Experimental Investigation of the Flow Dynamics in a Model of an Abdominal Aortic Aneurysm

Hani Abulkhair

A Thesis

in

the Department

of

Mechanical and Industrial Engineering

Presented in Partial Fulfillment of the Requirements

for the Degree of Doctor of Philosophy

at Concordia University

Montréal, Québec, Canada

June 2016

CONCORDIA UNIVERSITY
SCHOOL OF GRADUATE STUDIES

This is to certify that the thesis prepared

By: Hani Abulkhair

Entitled: Experimental Investigation of the Flow Dynamics in a Model of Abdominal
            Aortic Aneurysm

and submitted in partial fulfillment of the requirements for the degree of

          Doctor of Philosophy   (Mechanical Engineering)

complies with the regulations of the University and meets the accepted standards with
respect to originality and quality.

Signed by the final examining committee:

_____ Chair
Dr. J. Bentahar

_____ External Examiner
Dr. Y. Maciel

_____ External to Program
Dr. N. Bouguila

_____ Examiner
Dr. A. Dolatabadi

_____ Examiner
Dr. J. Dargahi

_____ Thesis Supervisor
Dr. L. Kadem

Approved by: _____
                   Dr. A. Dolatabadi , Graduate Program Director

                   _____
June 15, 2016   Dr. A. Asif, Dean
                   Faculty of Engineering and Computer Science

ii

Experimental Investigation of the Flow Dynamics in a Model of an Abdominal Aortic Aneurysm

Hani Abulkhair, Ph.D.

Concordia University, 2016

ABSTRACT

An Abdominal Aortic Aneurysm (AAA) is a vascular disease affecting seniors. It is described by an inflation of the aorta in the abdominal regions. The specific reason for this disease is not clear. Rupture of AAAs leads to death and current surgical interventions are risky and require frequent follow-up AAAs are usually associated with an Intraluminal Thrombus, which prevents blood from conveying oxygen and nutrition to the AAA walls. Formation of thrombosis are strongly affected by hemodynamics, and especially blood stasis.

It has been founded that blood stasis can be triggered by a reduction of flow rate such as that during sleeping or in people who suffer from lower limb amputation.

This change has been evaluated experimentally by time-resolved Particle Image Velocimetry. A compliant AAA model that has an aortic arch, renal arterirs, and an iliac bifurcation was designed and tested under normal and low flow conditions in terms of velocity behavior, residence time of particles inside the AAA, and shear history of particles during their movement.

Proper orthogonal decomposition and Dynamic mode decomposition have been applied to the flow in both planes to reveal the hidden dynamics and the coherent structures of the flow behavior inside the AAA.

The flow inside an AAA is mainly described by the jet penetrating the AAA with a large recirculation zone in the lumen. The velocity snapshots do not show a major difference between the two cases. Hidden dynamical structures were revealed by proper orthogonal decomposition and dynamic mode decomposition. Most of the small-scale dynamics occur near the entrance of the AAA. Vortical structures have been found to play a beneficial role in preventing thrombus formation. This study recommends focusing on the low flow conditions and developing a method that can promote blood flow mixing in patients with an AAA. The current study is the first study to evaluate the time-resolved behavior of the fluid flow inside AAAs and to decompose it into dynamical modes.

"In the middle of difficulty lies opportunity".
Albert Einstein

To my beloved parents
Abdulelah and Farida
and my beloved wife
Ghayda
and beloved sons
Abdulelah, Omar, and Hamza

ACKNOWLEDGEMENTS

TABLE OF CONTENTS

ABBREVIATIONS

AAA	Abdominal Aortic Aneurysm
CAP	Cell Activation Parameter
DMD	Dynamic Mode Decomposition
FSI	Fluid Structure Interaction
ILT	Intra Luminal Thrombus
LC	Low flow Condition
NC	Normal Condition
PRT	Particle Residence Time
PIV	Particle Image Velocimetry
POD	Proper Orthogonal Decomposition
SVD	Singular Value Decomposition
Re	Reynolds number
Sh	Shapiro number
St	Stokes number
Wo	Womersley number

LIST OF FIGURES

LIST OF TABLES

NOMENCLATURE

A_k, A_r constants for Richardson extrapolation
a temporal coefficient
A cross sectional area, m^2, snapshot matrix
$A_{\Delta t}$ linear mapping coefficient
c wave speed, m/s
d hydraulic diameter (diameter of the tube), m
d_p seeding particles diameter, μm
dt time between the two laser pulses, s
D_1, D_2 snapshots matrices
l_r length of the calibration target, mm
L_r length of the calibration target, pixels
l_t distance between the laser sheet and the camera, mm
p pressure, $mmHg$
t time, s
S companion matrix
u, v velcocites in the x and y directions, m/s
U, V orthogonal matrices
x spatial interrogation region dimension, mm
X previous position of a particle
X_n new position of a particle
y spatial interrogation region dimension, mm

GREEK
α conversation factor
ρ fluid density, kg/m^3
ρ_p seeding particle density, kg/m^3
μ fluid viscosity, $Pa.s$
τ viscous shear stress, Pa
τ_p characteristic time of particle, s
Δt integration time step, s
τ_s relaxation time of a particle, s
δ distensibility
ω frequency of the cardiac cycle, $1/s$
Σ diagonal matrix
Φ DMD coefficient matrix
ϕ POD coefficients (modes)
Λ Eigenvectors
λ Eigenvalues

1. INTRODUCTION

1.1 The Aorta

The aorta is the main and largest artery in the human body. Its diameter ranges from 15 mm to 25 mm. It is divided into four sections: the ascending aorta, the aortic arch, the descending aorta, and the abdominal aorta (Figure 1.1). The main role of the aorta is to distribute oxygenated blood and nutrients to the entire body through systemic branches. The aortic wall is mainly composed of two components: elastin and collagen (Länne et al. 1992, Abe et al. 2011). The major function of the elastin is to allow the aorta to stretch and recoil while the collagen helps in maintaining the structural shape of the vascular bed and provides it with tensile strength (Sakalihasan, Limet and Defawe 2005, Carmo et al. 2002). The aorta also includes several branches that supply blood to internal organs, making it a key organ in the arterial system. With aging, the aorta remodels itself to maintain its structural integrity and to withstand the stress on the walls. However, the process of stabilization and remolding can also alter the aorta in a way that weakens the aortic wall and enlarges its diameter.

1.2 Abdominal Aortic Aneurysms

Aneurysms can occur in numerous major arteries. The most common ones occur in the aorta and more specifically in the abdominal region; this type of aneurysm is called an Abdominal Aortic Aneurysm (AAA). An AAA is a vascular disease resulting from a dilation of the abdominal aorta. It is considered a health threat due its susceptibility to rupture. According to Zankl et al, 2007,

rupture of the abdominal aorta is the tenth largest killer among seniors in western countries and is the third leading cause of sudden death of men over 65 (Cowan et al. 2006). Globally, 500,000 patients are affected by AAAs each year (Bosch et al. 2001). A large screening study in Norway conducted between 1994 and 1995 showed that AAAs are present in 8.9% of males and 2.2% of females over 60 years old (Singh et al. 2001).
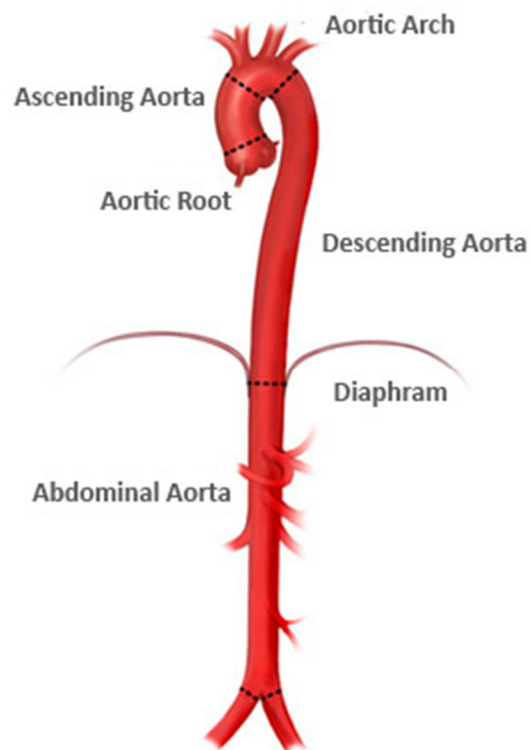
Figure 1.1: Schematic diagram of the aorta
(Ref: http://www.mountsinai.org/patient-care/service-areas/heart/procedures-and-services/aortic-aneurysm-repair/about-aortic-aneurysms)

Besides the risks of rupture, the lumen inside an AAA promotes thrombus formation. Thrombi can break down and block the iliac arteries and other distal arteries. Abdominal aneurysms are classified based on their shape. They can be either fusiform or saccular as shown in Figure 1.2 (Lasheras 2007). The most common aneurysms are of fusiform shape. They are formed between

the renal and iliac arteries whereas saccular aneurysms are a bulge located on one side of the abdominal aorta.
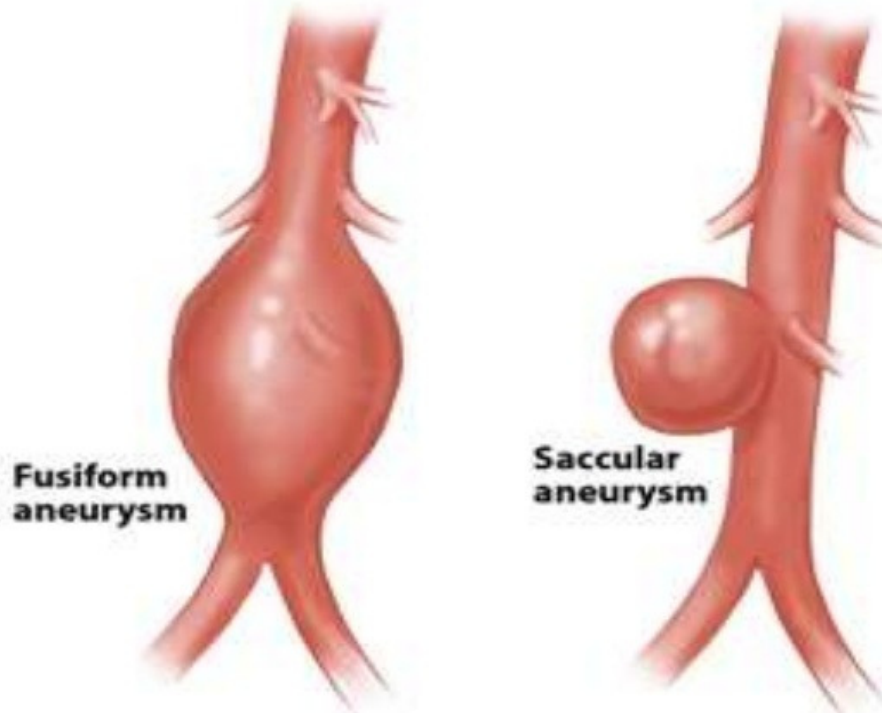
Figure 1.2: Types of abdominal aortic aneurysms
(Ref: http://www.slideshare.net/hawre14/aneurysms-dissection-7)

1.3 Symptoms

Patients with AAAs usually feel pain in their abdomen and back accompanied by a pulsating sensation in the abdomen. In some cases, AAAs are detected by physical examination. However, this method has been proven inaccurate and difficult for overweight and obese individuals (Lederle and Simel 1999). AAA diagnosis is usually performed by ultrasound imaging since it is the most accurate and least expensive method (Baxter, Terrin and Dalman 2008). According to Group Health (USA 2016), people who are between the age of 55 and 65 are recommended for Cone

Beam Computed Tomography (CT scan) screening based on their gender, family history, and smoking history. Once the AAA is detected, the patients will require an annual screening until the aneurysm reaches a critical diameter. They will then be advised for surgical intervention.

1.4 Treatment Options for AAAs

The only available treatment to date for AAAs is surgical intervention. Clinical investigation shows that 75% of patients are suitable for surgery (Chambers et al. 2009). The surgical intervention decision relies on the size of the AAA and the growth rate per year. Surgery is required when the AAA's maximal size exceeds 5.5 cm or when the growth rate is more than 1 cm per year. However, some studies questioned the validity of such parameters and showed that AAAs can rupture with a maximal size less than 5 cm, while some large AAAs remain stable (Raghavan and Vorp 2000). The risk of rupture varies between men and women. AAAs in women are more prone to rupture at smaller sizes, although their occurrence is 10 times less probable than in men (Isselbacher 2005).

There are two surgical treatments available for AAAs. Open Surgical Repair (OSR) and Endo-Vascular Aortic Repair (EVAR), (Figure 1.3). OSR is recommended for younger patients, but is risky and thus not suitable for all patients (Patel 2011). Although EVAR is appropriate for a lower percentage of patients than OSR, it has a lower mortality risk. Besides the higher cost of EVAR, patients undergoing the procedure are required to have frequent follow-up in hospitals (Ķīsis et al. 2012). In both groups, OSR and EVAR, patients stated some degradation in their quality of life especially in terms of mental health (Pettersson, Bergbom and Mattsson 2012). During the patient's life, the risk of aortic rupture is 25%. Therefore, the surgeons have to decide how early they should intervene in order to prevent this risk (Zarins et al. 2006).

EVAR is less invasive. However, (Greenhalgh et al. 2005) found that there is no significant difference between patients who undergo EVAR and patients who do not in terms of mortality risk. In addition, the high cost of surveillance and intervention for each patient added more complications to each patient's quality of life. Patients treated with EVAR experience significantly higher rates of graft-related complications and re-interventions. Brown et al. (2007) confirmed these results by pointing out that the graft-related complications and re-interventions are more common in the first four years after the intervention. As a result, patients treated with EVAR face significant comorbidities to the AAA.
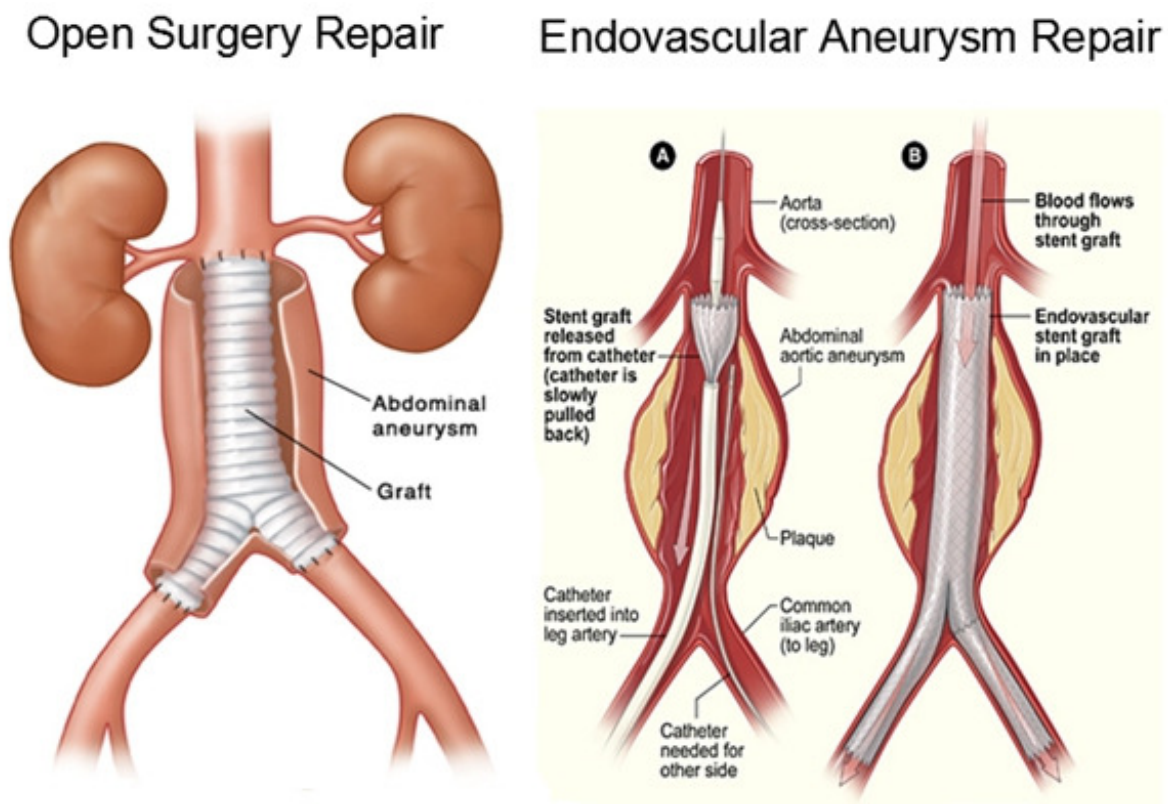
Figure 1.3 Surgical treatment methods available for AAAs
(Ref: http://reference.medscape.com/features/slideshow/abdominal-aortic-aneurysm)

1.5 AAA Initiation

The specific causes of AAAs are still unclear. However, many biological and mechanical hypotheses have been proposed to explain the development and progression of AAAs (Lasheras 2007). Studies have already demonstrated the link between AAAs and several vascular diseases like a stenotic bicuspid aortic valve (Pachulski, Weinberg and Chan 1991) as well as their associated global risk factors including high blood pressure, obesity, diabetes, smoking and some other biochemical mechanisms. Yet, the fact that most vascular diseases occur at specific locations in the arterial system favor the hypothesis of a significant contribution of local effects in the development and progression of vascular diseases such as AAAs. Previously, it was believed that AAAs were caused by infections on the arterial wall (Lasheras 2007) or as a result of atherosclerosis (Reed et al. 1992). The current dominant hypothesis for explaining the development of AAAs is that the cause is related to alterations in the aorta's properties (Lasheras 2007). Age plays a significant role in changing the arterial structure; with time, the aorta becomes stiffer and thicker. The stiffness accelerates the velocity and makes the pressure wave reflection stronger which may cause fatigue in the location of wave reflection namely at the iliac bifurcation (Nichols, O'Rourke and Vlachopoulos 2011).

AAA formation is linked to the degradation of the elasticity of the aorta (Sakalihasan et al. 2005). However, Lasheras (2007) questioned whether AAAs form as a result of wall degradation or hemodynamic changes in the abdominal aorta which cause unstable alterations of the anterior wall in contact with red blood cells. The alteration of elastin and collagen has been claimed to be an important factor in AAA formation and growth. The alteration is dependent on the production of proteases by vascular wall cells which is initiated by the inflammatory cells in the aortic wall

(Sakalihasan et al. 2005).

Seventy-five percent of the aneurysms are accompanied by an Intraluminal Thrombus (ILT) (Sakalihasan et al. 2005, Vorp et al. 2001). An ILT is a three-dimensional composition of fibrin structures comprised of platelets, blood proteins and red blood cells (Wu et al. 2007). The stasis of the blood cells and the recirculation zones promote platelet activation and result in the formation of an ILT (Bluestein et al. 1996, Malek, Alper and Izumo 1999).

The ILT is found to be strongly correlated with a weakening of the aortic wall where the thrombus works as a barrier between the aortic wall and the red blood cells that carry oxygen (Vorp et al. 2001). Figure 1.4 shows that the presence of an ILT has a strong correlation with reduced oxygen delivery to the aortic wall and a reduced thickness of the wall as well. ILTs can also break down and block the iliac arteries or other small arteries, which can lead to a life-threatening event. The presence of thrombosis may also reduce the lumen area and consequently reduce the pressure load on AAAs (which might help in reducing the probability of rupture). According to Faggioli et al. 1004, the presence of a thrombus in AAAs is a 'defense mechanism' against the stress on the aortic walls to prevent rupture. It is possible for the ILT to detach from the AAA wall; in this situation, the AAA will bear higher stress with weakened walls (Thubrikar et al. 2003). Satta, Läärä and Juvonen (1996), and Speelman et al. (2010) demonstrated that the overall thickness is associated with the level of risk of rupture. Furthermore, a clinical study by Schurink et al. (2000) found that the presence of an ILT changes the structural integrity and stability of the AAA wall. It is presently well accepted the progression of ILT and AAAs are closely linked to alterations in the flow field in the abdominal aorta (Chen et al. 2014). However, there is a significant gap regarding

the role played by flow conditions, and flow sub-structures, in the formation of ILTs.

(a) Effect of ILT Thickness on AAA wall pO_2

(b) pO_2 Gradient Through AAA wall with ILT (Group I)
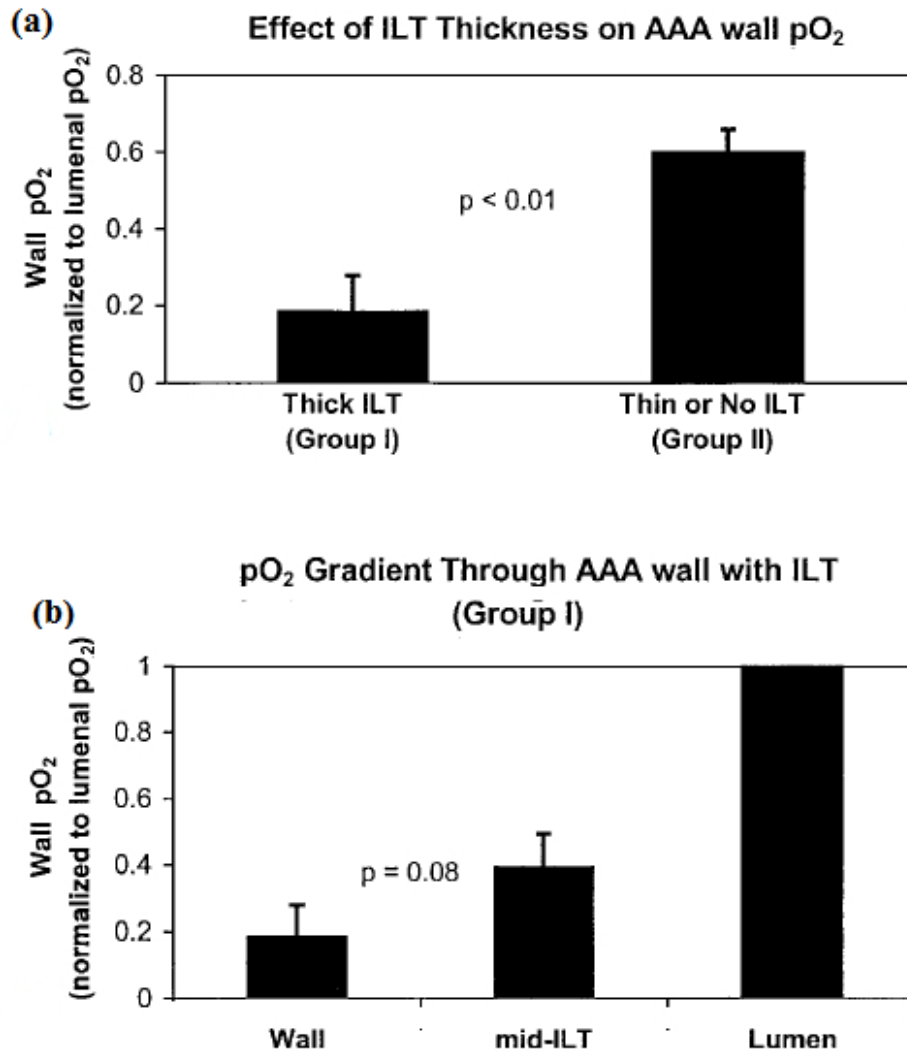
Figure 1.4: (a) Comparison of *in vivo* pO2 measurements for AAAs wall adjacent to a thick ILT versus AAAs wall adjacent to thin ILT. (b) In vivo measurements demonstrate pO2 gradient through the thickness of an AAA containing thick ILT (Vorp et al. 2001)

1.6 Thesis Organization

Chapter 1 is a general introduction to AAAs and the mechanisms believed to be involved in their initiation. Chapter 2 reviews the most significant role of hemodynamics in the progression and the

rupture of AAAs. Chapter 3 is a description of the state-of-the-art experimental facility developed for this study. Chapter 4 presents the flow characteristics and topology in AAAs under normal conditions (NC) and low flow conditions (LC). Chapter 5 provides more advanced characterization of the flow structures in AAAs under NC and LC using proper Orthogonal Decomposition (POD) and Dynamic Mode Decomposition (DMD). Chapter 6 includes a conclusion and suggested future research.

2. LITERATURE REVIEW

2.1 Introduction

The behavior of blood flow in arteries has been found to play a critical role in cardiovascular systems in terms of wall shear stress, diffusion between cells, normal pressure acting on the vessel walls and many other mechanical factors (Nichols et al. 2011, Caro 2012). Since the cardiovascular system contains many branches, curvatures, and narrow openings, blood is expected to face obstacles preventing it from being constantly laminar. Temporal changes in the stream of blood are a crucial subject in cardiovascular fluid flow. For instance, the transition to turbulence in blood vessels exerts a high frequency of fluctuation and inhomogeneous shear stress as well as random velocity. The main advantage of turbulence is its enhancement of mixing and transporting materials between cells. However, red blood cell surface membranes are vulnerable to rupture under excessive shear of the surrounding medium (Dooley and Quinlan 2009, Lokhandwalla and Sturtevant 2001). Besides the effects of blood particles, blood vessel growth and diameter are regulated by the flow rate and pressure inside the blood vessels. Blood vessels also remodel themselves to maintain small ranges of shear stress. In an adult artery, the shear stress is usually between 1-2 Pa (Giddens, Zarins and Glagov 1993).

2.2 Hemodynamics in a Healthy Aorta

When blood enters the aortic arch, it has a tendency to skew due to curvature. Seed and Wood (1971) studied the velocity profile in the aorta at various sections and demonstrated that the entrance of the descending aorta has an asymmetrical velocity profile. Moreover, Kilner et al.

(1993) showed that the curvature of the aorta causes a skewed velocity profile inside the abdominal aorta, which results in higher velocities at the inner side of the aorta. The degree of this skewness is influenced by viscous effects and the compliance of the aorta. However, its effect is still present in the renal arteries (Frazin et al. 1996). Atherosclerotic lesions occurring in arteries are motivated by the curvature of the aorta and the skewness of the velocity profile (Berger and Jou 2000).

Flows in the arterial branches undergoing transition to turbulence were first observed by Nererm et al. (1972). Renal arteries have a significant effect on the flow behavior in the abdominal aorta. Moore et al. (1992) stated that the branching of these arteries creates strong vortices just downstream of the arteries and complex transient separation. They also showed that during the deceleration in systole, a vortex is formed near the aortic wall and curls toward the center of the aorta. In addition, they demonstrated the presence of a transient flow reversal also located at the intersection between the renal arteries and the aorta. However, flow also moves inward and outward in the renal arteries. This complex flow behavior may have a strong impact on the flow patterns inside the abdominal aorta. Moore and Ku (1994) found that while resting, flow in the abdominal region becomes more complex during the deceleration phase where two vortices form after the renal arteries and a helical flow is found at the iliac bifurcation entrance.

For the iliac bifurcation, part of the pressure wave will be reflected at the branches, and some of the reflected wave goes back to the iliac arteries (see Figure 2.1). The reflection at this bifurcation alters stiffer aortas and can affect the systolic part of the pressure waveform. This alteration comes from the fact that the total pressure at the junction is equal to the sum of the incident wave and the reflected wave (Caro 2012, London and Guerin 1999).
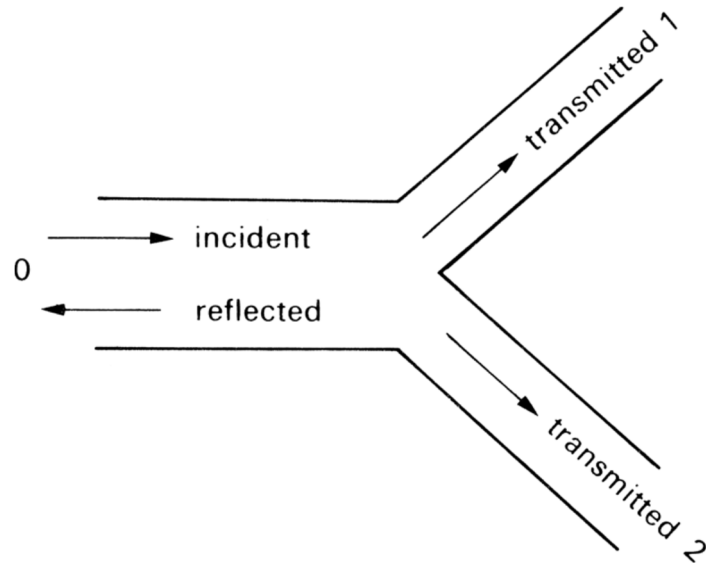
Figure 2.1: Sketch of an arterial bifurcation. The incident wave is partially reflected in the parent tube 0 and partially transmitted in the daughter tubes 1 and 2 (Caro 2012)

The viscosity of blood has two major effects on the aorta. First, when the viscosity works as a resistance to flow, it deforms the velocity profile by decreasing its gradient towards the center of the tube and increasing it in the boundary layer on the walls of the arteries. This gradient increases the shear at the walls and causes energy dissipation. Second, the viscosity affects the pressure wave where it works to attenuate the strength and speed of the wave. The strength of the wave speed is attenuated by the energy dissipation. Viscous forces work as an obstacle towards the oscillatory pressure gradient. Therefore, the viscosity weakens the spatial and temporal forces acting on the blood (Nichols et al. 2011). The spatial characteristics of the effects of viscosity are defined based on the Reynolds number (Re) which is the ratio between the inertial and viscous forces. This number is given by the following equation:

$$Re = \frac{\rho v d}{\mu} \tag{2.1}$$

where v is the velocity of the fluid at the tube (for the AAA in this study, this number Is defined at the inlet of the tube), ρ is the density of the fluid, μ is the dynamic viscosity of the fluid, and d is the diameter of the tube. The temporal characteristics are determined by the Womersley number, given by the following equation:

$$Wo = d \left(\frac{\omega\rho}{\mu}\right)^{1/2} \tag{2.2}$$

where ω is the frequency of the pulsatile flow.

2.3 Hemodynamics in Abdominal Aortic Aneurysms

As stated in chapter 1, hemodynamics plays an important role in the progression of AAAs. Nichols et al. (2011) summarize the mechanical factors that might lead to aortic dilatation. The presence of turbulence is attributed to weakening of the aortic wall. Khanafer et al. (2007) found that turbulence is one of the main reasons for high blood pressure and shear stress on the vessel walls. While pressure stays almost the same inside the AAA region, the kinetic energy generated by the turbulence destabilizes the Wall Shear Stress (WSS) and impacts the distal part of the AAA.

One of the theories assumes that the aorta is similar to a pipe under oscillatory pressure, where failure of this pipe is usually caused by fatigue (Lasheras 2007). It is very complex to consider such a theory in human arteries due to the complexity of the flow behavior and the arterial wall structure. Lasheras (2007) stated that a complex interaction between several biological factors and changes in the hemodynamic stimuli on the vessel wall might destabilize the properties of the arterial wall. He argues that rupture occurs when the inflated artery fails to support the stress

resulting from blood flow. Moreover, Sforza, Putman and Cebral (2009) emphasize the fact that hemodynamic factors play an important role in the growth of the AAA's size due to the cyclic loading applied on the aorta.

Endothelial cells in direct contact with blood particles are exposed to variations in WSS as they are affected by disturbed blood flow patterns (Chiu and Chien 2011, Jilkova et al. 2014). These cells are prone to damage under excessive shear stress (Fry 1968, Chiu and Chien 2011). As one of the main functions of these cells is to control wall permeability, low permeability leads to atherosclerotic plaque deposits and to a formation of lesions on the aortic tissue (Aird 2007). On the other hand, low wall shear stress is strongly correlated with atherosclerotic intimal thickening (Ku 1997).

Atherosclerosis is usually associated with AAA formation. The most affected region by atherosclerosis is the infra-renal aorta due to the branching of the iliac and renal arteries. The inflammatory sites can generate certain enzymes which may participate in the degradation of elastin and collagen, and eventually initiate the aneurysm (Moore et al. 1992).

Once an AAA is formed, it will gradually enlarge. Surgical intervention will be based on the diameter or the growth rate. However, the diagnosis may not be accurate as small size AAAs can also rupture, and large aneurysms can keep inflating to reach even larger sizes without rupture (Darling 1970). The relation between hemodynamics and narrowing of the blood vessels is complex. Blood vessels try to adapt to long term changes from WSS by vasodilation and wall remolding.

2.3.1 Steady Flow

Budwig et al. (1993) tested the transition from laminar to turbulent flow in rigid symmetric AAA models by applying a steady flow. The flow is described as a jet surrounded by a pair of vortices. WSS decreases by a factor of 10 in aneurysm bulges when compared to the entrance region. Peattie and Ringer (1994) investigated the critical Reynolds number at the inlet of the tube for transition to turbulence and discovered it to be between 2000 and 2600. As the size of the AAA increases, a lower Reynolds number is needed to establish turbulence. By considering the maximum Reynolds number throughout the cardiac cycle and determining whether it leads to turbulence or not, surgical intervention can be recommended. The disturbance in the flow inside an AAA is considered to be an indication of the weakness of the walls since it alters the WSS.

The size of the AAA also has a strong impact on the position of the vortex ring. This vortex is formed at the distal part of the AAA, and its strength is proportional to the size of the AAA as well as the Reynolds number (Patel 2011, Schrade et al. 1992, Peattie and Ringer 1994, Yu 2000, Asbury et al. 1995).

Patel (2011) illustrated the effect of the iliac bifurcation angle on AAAs. Compared to a model without an iliac bifurcation, an increase in resistance to the flow was observed due a large momentum change from the aorta to the iliac bifurcation. Moreover, a high pressure was measured at the bifurcation junction, and its amplitude was a weak function of the bifurcation angle. Although this study was based on steady-state conditions, it proved the importance of considering the presence of the iliac bifurcation when studying the flow in AAAs.

All of these studies were based on a steady flow, which does not have a direct relation to the hemodynamics of the actual pulsatile flow, and does not illustrate the changes occurring throughout the evolution of the cardiac cycle. Moreover, this limitation ignores the transition of the vortex ring as well as the evolution of the shear layer.

2.3.2 Pulsatile Flow

The effect of pulsatility was widely investigated in the clinical literature. Lasheras (2007) reviewed some of the main studies discussing the effect of hemodynamic stimuli on AAAs. Yu et al. (1999) investigated the fluid flow in three different sizes of glass models of AAAs. By fixing the Reynolds number (Re) and the Womersley number (Wo), they found that after systole, the flow begins to separate and forms a vortex. This vortex migrates during diastole and disappears in the distal part of the AAA.

Egelhoff et al. (1999) showed that the level of exercise increases the probability of turbulence and vortex formation in the AAA. The average Re for the study was between 362 and 1053, while the average Wo was between 16.4 and 21.2. By testing two models of AAAs different in their sizes at low Re, small AAAs results in an attached flow for the whole cycle. As the size of the AAAs increases, the flow starts to separate from the proximal neck and forms a stagnant pair of vortices near the proximal neck. This pair migrates with the flow by increasing Re. This study shows that such vortices are the main reason for large spikes in the WSS and temporal evolution.

Fluid structure interaction (FSI) simulations have been widely used to simulate compliant models.

16

Salsac et al. (2006) studied the variations in WSS during the progressive enlargement of AAA size. The aim of the study was to define the causes of the flow separation as well as the initiation of the vortex ring in simplified models of AAAs. Their research indicates that the flow starts to separate when the dilatation ratio is equal to 1.3 (the ratio between the size of the aneurysm to the aortic diameter D/d, see Figure 2.2). This flow separation causes a strong vortex ring and an internal shear layer. Moreover, the vortex ring becomes stronger as the dilatation ratio is increased. The critical regions found in their model were the separation at the proximal neck and the reattachment region in the distal part.
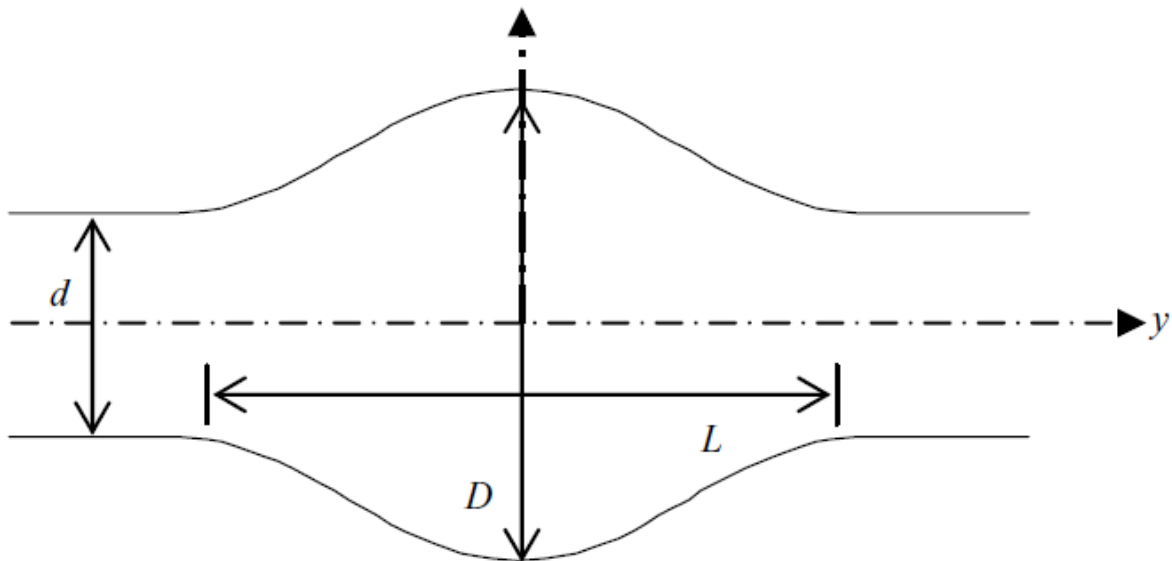
Figure 2.2

Figure 2.2: Geometry of AAA used by (Salsac et al. 2006)

Deplano et al. (2007) conducted an experimental study to investigate the flow patterns inside both rigid and compliant AAAs. Their work demonstrates that as the model becomes rigid, the generated vortices tend to collide, which contributes to an increase in the WSS. Although previous studies showed that the abdominal aorta becomes less distensible with age (Wilson et al. 1998), rigid models do not reflect the real WSS distribution due to the fact that the elasticity of the

aneurysm increases gradually with time.

Khanafer and Berguer (2009) assumed there was a turbulent flow inside the aneurysm and compared the rigid and compliant FSI models. The rigid model overestimated the WSS values. Furthermore, the maximum WSS occurred at the peak of systole, whereas the highest WSS in the compliant model occurred just after the peak of systole. In terms of flow behavior, the energy stored in the compliant model delays and weakens the formation of vortex structures in the proximal part of the aneurysm. In general, the viscoelastic dissipation of the aortic wall has been shown to be more important than viscous dissipation (Caro 2012).

Stamatopoulos et al. (2011) performed PIV measurements on a specific patient model. The PIV tests were conducted on 14 planes and then interpolated to reconstruct a 3D visualization of the flow field. Flow disturbance (fluctuations of velocities from cycle to cycle) was found in the posterior wall particularly in the deceleration. High shear stress appeared at these locations.

(Suh et al. 2011) showed that frequent exercise activity might help reduce the progression of AAAs. Their study hypothesizes that increasing the level of activity during the day will influence hemodynamics by reducing the progression of the aneurysm: quickly washing blood particles away from the aneurysm in such a way that the probability of thrombus formation is reduced.

Following the original work of Deplano et al. (2007), Deplano et al. (2013) added an iliac bifurcation to the model. They performed 3D visualization of the flow behavior to evaluate the development of the vortex ring generated inside the AAA. Their work demonstrates that the iliac

bifurcation contributes to an increase of about 90% in the impingement of the vortex ring when compared to a model without an iliac bifurcation. This impingement process contributes to an increase of the force applied on the wall of the AAA.

Most previous studies illustrate the effect of normal flow on AAA progression and some aspects related to ILT formation. Some tested the effect of elevated flow and pressure in terms of exercise conditions. The results indicate that exercise is advantageous for reducing AAA formation (Suh et al. 2011, Dalman et al. 2006, Arzani and Shadden 2012). However, other studies suggest that the effect of exercise leads to the progression of AAAs (Egelhoff et al. 1999, Deplano et al. 2007).

Humans often experience circumstances where their blood flow is reduced, for example if one is sleeping or suffering from certain health conditions such as lower limb amputation or spinal cord injury. There are numerous problems associated with sleeping on cardiovascular systems. The mortality risk is higher in people who experience long term sleeping (Grandner et al. 2010). Excessive sleeping is also linked to cardiometabolic risk (Knutson 2010), coronary artery calcification (King et al. 2008), and other cardiovascular issues. In addition, Abe et al. (2011) stated that long term low flow is associated with carotid artery atherosclerosis. During sleep, blood pressure and blood flow rates are reduced, consequentially slowing down the blood's movement and sometimes leading to blood stasis, a leading cause of thrombosis. Vollmar et al. (1989) argue that people suffering from a lower limb amputation are more likely to develop AAAs at earlier ages. Their study showed that patients suffering from lower limb amputation have a percentage of retrograde flow in the abdominal aorta toward the renal arteries, which in turn initiates inflammation within the endothelial cells.

2.4 The Role of Fatty Materials in Thrombosis Production

The alteration of elastin and collagen in the aortic wall lead to a reduction in the wall's strength and changes in its structures. The accumulation of fatty material on the aortic wall leads to plaque formation. These symptoms are commonly found in patients with aneurysms. Some studies indicate that plaque in infected arteries is a consequence of low blood flow velocities and a transition from laminar unidirectional regimes to more chaotic regimes (Glagov et al. 1988). As a consequence, plaque starts to accumulate in the affected region.

The low shear regions formed behind plaque regions increases the activated platelets which aggregates and forms a thrombus. Thrombosis can also form in a region of injury. Within diseased arteries like those affected by an AAA, the thrombus fibrin attracts blood particles. The thrombus enlarges during blood stasis as the aggregation process is elevated (Li and Kleinstreuer 2006). The presence of a thrombus in AAAs was once thought to be a defense against stress on the aortic walls to prevent rupture (Faggioli et al. 1994). However, Satta et al. (1996) compared patients with ruptured AAAs to patients with large unruptured AAAs and found that ILT thickness and volume in ruptured AAAs are much higher than in the unruptured ones. Furthermore, the clinical study by Schurink et al. (2000) demonstrated that the presence of an ILT changes the structural integrity and stability of the AAA wall.

Rayz et al. (2010) performed a numerical investigation of blood stasis in a patient-specific model of an AAA. By comparing the locations of ILTs and the location of blood stasis, the researchers found that ILTs and blood stasis occur in almost the same regions. These regions also suffer from

low WSS. One of the recent *in vitro* studies by Chen et al. (2014) compares AAAs with and without ILTs. Their study shows that the presence of an ILT hinders vortex formation. They suggested that control of the vortex formation in the AAA lumen most likely reduces the risk of rupture.

2.5 Stability of the Flow and Coherent Structures

The instability of blood flow has been described in almost all previous studies that applied the pulsatility effect on AAA testing, as being a transition from laminar flow to turbulent flow (Egelhoff et al. 1999, Salsac et al. 2006, Stamatopoulos et al. 2011).

One of the earliest studies on the stability inside circular pipes was performed by Yellin (1966) The instability criteria were defined based on the flow rate variations. Using an oscillating flow, they were capable of overcoming instabilities generated at the entrance of the pipe. The critical moments were found to be the instants of inflection in the velocity profile where the flow experienced high degrees of adverse pressure gradient and separation from the tube walls.

The stability of a pulsatile flow in a circular tube has been also performed by Das and Arakeri (1998). The flow was mainly laminar under a Reynolds number of 500. The flow became unstable in the sub-wall region where an array of periodic vortices formed during the deceleration period. These kinds of instabilities were destroyed upon the acceleration of blood flow.

An experiment involving the stability of flow inside AAAs was performed *in vitro* by Yip and Yu (2001). They classified general flow behavior into three regimes: A, B and C. Regime A did not have any vortex formation while regimes B and C did. In regime B, vortices were stationary at the

separation region (proximal neck) or moved slightly to the core of the AAA, while in regime C vortices migrated to the distal part of the AAA. Based on the stability analysis, they found that the transition to turbulence and the formation of small vortical structures occurred during the deceleration region for regimes B and C.

Linear stability analysis has also been applied on numerical simulations in rigid models of AAAs. Gopalakrishnan, Pier and Biesheuvel (2014) examined numerous AAA sizes with varying aspect ratios and Womersley numbers, they found that under resting conditions, small aneurysms are prone to have unstable flow behavior in comparison to larger ones. When the AAA experienced higher flow rates (exercise conditions), the threshold of instability elevated, and consequentially led to high variations in WSS, activating platelets and forming a thrombus.

The importance of vortical structure behavior in AAAs was first suspected by Biasetti, Hussain and Gasser (2011) who demonstrated that vortical structures form in tortuous regions or when flow separates at the proximal neck. This tortuosity and flow separation create a local vortex that can activate platelets. Thus, they concluded that platelet tracking is important in assessing the triggering and aggregation of platelets. In fact, the presence of the vortical structures is what first activates the production of platelets, which forms thrombosis and lead to aortic wall degradation.

Hussain (1986) defined dominant coherent structures as fluid elements that capture the overall dynamics of the blood flow and carry the bulk of the mass and energy of a fluid. The importance of showing the presence of these structures comes from the fact that turbulence generation in blood vessels adds burdens on red blood cells and may lead to hemolysis (Raval et al. 2010). One of the

most common methods for analyzing the coherent structures in fluid flow is by using POD. It was first introduced by Lumley (1967). This method was modified and extended by Sirovich (1987) to use data snapshots.

POD is a method for decomposing an unsteady flow field into a number of modes. These modes hold the main energetic structures of the flow, which provides a compact and simple representation of it (Holmes 2012). This method has been applied in many fluid flow applications. Cosadia, Boree and Dumont (2007) used POD on time-resolved PIV to reveal the large and small scale structres in a deasial engine. Perrin et al. (2007) compared the phase-average turbulence with the coherent structures extracted from PIV of wakes behind a cylinder. Using POD, researchers can predict the vortex shedding and express the whole flow by a few modes. Meyer, Pedersen and Ozcan (2007) analyzed a jet in crossflow by testing several planes at the middle of the jet, and some other perpendicular planes. Using POD, they found that the wake vortices are less dominant than vortices generated in the shear layer. The use of POD to examine cardiovascular flows has been documented in two major studies. The first was conducted by Grinberg, Yakhot and Karniadakis (2009), who utilized POD on *in vivo* MRI images extracted from the occluded artery to quantify different flow regimes. However, the low temporal resolution of MRI prevented the capture of coherent structures correctly. Another study conducted by Kefayati and Poepping (2013) applied POD on normal and stenosed carotid arteries. They discovered that as the stenosis becomes severe, more modes are required to represent the flow field, and more complex flow structures appear. More information about the theory of this method is presented in chapter 5.

One of most recent methods for analyzing an unsteady fluid flow is called Dynamic Mode

Decomposition (DMD). This approach was introduced by Schmid (2010) and can decompose blood flow into modes based on frequency and find out whether the mode is growing or decaying with time. Many studies used this method in their applications. For instance, Schmid (2010) studied the wake behind a flexible membrane. This method was mainly applied to quantify the dynamics of jets (Rowley et al. 2009, Schmid 2010, Semeraro, Bellani and Lundell 2012). To the best of our knowledge, no studies have been conducted analyzing cardiovascular flow using the DMD method. POD and DMD have the potential to provide information about the stability of AAA structures, their growth/decay rate as well as their frequency. Coherent structures are formed in the shear layer or near the walls.

Previous research has documented how blood flow becomes more disturbed and turbulent. However, they neither mentioned the consequences of main structures within blood flow nor examined the frequencies of these structures. They also did not mention the general characteristics of flow behavior. Understanding these issues can lead to an enhancement in rupture diagnoses, thrombosis formation probabilities and a deep understating of the flow behavior inside AAAs. Moreover, POD and DMD can provide information about the stability of structures, their growth/decay rate, and their frequency.

2.6 Motivation

Previous studies highlighted the importance of hemodynamic effects in AAA progression and its contribution to intra-luminal thrombus formation by testing various flow conditions and AAA sizes as well as other factors. In these experiments, the flow conditions were limited to both normal and exercise flow conditions. While exercise has been shown to eventually be a good way to

prevent AAA progression, its effect is limited to small periods of time during the day, and most seniors are not capable of exercising intensely enough to make a difference. Moreover, humans experience circumstances where their blood flow is reduced, which other studies did not take into consideration.

As a conclusion from previous studies, once AAAs is formed, ILTs start to from as a result of blood stasis and platelet activation. The low flow conditions are associated with higher probability of blood stasis. This effect has to be investigated and quantified. The platelets accumulate shear while moving with the blood stream and they are involved in ILT formation. These two factors are discussed in chapter 4. Moreover, this study highlights the major difference inside AAAs between NC and LC hemodynamics. Moreover, it will analyze the flow behavior to give a general characteristic in terms of small and large coherent structures, and finally, it will analyze the frequency phenomena occurring during each cardiac cycle as will be discussed in chapter 5.

2.7 Objective

As outlined from the previous studies, there is some lack of knowledge in-terms of the role of low flow contribution to AAA progression, and the role of vortical structures in AAAs. Therefore, this study has two major goals:

- To investigate the flow dynamics in an AAA model under normal and low flow conditions in terms of thrombus formation and spatial and temporal flow structures.
- To generate new knowledge for developing new innovative mechanics and new medical devices to limit the progression of AAAs.

3. EXPERIMENTAL SETUP AND TEST CONDITIONS

3.1 Introduction

This chapter will present the details of the experimental apparatus and methodology used in this thesis, from building the AAA model and performing particle image velocimetry measurements to post-processing the resulting velocity fields.

3.2 Abdominal Aortic Aneurysm Model

The geometry of the aneurysm was selected based on the CT images available in Les et al. (2010) This study selected eight AAAs in their earlier stages. The idealized average model of these eight patient-specific geometries has been drawn using a CAD software. The shapes were then 3D printed. Figure 3.1 shows the dimensions of the selected model, while Figure 3.2 presents a sample of a 3D printed model. The models were attached to a rotating machine, and multiple layers of silicone were applied in order to create the elastic model of the AAA.
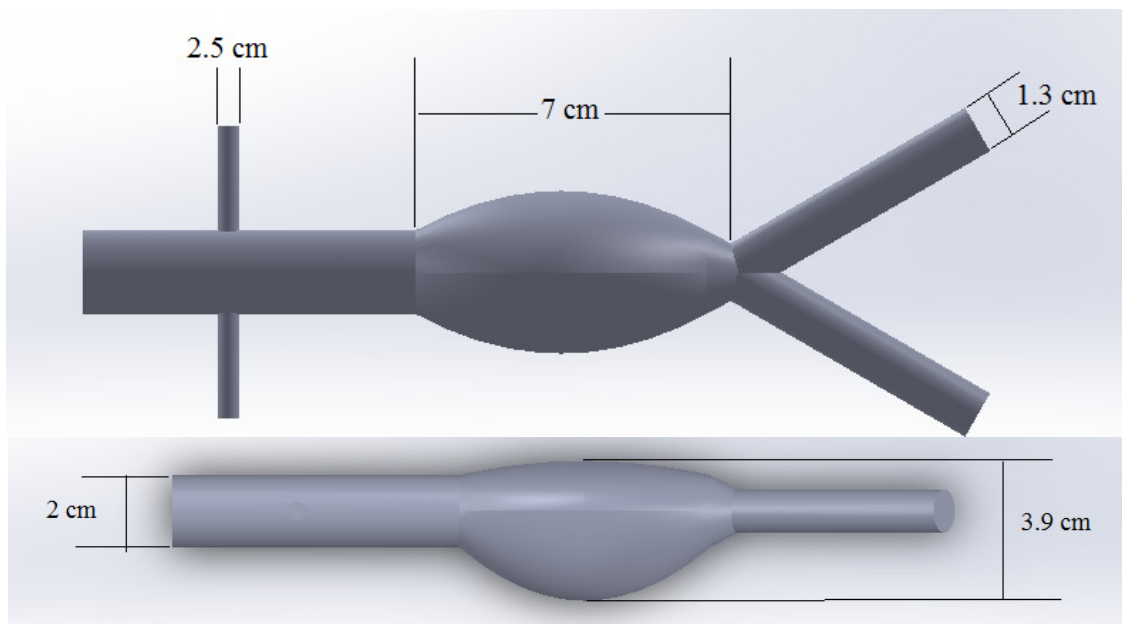
Figure 3.1: Dimensions of the AAA model used in the current study

26

The silicone used in this study was Polycraft Silastic T4, with a 10:1 ratio by weight of the base material and the curing agent. Since the base material is very viscous (70000 cP), the mixing process with the curing agent led to air bubbles being trapped in the mixture.

To remove the bubbles, the mixture was placed in a vacuum chamber for 30 minutes: enough time for the bubbles to be completely removed. The mixture was then painted on the printed model of the AAA using a standard paint brush. Overall, seven to eight layers were needed to coat the transparent model of the AAA. Polycraft Silastic T4 provides reasonable radial deformation values compared to *in vivo* data. It should also be mentioned that other materials can also be used to build models of AAAs. For example, Stamatopoulos et al. (2011) used Solar-Sylgared 184 to build an AAA model and Deplano et al. (2007) used polyurethane. In this work, we also attempted to use Solar-Sylgared 184. However, detaching the elastic model from the 3D printed mold was difficult without significantly damaging the AAA model. Finally, we also attempted to use other materials such as clear flex 50. However, the resulting AAA model was not elastic and transparent enough (for optical measurements). All materials had disadvantages in terms of elasticity and clarity. Figure 3.3 shows a sample of a transparent model, utilized in this study. The radial deformation of the model between the systolic and diastolic pressures is 3.8%, which is close to *in vitro* data found in Nichols et al. (2011) which is 4.3%. Reproducing the correct wall deformation is important since previous experimental or numerical studies have shown that the interaction between the fluid and the wall significantly determines the flow topology in models of AAAs (Deplano et al. 2013).
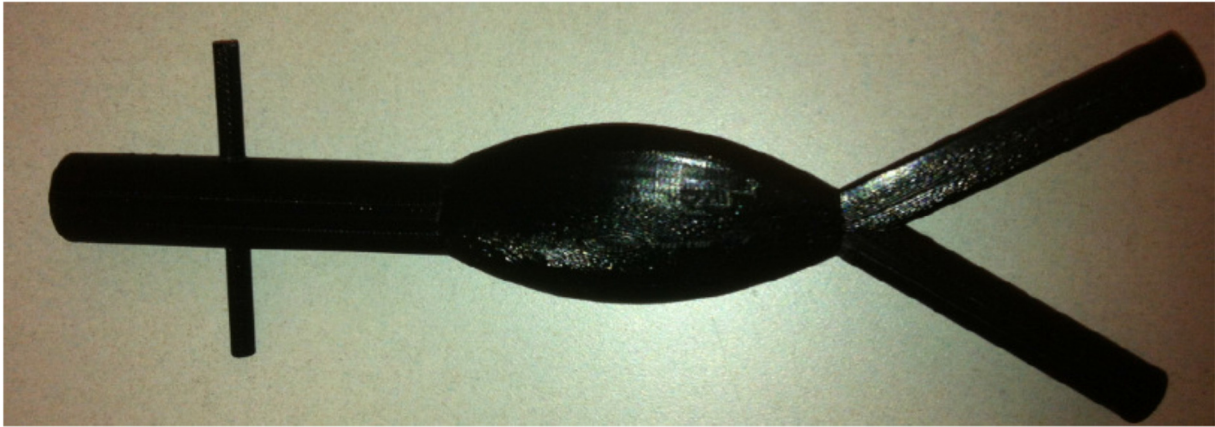
Figure 3.2: 3D printed model of model of AAA

Figure 3.3: Silicon transparent model of AAA

3.3 Blood Analog

Blood consists of a complex mixture of cells, proteins, lipoproteins and ions (Ku 1997) that display a non-Newtonian behavior. The main component affecting the viscosity of blood are red blood cells which make up about 40% of the total volume (this percentage is commonly called hematocrit). Red blood cells increase the viscosity of blood, making it around four times the viscosity of water. However, as the diameter of blood vessels increase (typically > 1 mm), the effect of red blood cells is less significant and blood shows a Newtonian behavior (Pedley and Luo

28

1995, Berger and Jou 2000). In this experimental study, the blood was simulated by mixing water and glycerol (60% water and 40% glycerol, by volume). The solution had a density of 1100 kg/m^3 and a viscosity of 3.7 cP, which is close to reported blood properties in large arteries (Waite and Fine 2007). This blood analog was used as a circulatory fluid and pumped from an open tank by a centrifugal pump, controlled by a custom made LabVIEW code, through the aortic valve, the ascending aorta and finally through the abdominal aorta with the AAA model.

3.4 Code for Controlling the Pump

A custom made LabVIEW^{TM} code was developed to control the pump signal required to have physiologically correct pressure and flow waveforms in the AAA model. In addition to the signal sent to the pump, a trigger (TTL signal) was added to the code to mark the starting point for pressure, flow, and PIV measurements. Figure 3.4 shows the sent to the pump. The first half of this signal consists of: sine wave which mainly aimed to send the pump the behavior of the cardiac cycle during the systolic period. The second half is a negative wave which aimed in generating some back flow to close the mechanical heart valve. Finally, a constant zero wave repressing the rest of the diastolic part. The combination of these three components of waves could result in a similar waveform found *in vivo* (Nichols et al. 2011) with some fluctuations in the diastolic part (see Figure 4.1). The presence of these fluctuations were found in some studies dealing with AAA like Swillens et al. (2008) and Deplano (2007).

3.5 Pressure and Flow Waveforms

To regulate pressure variations, a mechanical heart valve was placed at the entrance of the

ascending aorta. For the NC, the aortic peak systolic pressure was adjusted to be around 120 mmHg and the end diastolic pressure to be around 70 mmHg. A total of 1.6 L/min was pumped from the tank: 0.6 L/min through the renal arteries and 1.0 L/min through the AAA model and the iliac arteries. These conditions are similar to those of Moore et al. (1992). The AAA model is placed in a transparent Plexiglas box filled with the same blood analog circulatory fluid. As for the low flow conditions (LC) simulated in this work, Deqaute et al. (1991) showed that during sleeping, pressure, flow rate, and heart rate are reduced. They illustrated that the heart rate reduced from 72 bpm to around 60 bpm, pressure reduced to between 50 mmHg and 100 mmHg, and flow rate was reduced with around 20% of the original flow amount. Therefore, the experimental conditions were set as: peak systolic/end diastolic pressures of 100/50 mmHg and a total flow rate of 1.2 L/min. With 0.5 L/min through the renal arteries and 0.7 L/min through the AAA model and the iliac arteries. The heart rate was 72 bpm and 60 bpm for the NC and the LC, respectively.
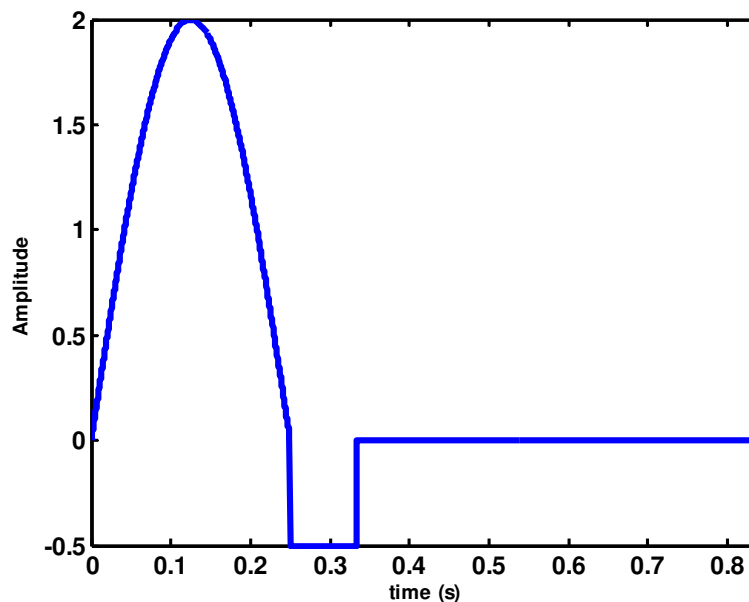
Figure 3.4: Schematic of the voltage waveform sent to the pump to generate the flow waveform

Instantaneous pressure measurements were performed using a Millar catheter MPR 500 (Millar Instruments, Houston, TX, USA, accuracy 0.5% full scale). Instantaneous flow measurements were performed using a Transonic flow meter T201 (Transonic Inc., Ithaca, NY, USA, accuracy 1% full scale). Both pressure and flow rate measurements were performed 10 cm above the proximal neck of the AAA model.

The average Reynolds numbers are 357 for NC and 297 for LC. The elastic wave propagation velocity in the system was estimated as 8.78 m/s. This value was estimated from the following equation:

$$c = 1/\sqrt{\rho\delta} \tag{3.1}$$

Where δ is the distensibility of the aorta $\delta = A^{-1}\frac{\delta A}{\delta p}$, A and p are cross-sectional area and pressure respectively. This velocity is comparable to wave speeds expected in the aorta which is around 10 m/s (Lighthill 1975). The ratio between the elastic wave propagation velocity and the flow velocity is called the Shapiro number (Sh) (ratio between the velocity of the fluid flow and the wave speed velocity). This is an important design parameter. In our model we obtained a value of around 0.035 based on the maximum velocity, which is consistent with the expected values in the aorta $Sh \approx 0.1$ (Duclaux, Gallaire and Clanet 2010). Figure 3.5 shows a schematic diagram of the complete system including the location of pressure and flow measurements.
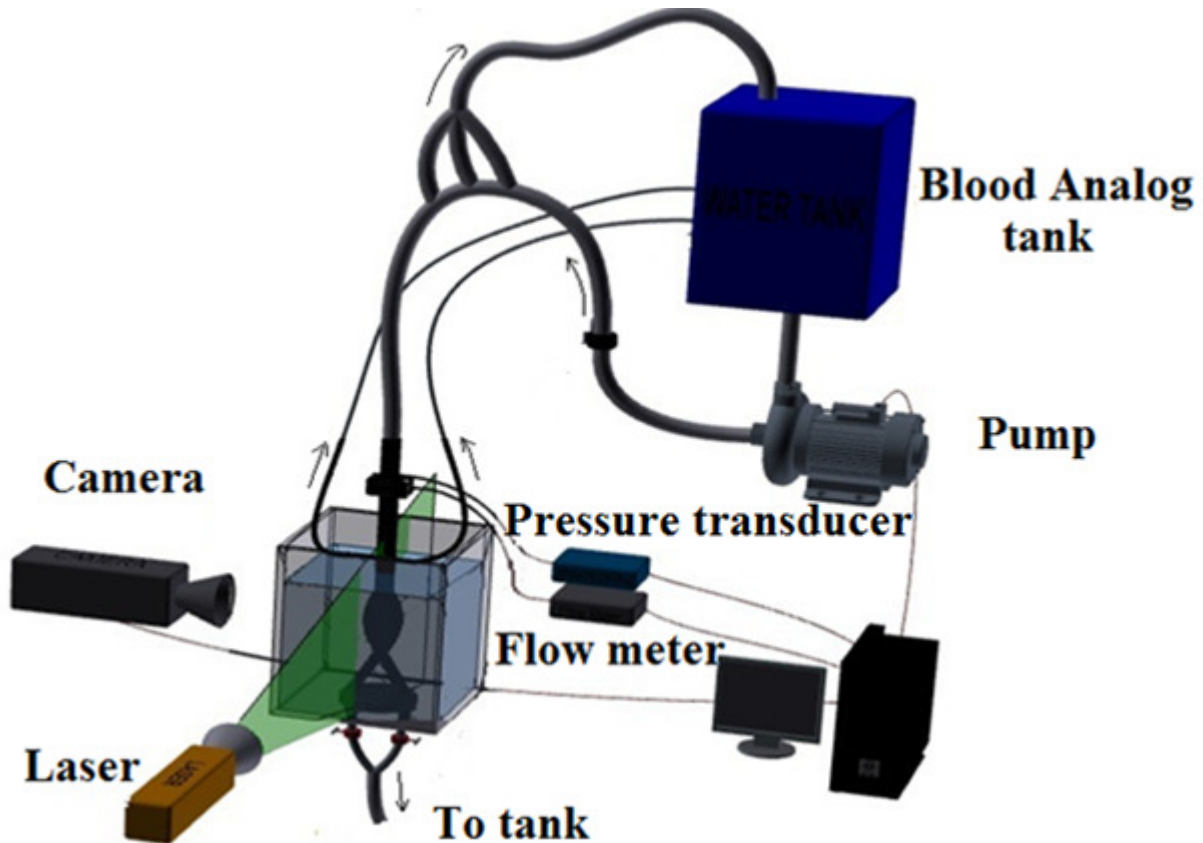
Figure 3.5: Schematic diagram of the experimental facility

3.6 Velocity Field Measurement using Particle Image Velocimetry

Particle image velocimetry (PIV) is an optical velocity measuring technique that uses a laser, CCD cameras, and seeding particles. The basic principle is that particles, a couple of micrometers wide, are seeded in the flow field. A laser sheet is directed to the test section to illuminate the particles. Two consecutive images of the illuminated particles are taken by a camera. By knowing the difference in time between the two images and the distance traveled by the particles between these two images, the velocity of the particles corresponding to the flow stream velocity can be calculated.

The images show numerous particles, not all of which have the same speed. Therefore, each image

is divided into small sections known as interrogation areas (measuring between 8-64 pixels). A cross-correlation is then applied to each interrogation area to identify the direction and speed of the seeded particles. To speed up the correlation process, Fast Fourier Transform was implemented. Figure 3.6 shows a schematic diagram of the arrangement of the laser sheet in a fluid stream (Raffel, Willert and Kompenhans 2013). Using particles to track the fluid motion is not new and has already been performed in the early 20th century by Prandtl (Raffel et al. 2013). Using interrogation regions and cross-correlation methods have been introduced by Adrian (1991). This method was later extended to include multi-frame exposure (Keane and Adrian 1992). PIV has already been used in several research areas, including turbomachinery (Hill, Sharp and Adrian 2000, Duquesne, Maciel and Deschênes 2015), aerodynamics (validation of numerical simulations) (Chen et al. 2014) and cardiovascular flows (Keshavarz-Motamed et al. 2014, Tanné et al. 2010).
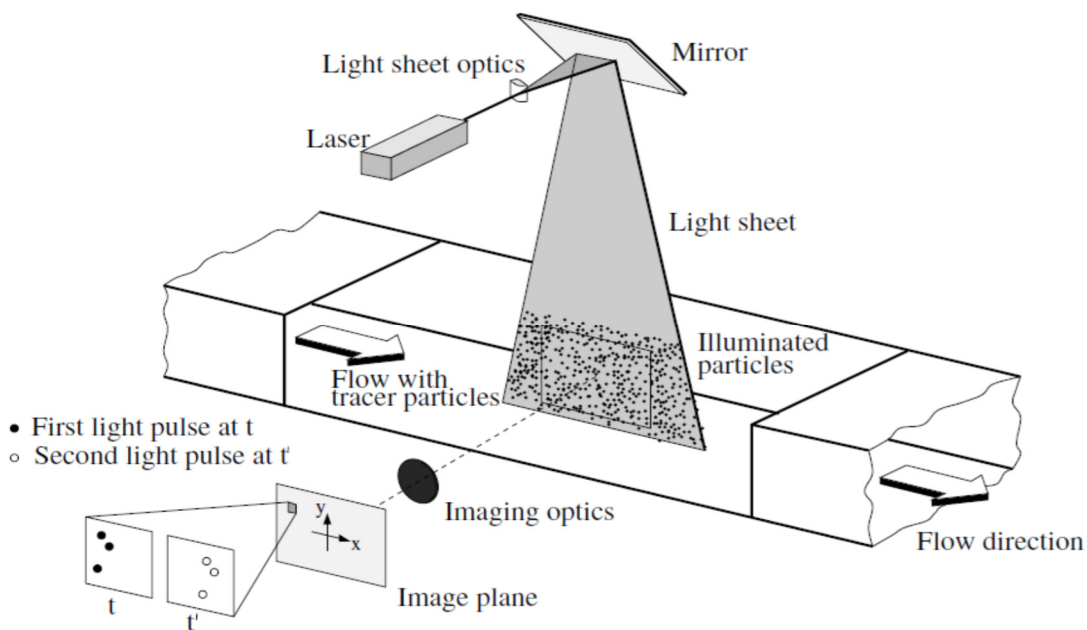
Figure 3.6 Schematic of the arrangement of the laser sheet in a flow stream (Raffel et al. 2013)

- Adaptive correlation and validation of velocity vectors

In most PIV applications, multiple sizes of interrogation regions are used to validate the resulting values of the vectors. A large interrogation area was first used to find a rough estimate of the values, where they can be used as an initial guess for the smaller interrogation regions. There are two iterations performed in these operations. Moreover, 50% overlap between the interrogations regions was implemented to recover the information near the edges.

Validation of the velocity vectors is an important step to remove the outliers (Keane and Adrian 1992). This step was performed by comparing the estimated velocity vector with the nearest vectors and apply a median filter to remove the outlier vectors. This step was implemented in the post-processing by removing vectors with 1/peak 2 = 1.1. Table 3.1 presents the main post-processing parameters.

Table 3.1: PIV parameter used for post-processing

Interrogation region	Multi-pass cross correlation - Initial size 64×64 pixels - Final size 16× 16 pixels 50% overlap Final spatial resolution is 0.787mm × 0.787mm
Peak locking	Subpixel interpolation
Velocity validation	Cross-correlation peak validation: - Minimum ratio peaks 1/ peak 2: 1.1 - Elimination of spurious vectors: Median filter Remove if difference to average > 2 rms of neighbors Neighborhood size: 3×3

- Calibration and refractive index estimation

The calibration target was a special reference frame which has an accuracy of 0.5 mm. This target was placed inside the AAA model at the position of the laser sheet. The laser sheet thickness for all measurements was around 1 mm. This target had a length of 60 mm, corresponding to 575 pixels in recording, which gives a conversion factor of 9.58 px/mm.

The change in the medium from air, water, Plexiglas, and silicon used to build the AAA model force the images to have some distortion. Also, the presence of the curvature of the AAA model made the AAA geometry work as a lens. The best way to reduce this distortion is to have the same blood analog inside the AAA model. A calibration target was built and placed at the plane of measurement inside and outside of the AAA model. Two images were taken from both views as shown in Figure 3.7. A certain length was chosen from the calibration board inside and outside the AAA model. The error difference between the two measurements was found to be less than 0.2%.
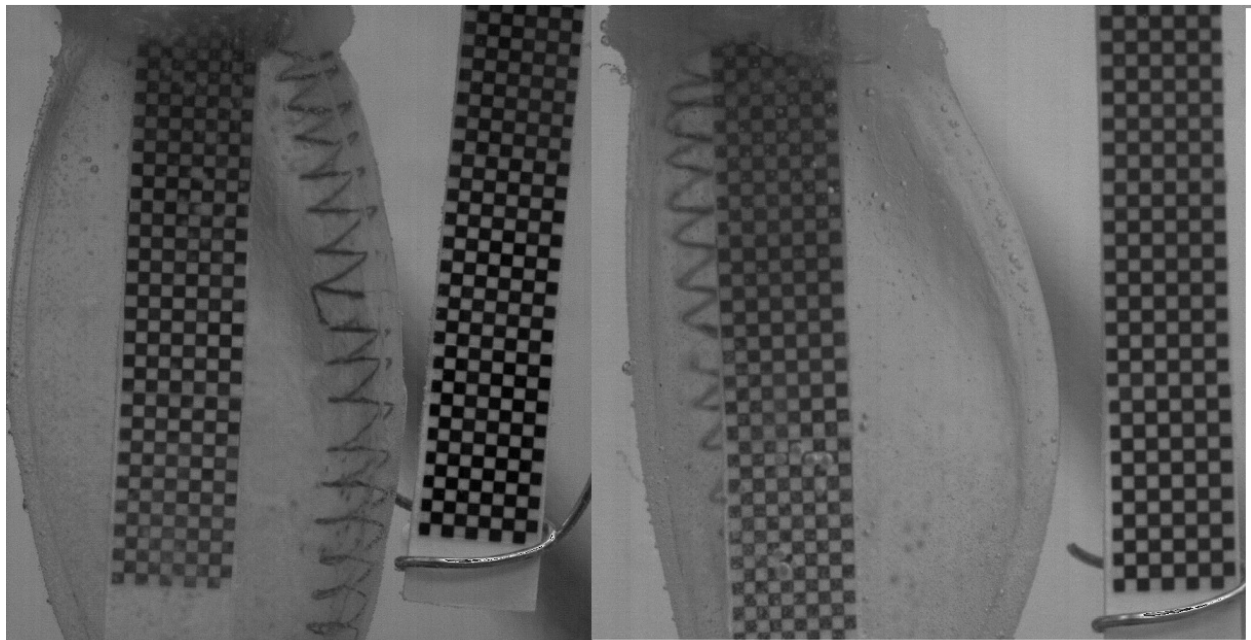
Figure 3.7: Distortion test images inside and outside AAA model for: (left) anterior plane, (right) lateral plane

- Particle Illumination, Peak Locking, and particle displacement

Light scattering due to particle size is a major factor in PIV measurements. This property is a function of the polarization and the observation angle. The morphology of the particle is also considered to be a major factor. For spherically-shaped particles, the scattering effect is estimated based on Mie's theory (Raffel et al. 2013). Figure 3.8 shows the light scattering behavior for different sizes of particles. Most of the scattered light intensity is at 180° degrees. The camera position should be mounted perpendicular to the laser sheet (90° between the laser sheet and the camera). At this location, only a factor of 10^{-5} of the initial laser intensity is reflected. This shows the importance of using a strong light source. Figure 3.9 shows some of the raw images with particles.
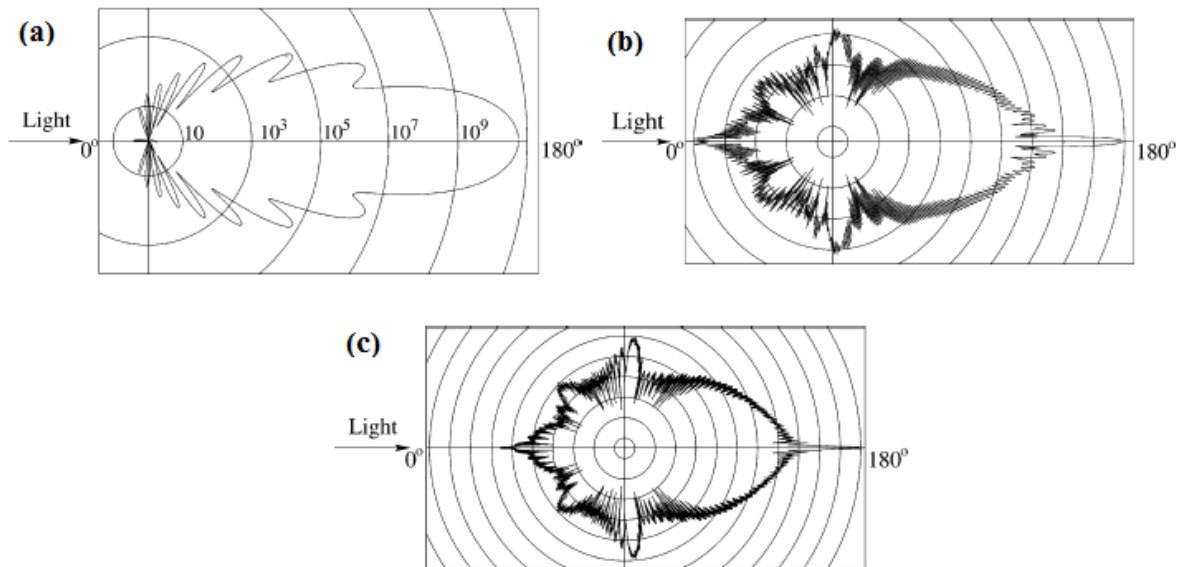
Figure 3.8: a) light scattering for a 1μm particle, b) light scattering for a 10μm particle c) light scattering for a 30μm particle (Raffel et al. 2013)
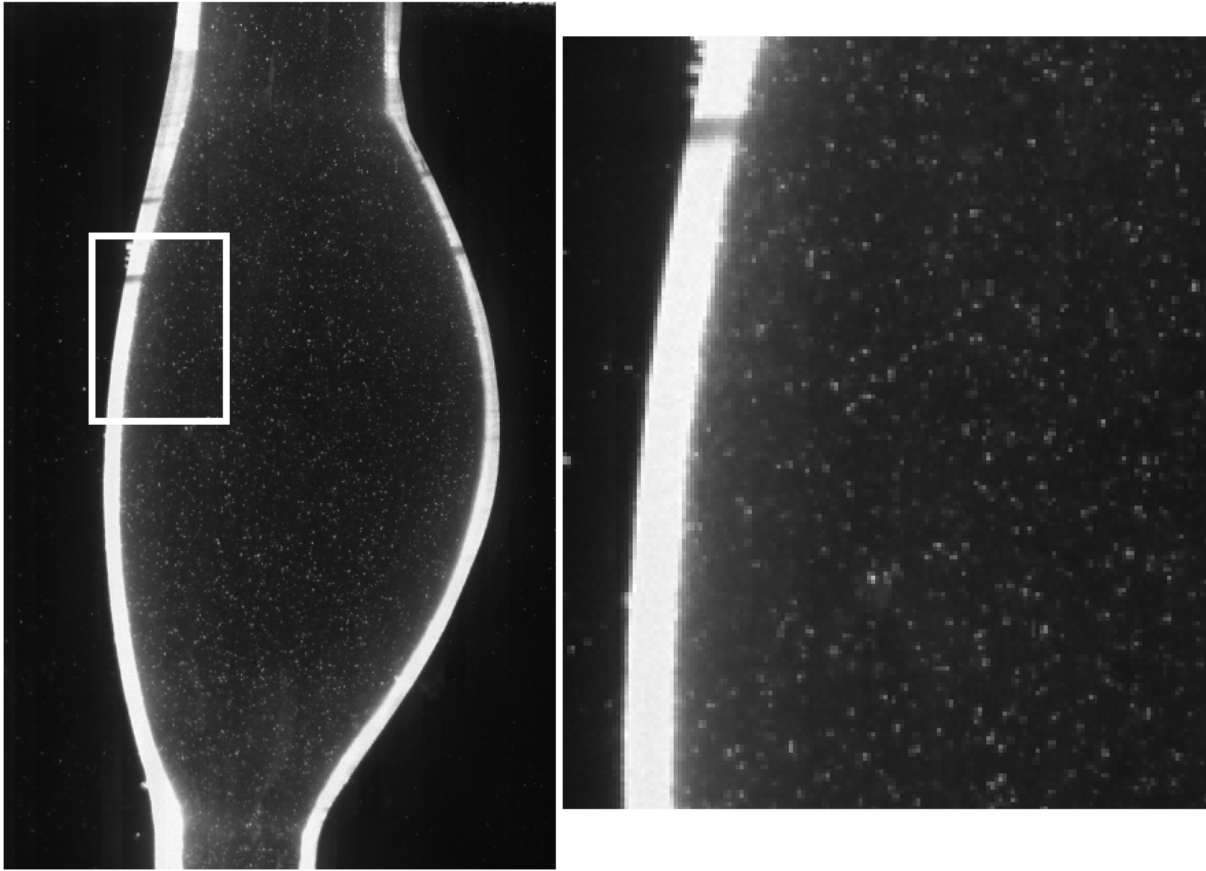
Figure 3.9: Raw image taken by the CCD-Camera

The seeded particles in the image captured by the CCD camera should be between 2 to 6 pixels to estimate the subpixel displacement (Adrian and Westerweel 2011). For this experiment, this criterion was archived by having the particle image size be around 3 pixels. If the size of the particles is too small (less than 1 pixel), peak-locking effects will appear, meaning the estimated displacement vector will be biased towards integer pixel values, and as a consequence, this will increase velocity uncertainty. This effect was minimized by performing a subpixel interpolation. In the current post processing software (Davies 7.2).

To avoid correlation errors due to in-plane displacement, particles should move less than a quarter

of the interrogation region (Keane and Adrian 1992). However, the nature of pulsatile flow forces cause significant variations in displacement. Particle displacements in all measurements were between 1-11 pixels per interrogation region.

- PIV system

Table 3.2: Specifications of the PIV system

Laser	Nd:YLF laser (Litron Lasers, UK) Maximum pulse energy: 10 mJ Repetition rate: 20 kHz Wavelength: 527 nm
Camera	Phantom v9.1 camera (Vision Research, Stuart, FL, USA) 1,000 frames per second, 14-bit, at a maximal resolution of 1,632 *1,200 pixels.
Camera Lens	Nikon AF Micro-Nikkor 60 mm f2.8 D
Software	DaVis 7.2. (LaVision GmbH, Germany)

- PIV settings

The settings for all measurements were the same in terms of camera, laser settings, post-processing and triggering points. The only difference between the NC and LC is the time between the laser pulses. For NC, this time was chosen to be 4000 μs while for the LC, this time was 4800 μs. Prior to post-processing, a mask specifying the region of interest from the raw image was drawn where the analysis of cross-correlation is applied on the specified region. Boundaries of these regions were closer to AAA walls. The distance between the mask and the AAA wall was around 0.5 mm. Table 3.3 presents the main differences between the NC and LC.

Table 3.3: Differences between NC and LC settings

Condition	NC	LC
Cardiac cycle duration	0.8333 s	1 s
dt between laser pulses	4000 μs	4800 μs
Frequency of images	120 Hz	100 Hz
Number of images per cycle	100 pair	100 pair

The results section, which is presented in chapter 4, has three main parts: velocity snapshots, particle residence time (PRT) and shear history. In the velocity snapshots, one cycle was chosen to present the evolution of the stream lines, vorticity and swirling strength. For the PRT and shear history, seven cycles were used to estimate the results. These cycles were not time-averaged. In chapter 5, covering the implementation of the decomposition techniques, only one cycle was used for both applied techniques.

3.7 Smoothing of the Velocity Field

Time-resolved velocity measurements are usually subject to noise both in space and time. As a consequence, it is recommended to filter the velocity field prior to further, more advanced, data processing. In this work, the smoothing procedure is based on the penalized least squares method through the application of the discrete cosine transform (DCT). This method was compared to normal PIV smoothing methods like the normalized median test and was found to be more efficient even in the presence of clustered outliers (Garcia 2010). The capability of this method is illustrated in Figure 3.10.
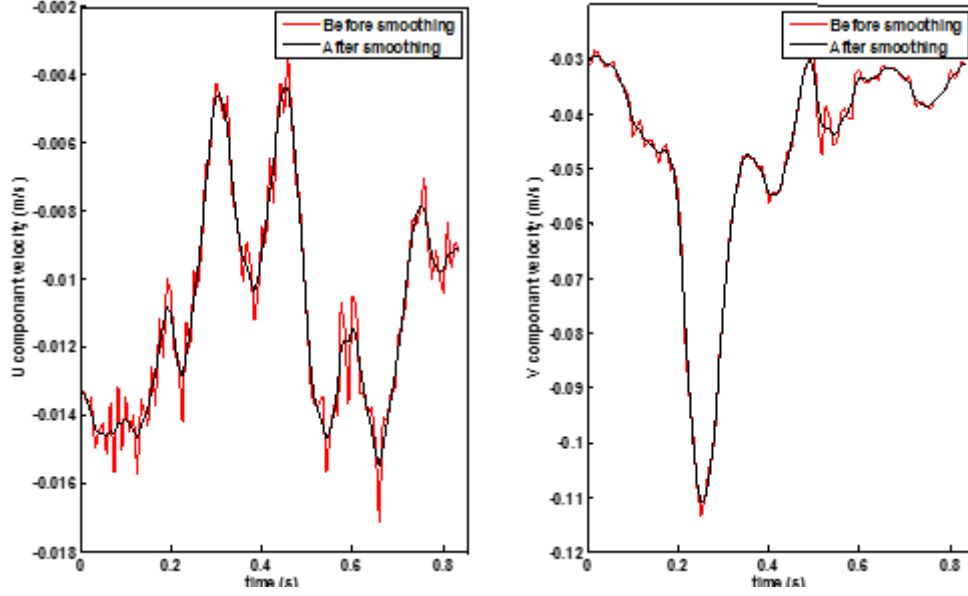
Figure 3.10: Difference between original velocity fields (U and V components) before and after smoothing using the discrete cosine transform

3.8 Vorticity and swirling strength(λ_2)

Vorticity and swirling strength were calculated based on the fourth-order compact Richardson extrapolation scheme: one of the most accurate and stable methods for evaluating derivatives with PIV data (Etebari and Vlachos 2005). The equation is defined as:

$$\frac{du}{dx_i} = \frac{1}{A_r}\sum_{k=1,2,4,8} A_k \frac{u_{i+k}-u_{i-k}}{2k\Delta x_i} \tag{3.2}$$

where A_r, A_k are constants for the Richardson extrapolation and x is the spatial resolution.

Vorticity is defined as the tendency of the fluid particles to swirl. In a 2D flow it is given by:

$$\omega = \frac{\partial u}{\partial y} - \frac{\partial v}{\partial x} \tag{3.3}$$

where u, v are the velocities and x, y are the spatial coordinates.

40

The swirling strength is found from the velocity gradient tensor, which is given by:

$$\nabla u = \begin{pmatrix} \frac{\partial u}{\partial x} & \frac{\partial u}{\partial y} \\ \frac{\partial v}{\partial x} & \frac{\partial v}{\partial y} \end{pmatrix} \qquad (3.4)$$

The velocity gradient tensor can be decomposed into strain rate and rotation rate:

$$\nabla u = S + \Omega \qquad (3.5)$$

Eigenvalues of the matrix $S^2 + \Omega^2$ can then be evaluated. Negative values of the second ordered eigenvalues corresponds to location of swirling (Jeong and Hussain 1995).

3.9 Uncertainty Analysis

PIV measurements require an involvement of several subsystems, and each subsystem has its own uncertainty. Since PIV aims at determining the velocity knowing the displacement of the tracers and the time between the two laser pulses, the uncertainty associated with each one has to be identified. Nishio (2008) summarized the error sources of PIV measurements including the calibration target errors, the captured image distortion and camera recording angle, the subpixel analysis when applying a cross-correlation, the delay in the trigger, and out-of-plane velocity effects on 2D PIV.

Effect of the calibration target. The role of the CCD camera is to capture the scattered light from the fluid particles, and the displacement of the particles is estimated using a cross-correlation. The resulting displacement is expressed in pixels and has then to be converted to physical units

(typically in mm). For this purpose, a calibration target is used. In this experiment, a stainless steel calibration target with an accuracy of 0.5 mm was used. The target was placed in the same position as the laser sheet (inside AAA model). The length of the calibrated image (l_r) was 60 mm, which when converted to pixels gives $L_r = 575$ px. Therefore, the conversion factor (α) is 9.58 pixels/mm. An error could also occur when selecting the edges of the calibration target. The sensitivity can be calculated by the following equation: $\partial\alpha/\partial L_r = 0.000181$ mm/px^2. The error is likely to be around 0.5 pixels.

Since the error could be affected by 0.5 pixels at each side, the total error for the calibration board will be 0.000181 mm/px^2=1.81×10^{-7} mm/px. At a uniform flow speed of 0.06 m/s, the number of pixels associated with the movement is $0.06/\alpha*1000\approx624$ px/s, and the error in velocity is $1.81\times10^{-7}\times624=\pm1.1\times10^{-4}$ m/s (around 0.2%).

Effect of camera-laser distance. The physical distance between the calibration target and the camera could lead to an error due to a mismatch between the laser sheet and the PIV camera. As long as the camera is far from the measurement plane, the error due to this distance is limited. Since the laser thickness is about 1 mm, we can assume this difference between the calibration target and the measurement plane is around 0.5 mm. In our setup, this length (l_t) is around 500 mm and the sensitivity of this factor is then $\partial\alpha/\partial l_t=0.000197$ 1/px.

When multiplying this sensitivity with the difference between the laser sheet and the calibration target, we will have 1×10^{-7} m/px and the resulting uncertainty on the velocity will be $1\times10^{-7}\times624=\pm7.7\times10^{-5}$ m/s which is around 0.1%.

Effect of image distortion at the image edges. Camera optics might produce some distortion at the edges of the captured images as shown in Figure 3.11. This error results in a small magnification near the edges of the recorded image. However, Harris (2012) stated that this error does not reach more than 0.3% in most experiments.

Effect of measurement synchronization. The delay in the trigger is negligible since it is of the order of nanoseconds. This effect might delay the onset of measurements, but due to its small timescale compared to the snapshot timescale, it is negligible.

Post-processing errors. The main source of errors is due to mismatching of the two pair of images and subpixel analysis. Okamoto et al. (2000) stated that these errors are between 0.03 pixels and 0.2 pixels. If a particle moves from the first image to the second, to another within 1 pixel, it moved 0.104 mm=0.000104 m. For a dt of 4000 μs. The velocity of this particle would be 0.026 m/s and the error in velocity would be 0.23×0.026=±0.006 m/s which is around 10.5%.
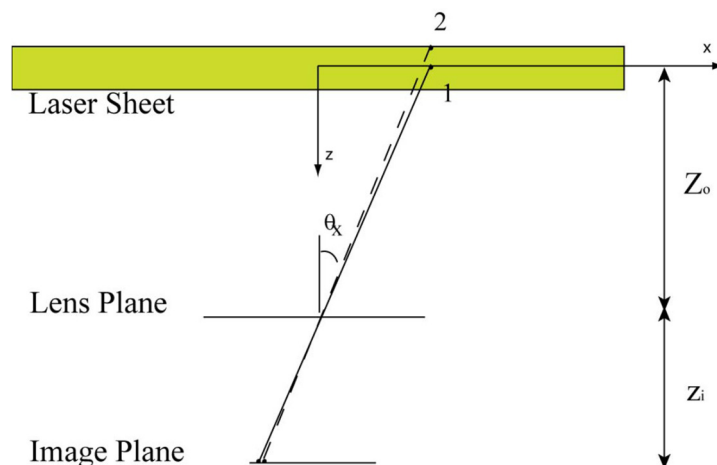
Figure 3.11: A diagram of the laser sheet and camera lens positions showing the distortion effects (Harris 2012)

The overall uncertainty of PIV measurements due to the conversation factor subpixel analysis and the image displacement is around 10%. The reported sources of errors are not the only ones that can be found in PIV applications. Other sources of errors can be found from non-homogenous particle image density, in place and out of loss of correlation, gradients of velocities, illumination variations, poor image quality, unfocused particle images. All of these sources are difficult to quantify. Therefore, they were not considered in this study. The cycle to cycle variation was estimated to be less than 5%. This error was estimated from the average flow rate at each cycle, and from the average pressure between the cycles. Table 3.4 presents the values of the pressure and the flow rate for seven cycles.

Table 3.4: Average pressure and flow variations for seven cycles.

	Cycle 1	Cycle 2	Cycle 3	Cycle 4	Cycle 5	Cycle 6	Cycle 7
Pressure (mmHg)	94.03	94.47	93.89	93.07	92.51	92.58	92.67
Flow rate (L/min)	1.614	1.653	1.623	1.641	1.610	1.616	1.645

4. FLOW ANALYSIS AND PARTICLE RESIDENCE TIME

4.1 Introduction

As outlined in chapter 2, LCs as experienced during sleeping, are associated with several risk factors. Mainly, LCs are expected to reduce the strength of the jet penetrating the AAA region and the duration of the systolic phase. Quantifying some of these effects is important. Degaute et al. (1991) conducted a study monitoring the blood pressure, the flow rate, and the heart rate in 31 healthy patients for a 24-hour period. During sleeping, the average patient's blood pressure was reduced from 120/80 mmHg to 100/55 mmHg, and the heart rate from 72 bpm to 60 bpm. The flow rate of the blood was also reduced by around 20% compared to NC (Khatri and FreIs 1969). The experimental setup described in Chapter 3 was adjusted to simulate the specific flow rate and pressure conditions for NC and for LC. Figure 4.1 shows the resulting pressure and flow waveforms for both cases. Particle image velocimetry measurements were performed in two orthogonal planes as displayed in Figure 4.2. In this chapter, the comparison between flow characteristics at NC and LC are discussed in terms of velocity field (streamlines), vorticity field, particle residence time and shear stress history of simulated particle traces in the flow stream.
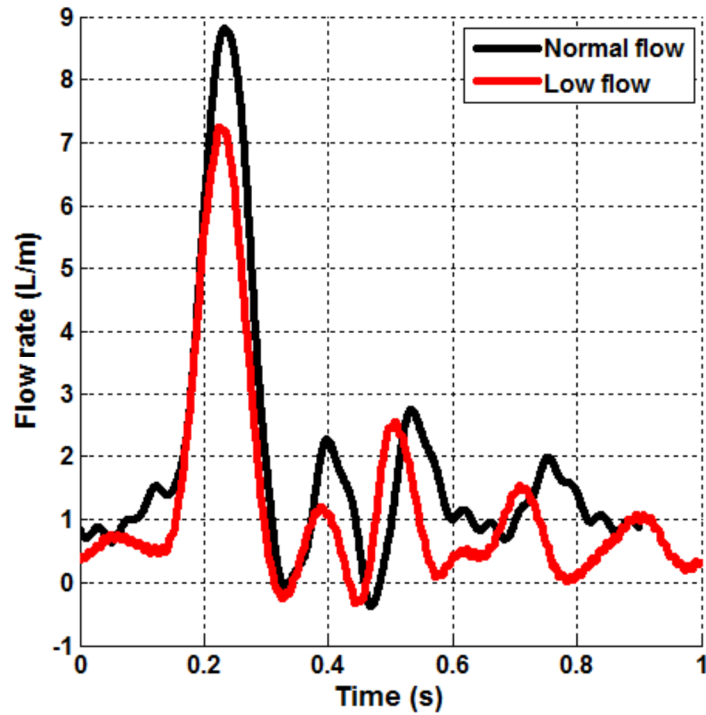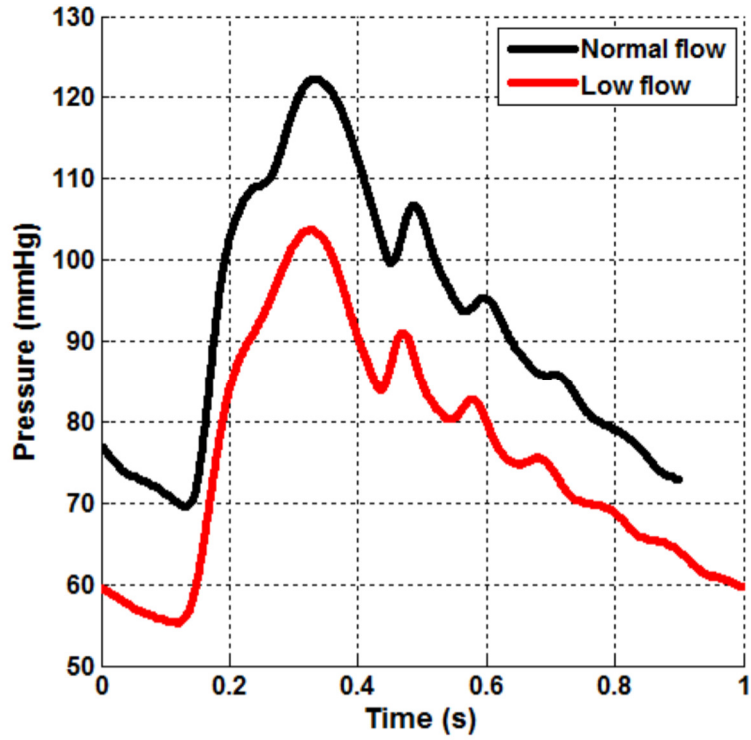
Figure 4.1: Pressure (top) and flow rate (bottom) waveforms during the cardiac cycle for the NC and LC
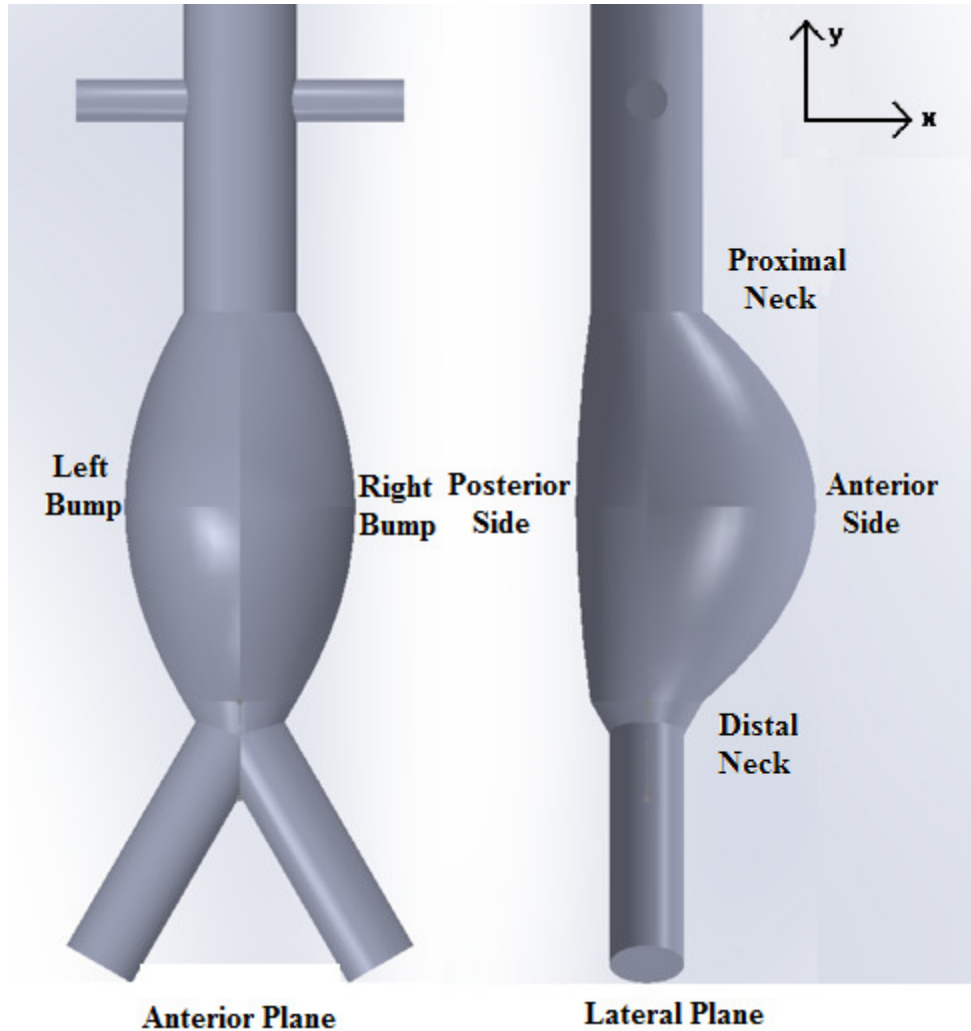
Figure 4.2: A representation of the two orthogonal planes used for particle image velocimetry measurements. Left: anterior plane; Right: lateral plane

4.2 Streamlines and Vorticity for the Normal Flow Condition (NC)

Lateral plane: Figure 4.3 presents four instants in the systolic period of velocity streamlines, vorticity, and swirling strength in the lateral plane for NC. At the beginning of the cardiac cycle (just before systolic period, figure 4.3 a1, b1, c1), the flow was characterized by slow motion of fluid near the anterior bulge. It is separated by a swirling region separating fluid affected by the expansion of the AAA and the fluid moving toward the AAA exit. The fluid affected by the sudden

47

expansion forms a large recirculation zone with low velocities. Due to these low velocities, vorticity and swirling strength cannot be detected. At the early stage of systole as illustrated in (Figure 4.3 a2, b2, c2), the strength of the generated vortex was reduced due to an increase in acceleration of the upstream flow resulting from higher levels of pressure and flow rates, as well as the flow beginning to attach to the AAA wall. At the peak of systole (Figure 4.3 (a3)), the velocity field becomes fully attached to the AAA wall and is directed towards the exit of the AAA. Maximum velocity at the entrance region was found to be around 0.36 m/s. Early deceleration shows a separation of the inlet flow and a formation of some swirling close to the proximal neck of the AAA.

During late deceleration (Figure 4.4 (a1,a2,a3)), when the flow rate becomes low, the anterior side of the AAA experiences a backflow and a reformation of the large vortex. The small peaks in diastole do not change the major behavior of the flow (Figure 4.4 (2-3)). The rest of diastole continued to have a similar trend (Figure 4.4(8)).

Figure 4.3: (a) velocity streamlines, (b) vorticity during and (c) swirling strength in the systolic period for the NC in the lateral plane

Figure 4.4: (a) velocity streamlines, (b) vorticity during and (c) swirling strength in the diastolic period for the NC in the lateral plane

Anterior plane: Figure 4.5 presents the evolution of velocity streamlines, vorticity, and the swirling strength for the NC. Though the plane is symmetrical, the inclination of the inlet jet prevents symmetrical flow structures to develop. The asymmetry is mostly due to the effect of the aortic arch (see Seed and Wood (1971) and Kilner et al. 1993)). At the beginning of systole (Figure 4.5 a1, b1, c1), a slow stream of fluid traveled through the AAA region and caused two vortices in the right and left bulges. Since the flow was inclined toward the left bulge, the location and the strength of the left vortex was higher. At the early stage of the cycle (Figure 4.5 a2 , b2,c2), the strength of the inflow jet was not sufficient to generate fully attached streamlines to the AAA walls, causing a small separation of the flow close to the left and right bulges. The peak of the systolic region (Figure 4.5 a3, b3, c3) is comparable to the lateral plane where velocity vectors are attached to the wall and directed towards the iliac arteries (Figure 4.4 a4, b4, c4).

The general behavior of the flow in the diastolic period is almost the same for the four instants as illustrated in Figure 4.6. What can be seen from the four snapshots is the migration of the two vortices until they vanish. Their migration lasts for the whole cycle until a new pair start to form at the proximal neck. Some swirling strengths near the bulges were not detected properly with the vorticity contours and the swirling strength contours.

Figure 4.5: (a) velocity streamlines, (b) vorticity during and (c) swirling strength in the systolic period for the NC in the anterior plane

Figure 4.6: (a) velocity streamlines, (b) vorticity during and (c) swirling strength in the diastolic period for the NC in the anterior plane

4.3 Streamlines and Vorticity for the Low Flow Condition (LC)

Lateral plane: Figure 4.7 illustrates the stream lines, vorticity, and the vortical structures in the anterior plane of the AAA during the LC. The general characteristics of the flow do not change significantly. It is essential to highlight the main differences compared to the NC. At the early systole, the swirling region which separates the flow moved upstream which means it affected the entrance region. The duration of the systolic period is less than the NC. Therefore, washing of the blood stream close to the proximal edge was delayed (Figure 4.7 a2, b2, c2). Early systole (Figure 4.7 a3, b3, c3). The same phenomenon occurs of washing of the blood particles from the entire region of the AAA. The maximum velocity formed in this case at the entrance region was around 0.23 m/s. The early diastole has a similar trend as for the NC (Figure 4.7 a4, b4, c4). For the early diastolic period, a small vortex near the posterior entrance moved apart from the wall compared to the NC where it remains attached to the wall. The rest of the diastolic period is characterized by a small vortex close to anterior entrance in addition to the large vortex in the anterior region of the AAA (Figure 4.8).

In terms of vortical structures, the large vortex created near the proximal neck has been reduced, and its presence during the cardiac cycle was eliminated compared to the NC. The shear layer developed during most of the systolic period tends to be more confined close to the posterior wall. *Anterior plane*: The flow structure in the LC (Figures 4.10-4.11) also holds similar trend as for the NC. However, jet strength was reduced. Therefore, the vortices near the two bulges have lower strength compared to the NC. Since both cases do not display major differences, more advanced methods to compare the LC with the NC are required and will be outlined in the following sections.
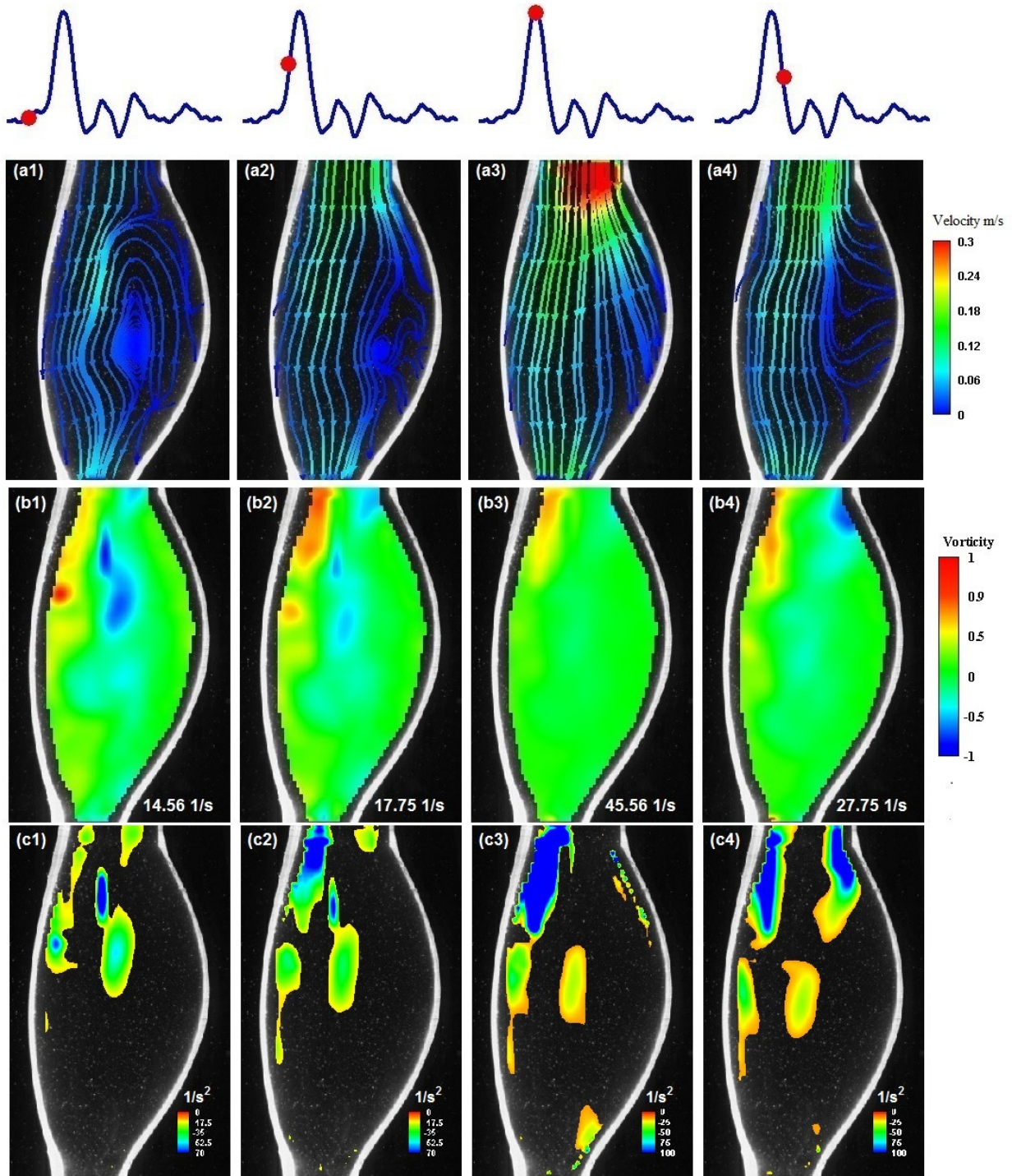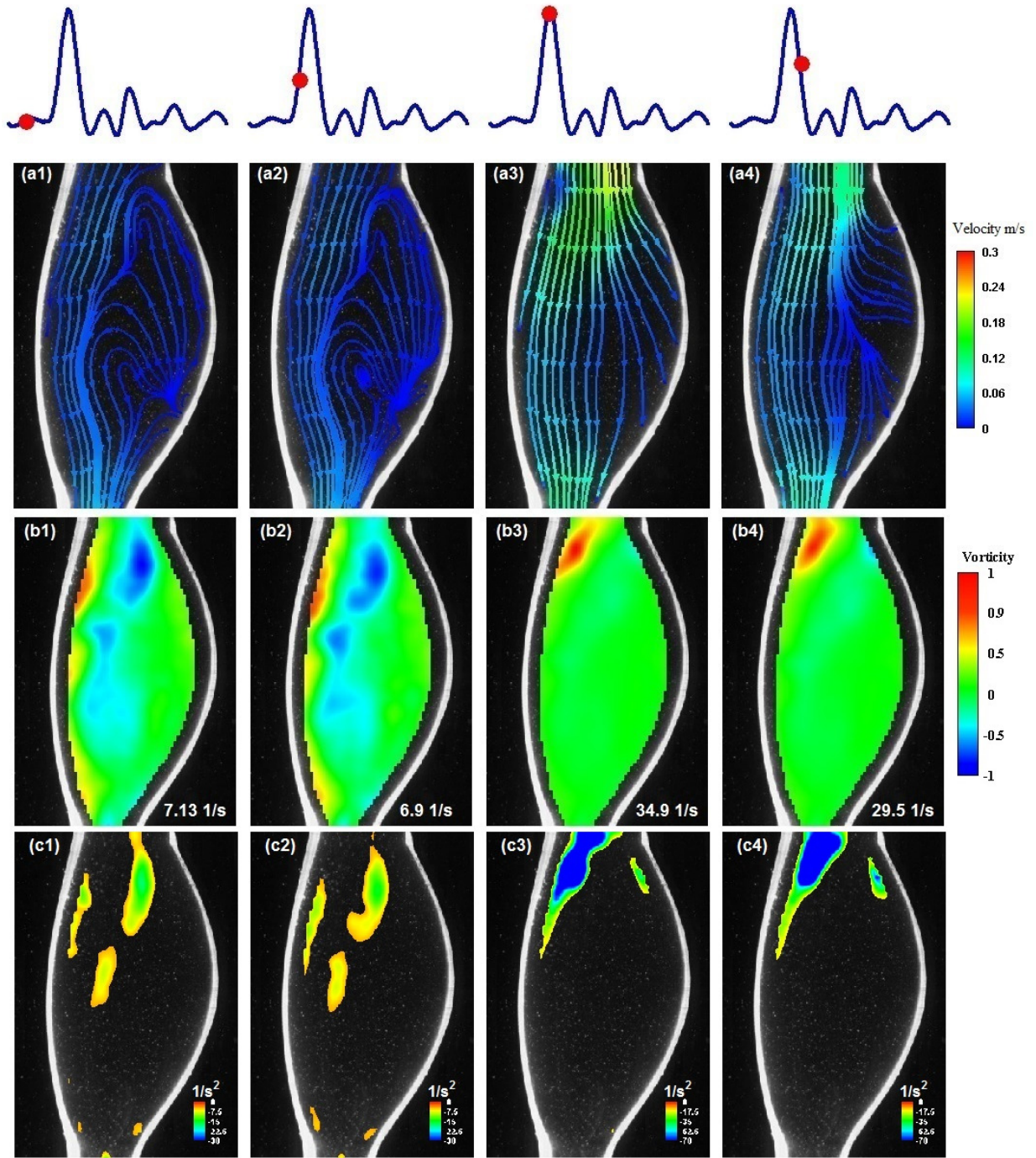
Figure 4.7: (a) velocity streamlines, (b) vorticity during and (c) swirling strength in the systolic period for the LC in the lateral plane
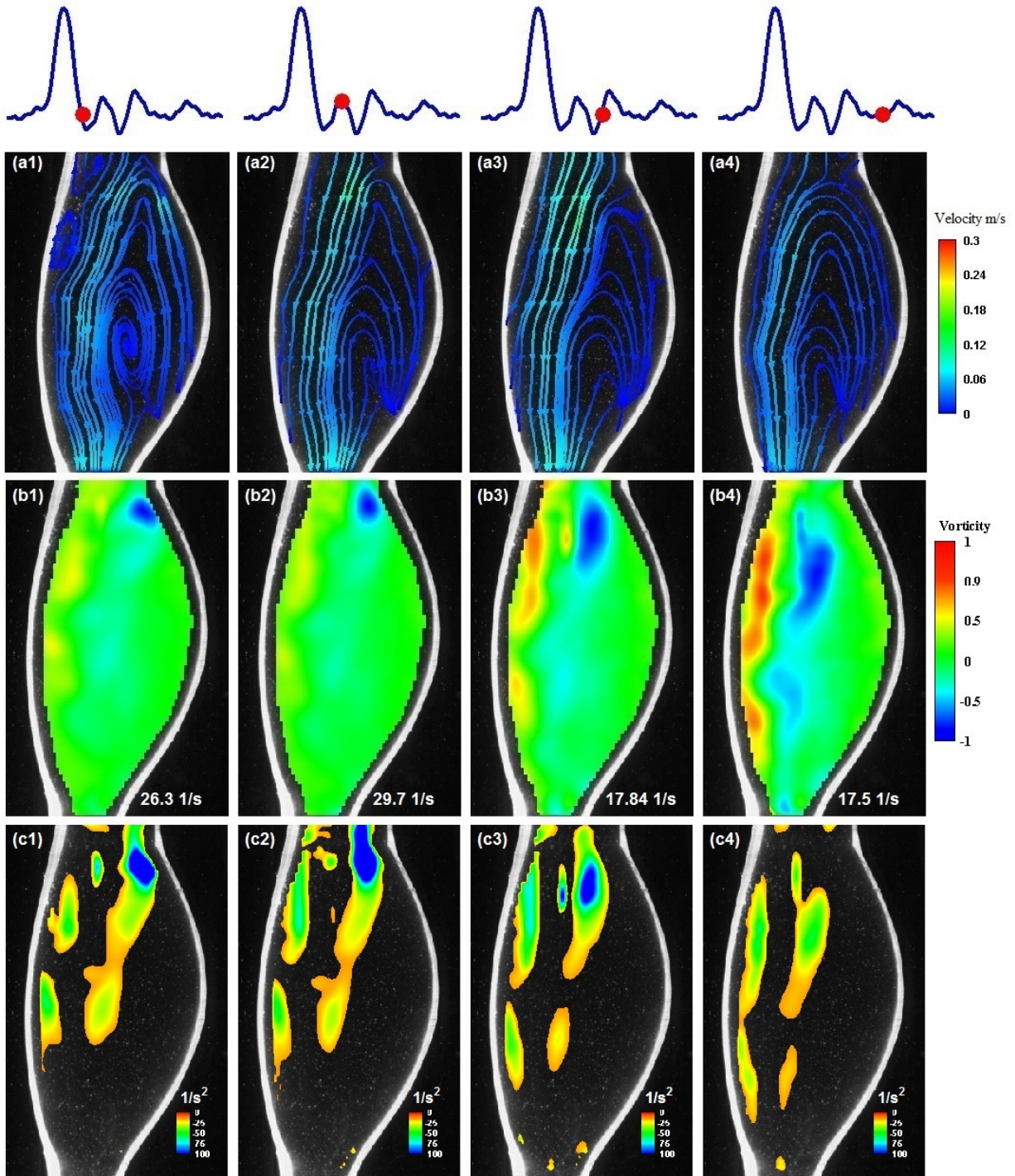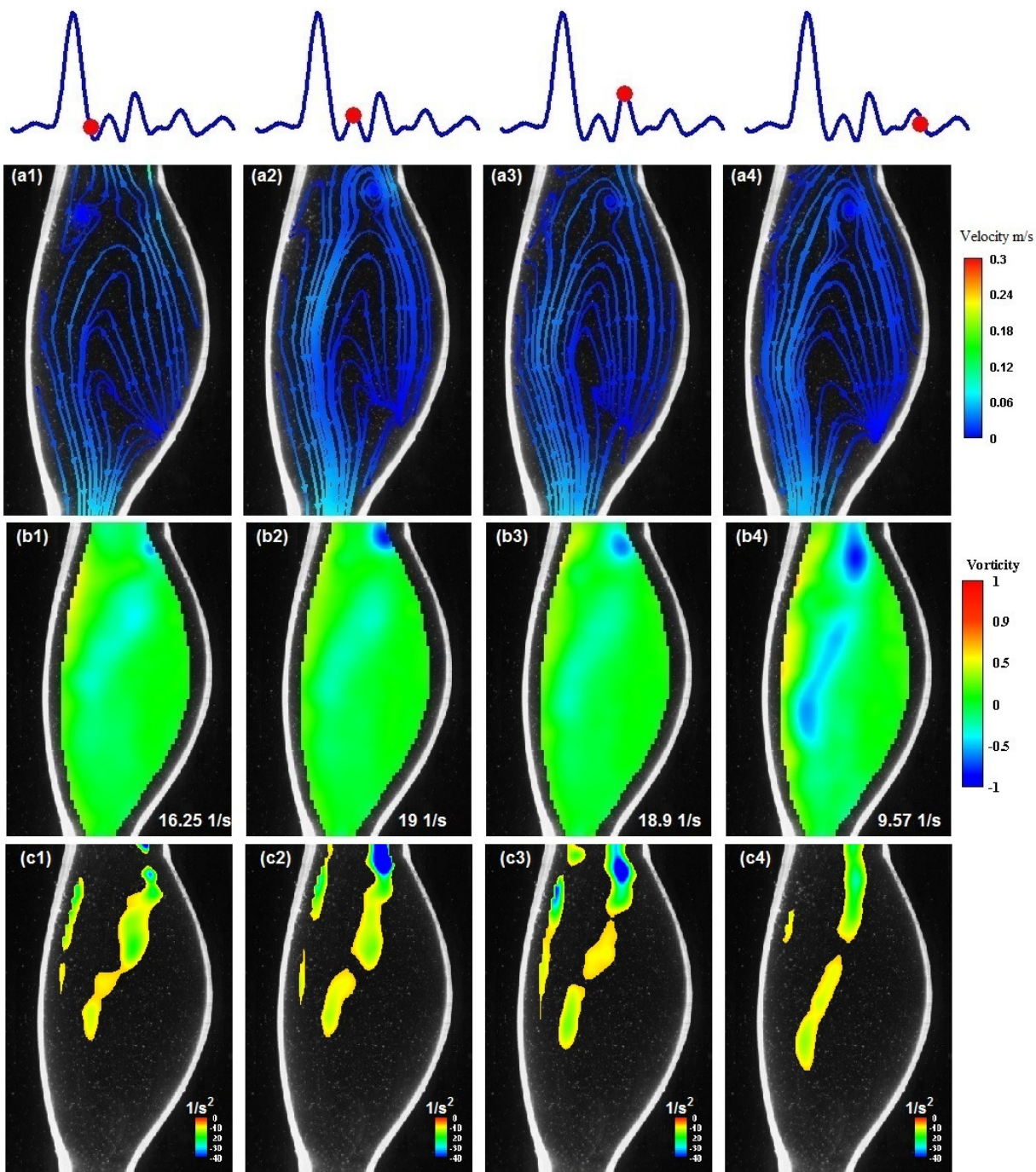
Figure 4.8: (a) velocity streamlines, (b) vorticity during and (c) swirling strength in the diastolic period for the LC in the lateral plane
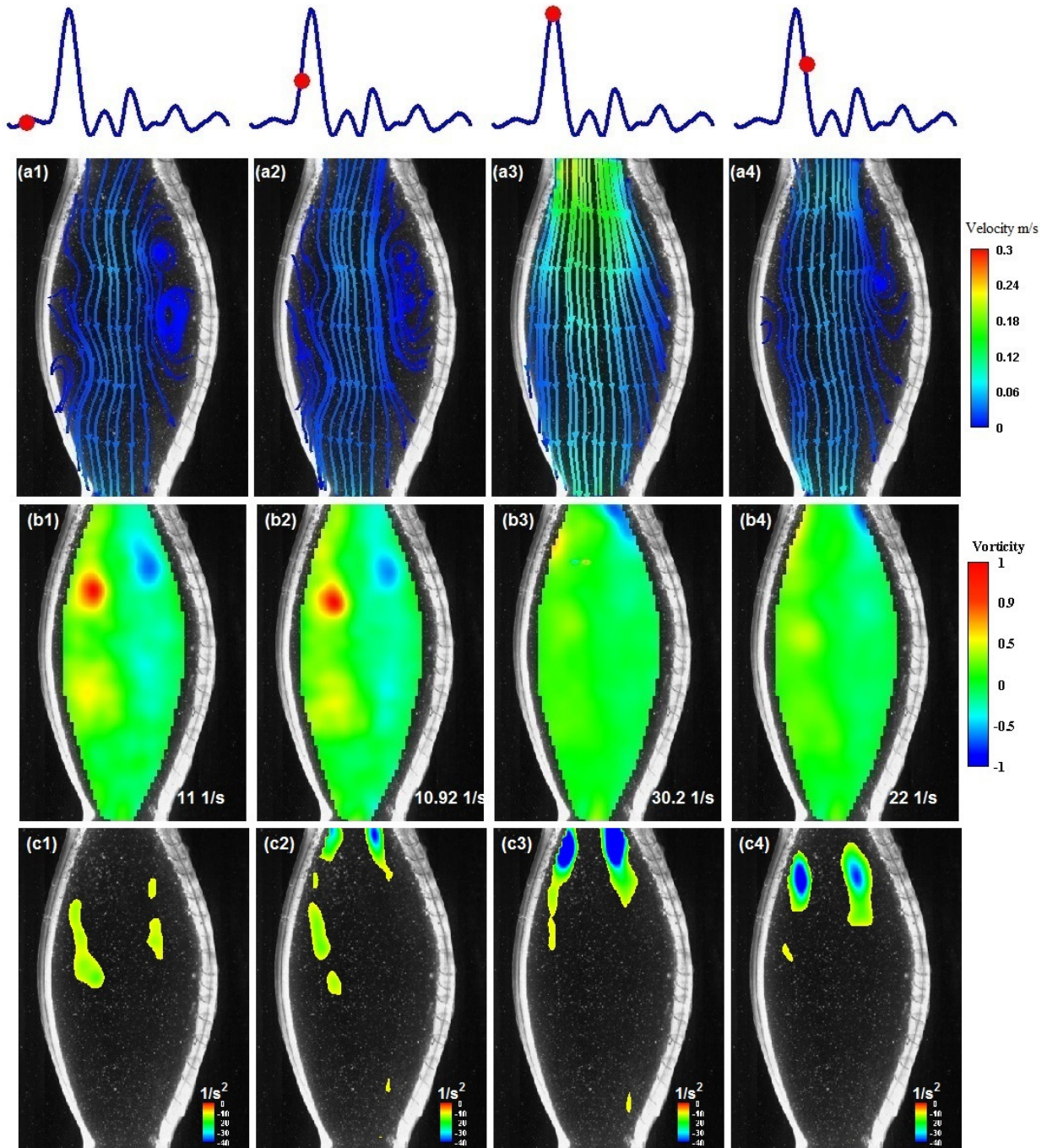
Figure 4.9: (a) velocity streamlines, (b) vorticity during and (c) swirling strength in the systolic period for the LC in the lateral plane
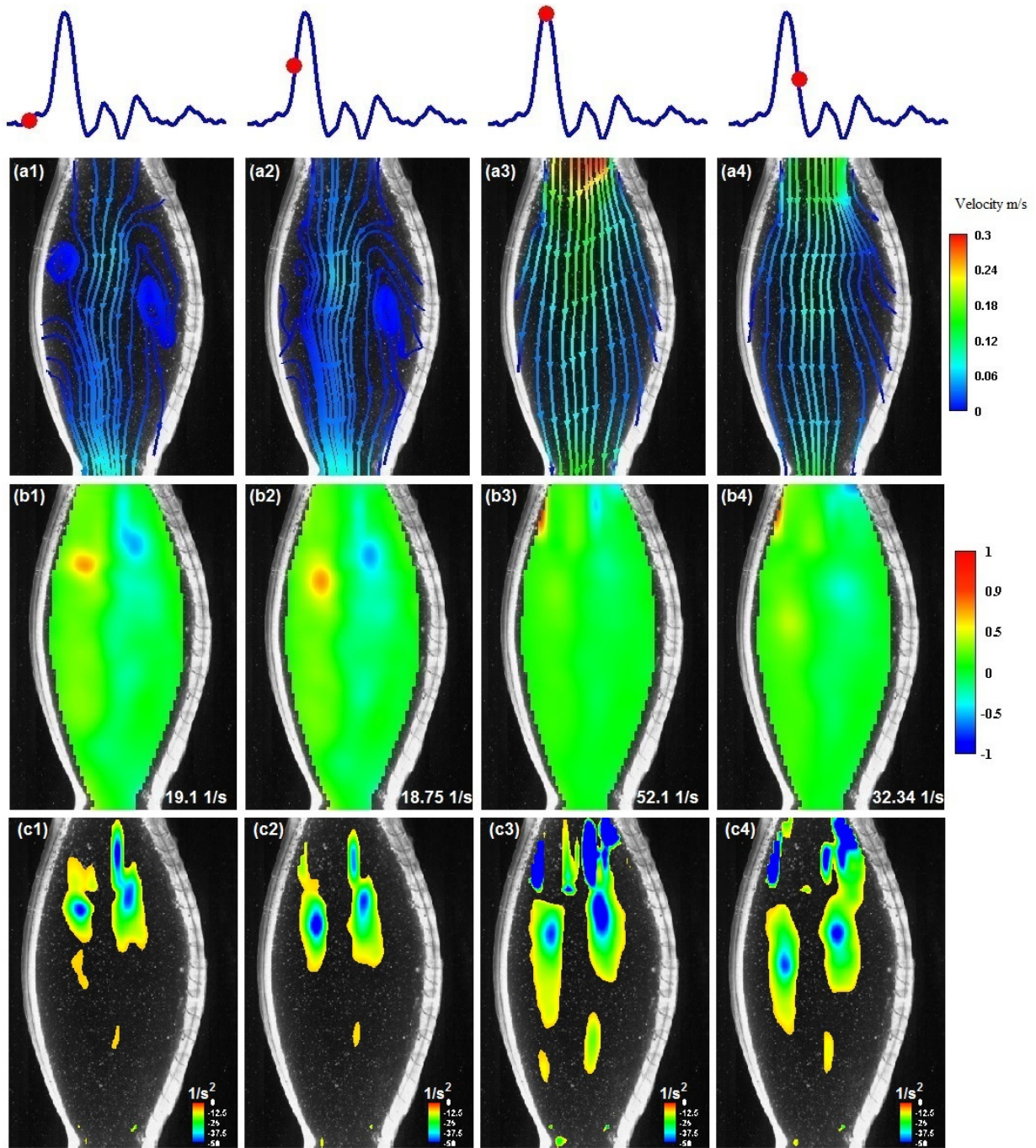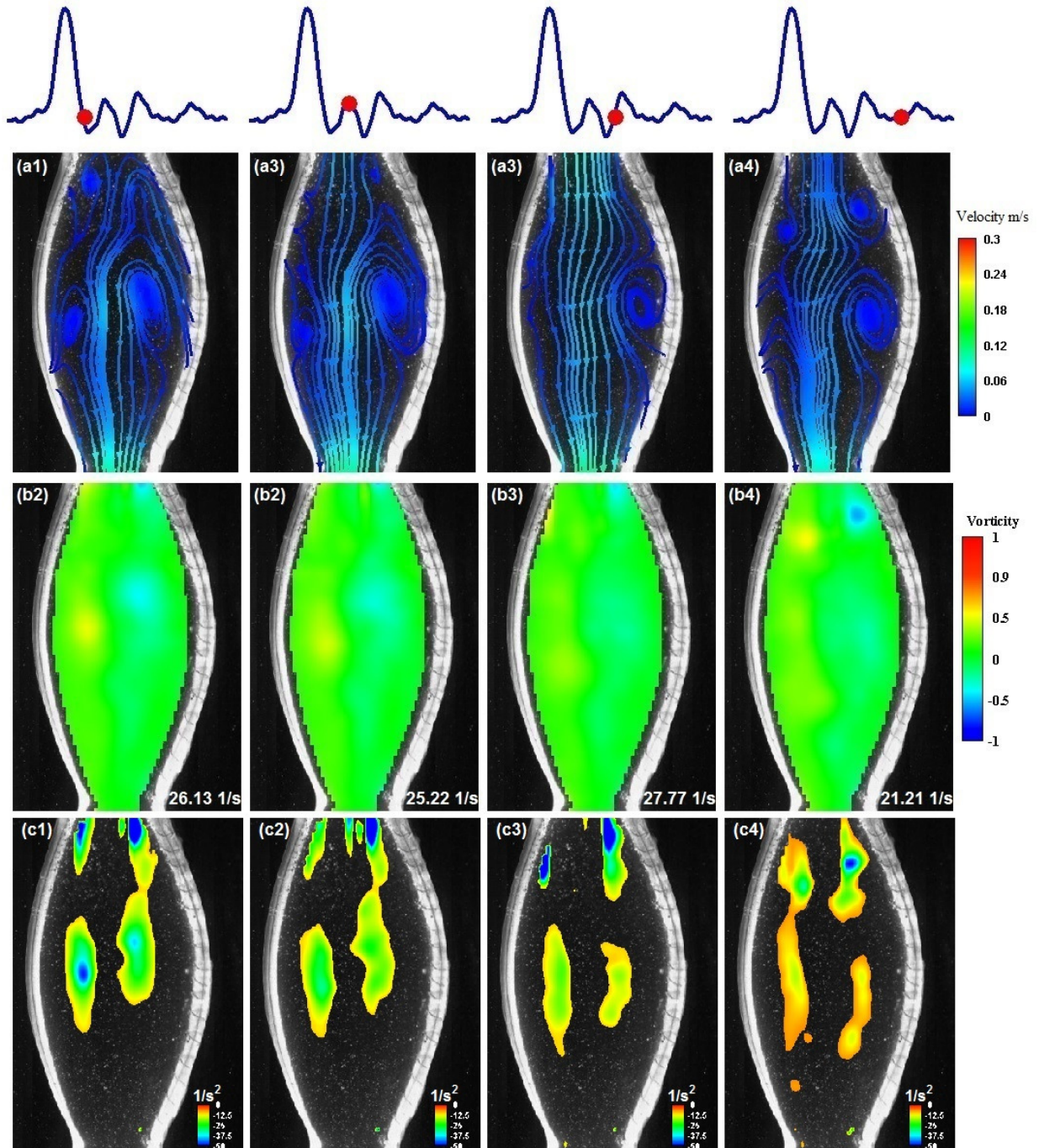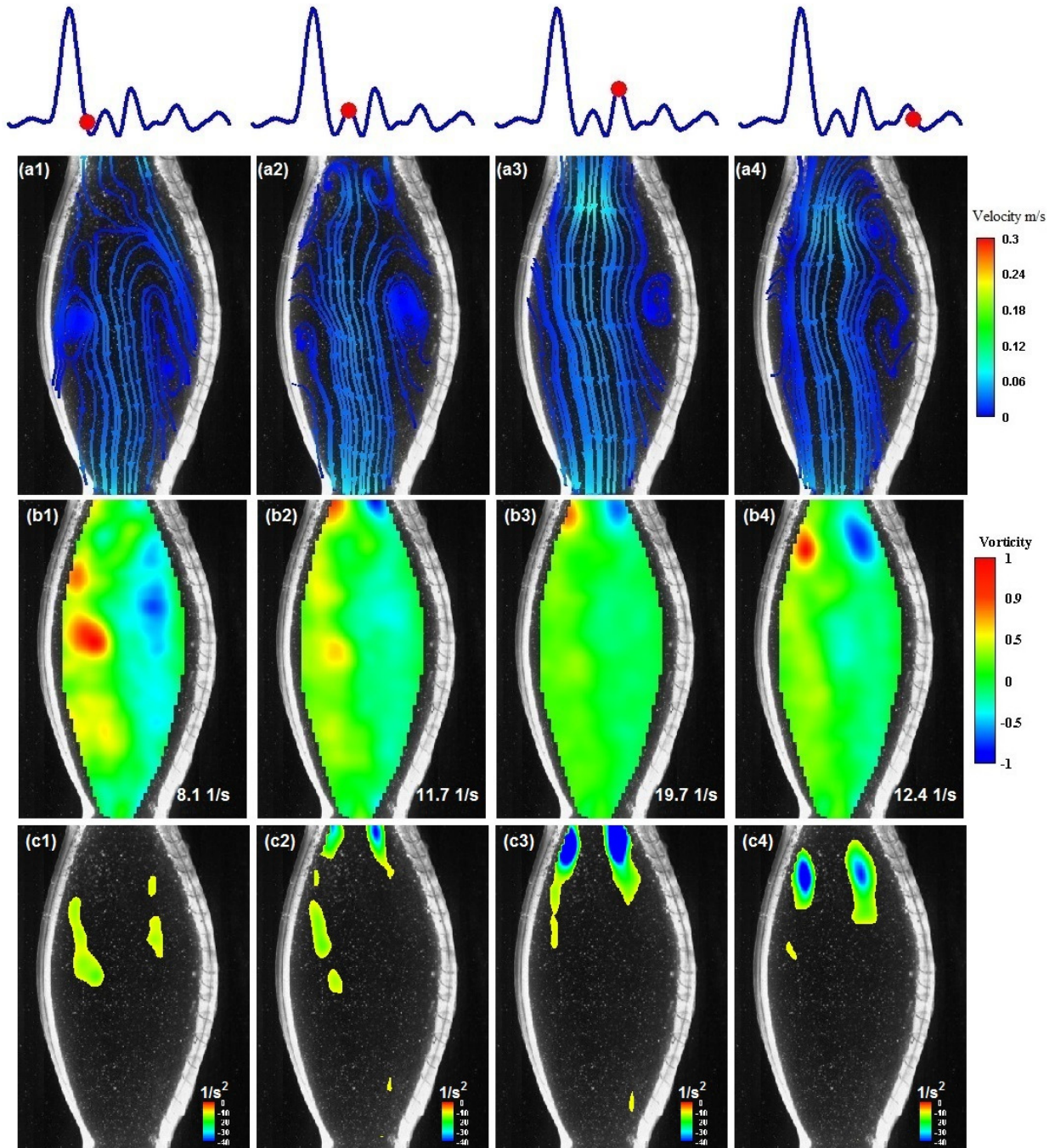
Figure 4.10: (a) velocity streamlines, (b) vorticity during and (c) swirling strength in the diastolic period for the LC in the anterior plane

4.4 Particle Residence Time (PRT)

The particle residence time is the time taken by a specific blood particle to travel inside the AAA region. This time is evaluated by inserting a number of particles at the beginning of the processed cycles and tracking their movement over a relatively long period of time. The new position of the particle is estimated based on the weighted average of the four neighboring velocities based on a bilinear interpolation function:

$$X_n = X + U\Delta t \tag{4.1}$$

Where X_n is the new position of the particle and X is the old position. U is a weighted average of the four neighbor velocities as presented in Figure 4.11 and Δt is the interrogation time step.
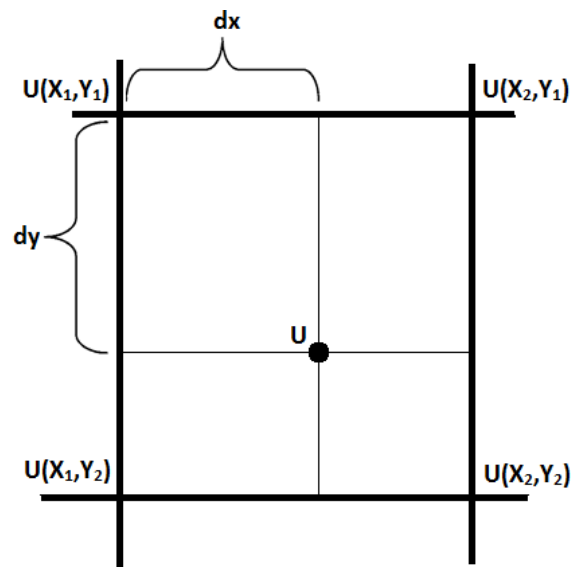
Figure 4.11: Schematic of the four neighbor points surrounding the particle location

A Matlab code was written to estimate the PRT in the AAA model under the NC and the LC. The particles have been tracked over seven consecutive cycles.

PRT was performed on time-resolved data. The PIV recording evaluates a vector field based on two images of particles at 100 instants during the cycle. Figure 4.12 shows the recording behavior of the camera and the estimated vector field. For the NC, the time between the two images is 4000 μs, and the number of vector fields is 100 per cycle. This number represents the duration of the recording, which will be 0.4s in one cycle. However, the cycle duration is 0.8333 s. The rest of the time (0.4333 s) is divided between the snapshots where each time lag before the next recording is 4333 μs. In order to have more accurate results, a linear interpolation between consecutive vector fields was performed.
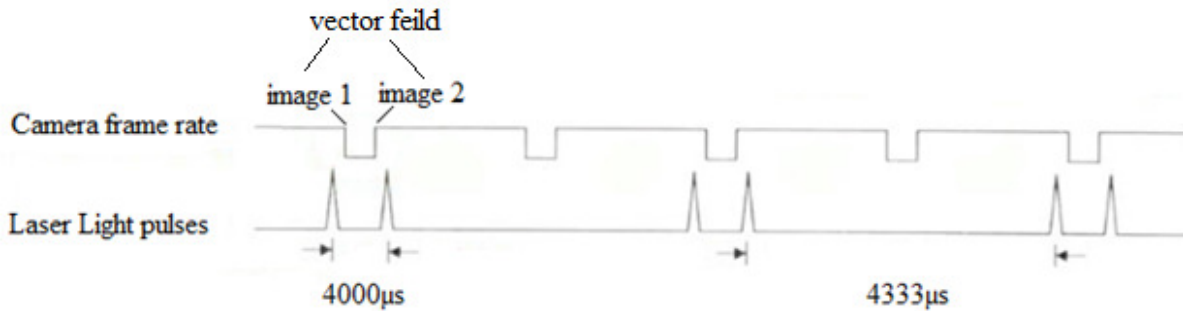
Figure 4.12: PIV recording scheme

The main advantage of the PRT code is to determine the location of the particles that did not leave the AAA after several cycles. As previously mentioned, the stasis of blood particles results in an aggregation and activation of platelets. Since the PRT code relies on particle tracers seeded in the flow, it is therefore important to evaluate if blood particles will effectively follow the flow stream. It is assumed in this analysis that blood particles do not interact with the fluid stream, and they are not affected by the neighboring particles.

To investigate this specific point, particle-laden flow theory was used and we computed the Stokes number:

$$St = \frac{\tau_p}{\tau_f} \tag{4.2}$$

where τ_p represents the time response of the blood particle and τ_f represents the characteristic time of the flow. The ratio between these two numbers gives an indication of the Stokes number. If $St \gg 1$, particles will travel on their own path, while if $St \ll 1$, particles will follow the fluid stream. The time response of the particle is estimated from the following equation (Fessler and Eaton 1999):

$$\tau_p = \left(2\rho_p + \rho\right)d_p^2/(36\mu) \tag{4.3}$$

where ρ_p is the density of the particles, ρ is the density of the fluid, d_p is the diameter of the particles, and μ is the viscosity of the fluid. Platelets are smaller in size than red blood cells, but their size does not exceed $4\mu m$ (Caro 2012). The time response is thus $\approx 4 \times 10^{-7}$ s. The characteristic time of the fluid flow is around 0.5 s. This is the time in which the vortex occupies half of the cardiac cycle. As a consequence, one obtains $St \approx 2 \times 10^{-7} \ll 1$. Therefore, we can reasonably assume that particles are following the same path as the fluid stream.

In the post-processing analysis of PIV images, a mask was drawn to specify the region of interest, see section 3.6.5. This mask has a small difference from NC to LC. The seeding particles were placed at each interrogation region within this mask. Table 4.1 presents the number of particles inserted at each case.

Table 4.1: Number of particles released at each case

	Lateral plane	Anterior plane
NC	2516	2173
LC	2453	2171

The onset of releasing the particles is critical. Some analysis has been performed to test the effect of this parameter. Particles were released at the beginning of the cycle and with a step time instant of 10. This number of instants represents 0.083 s for NC and 0.1 s for LC. Knowing that the number of instants per cycle is 100. Ten instants have been performed for each case to test the sensitivity of the onset of the releasing. Figure 4.13 presents the number of particles that left the AAA region as a function of instant during the cardiac cycle. The effect of the onset of releasing of the particles does not show major differences. The highest difference is found in the lateral plane for the normal condition (1791 and 1725). When converting the number of particles that removed from AAA domain to a percentage, the highest error is 2.7%.
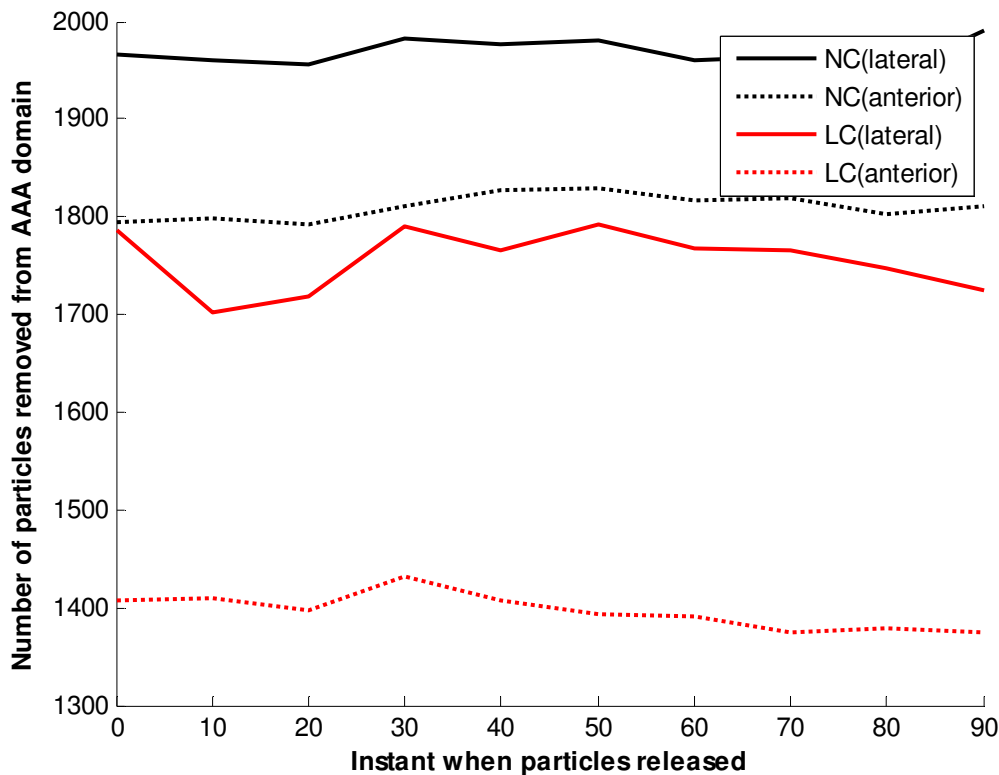
Figure 4.13: Number of particles that left the AAA as a function of onset releasing instant during the cardiac cycle

A random instant has been chosen (at snapshot 60) to show the particles stayed and left for each case. Figures 4.14 to 4.17 show the particle maps for each case at first when the particles were placed at the AAA region and after seven cycles showing the remaining particles that did not leave the AAA region. For the lateral plane in NC (Figures 4.14), particles are mainly close to the boundaries, and mainly close to the anterior side. Same behavior is found for the LC with a larger area of particles close to the anterior. In the anterior plane, particles close to the walls tended to stay for both cases. The region of the stasis of particle is also larger in the LC.
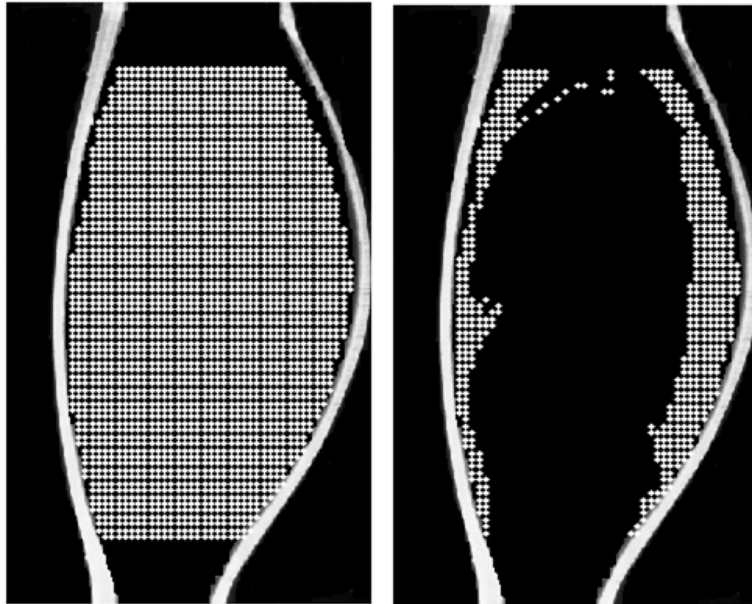
Figure 4.14: (left) Inserted particles in the AAA domain for NC in lateral plane (right) remaining particles after seven cycles
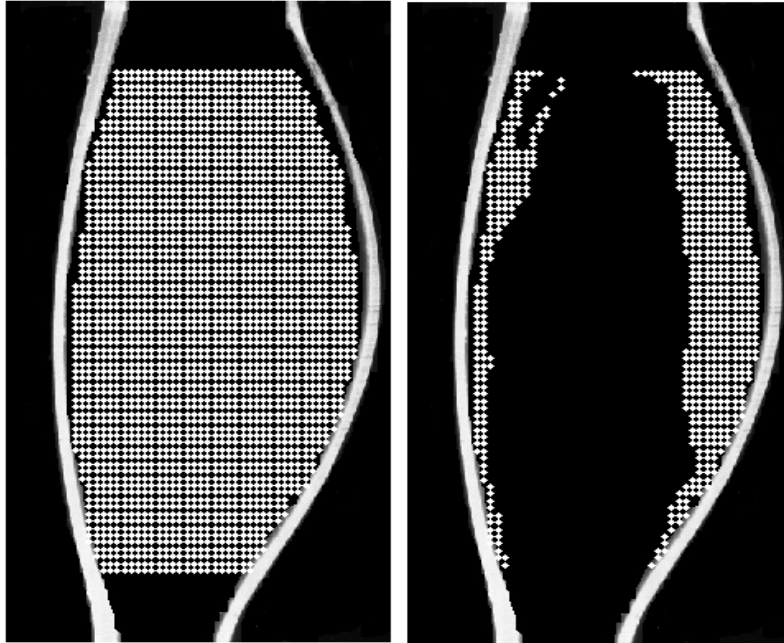
Figure 4.15: (left) Inserted particles in the AAA domain for LC in lateral plane (right) remaining particles after seven cycles
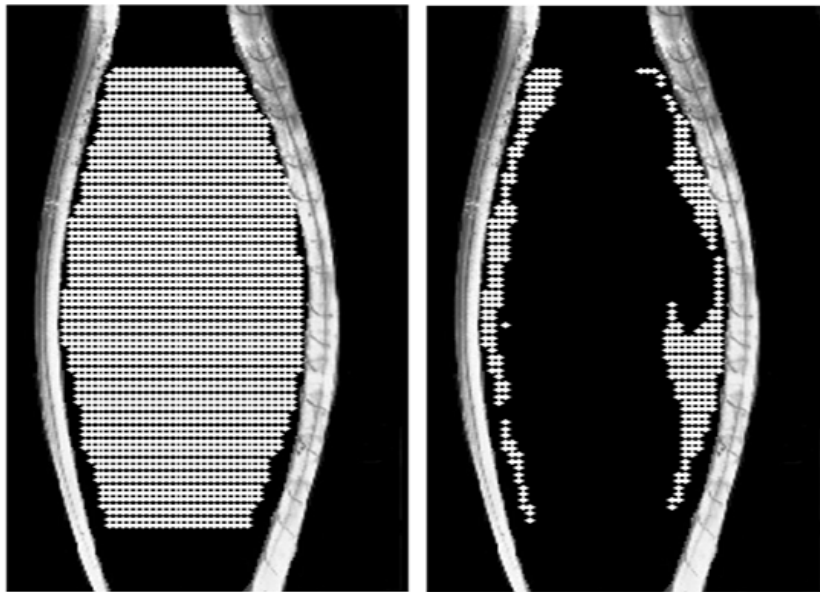
Figure 4.16: (left) Inserted particles in the AAA domain for NC in anterior plane (right) remaining particles after seven cycles
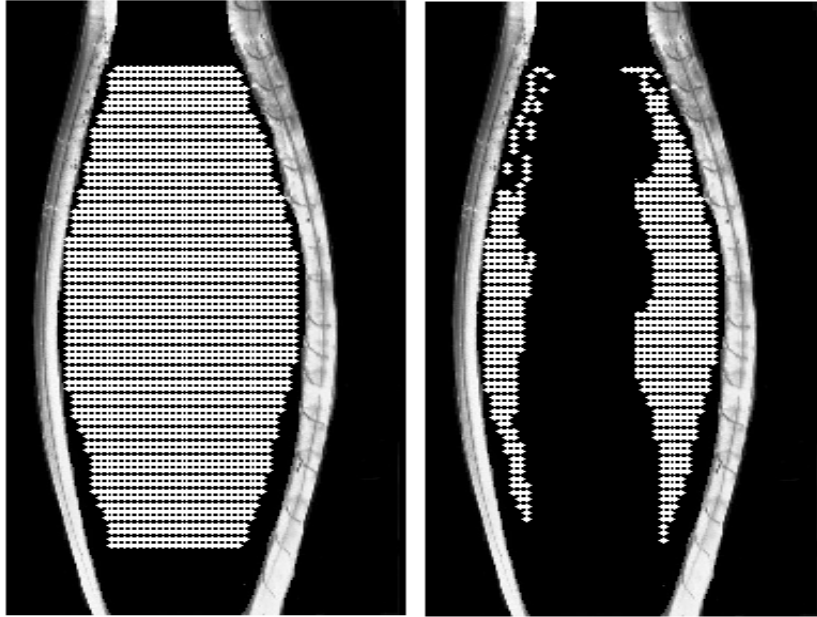
Figure 4.17: (left) Inserted particles in the AAA domain for LC in anterior plane (right) remaining particles after seven cycles

To have a clear distinction between both cases, subtraction of the particle locations was performed. The solid circles in Figure 4.18 represent the regions were the particles did not leave the AAA during the LC but left during the NC. Hollow circles show particles that left during the LC and stayed during the NC. The region where particles remained in the AAA during the LC in the lateral plane was mainly close to the anterior side. Clinically, this region has been shown to be more prone to ILT formation, see (Hans et al. 2005). The percentage of particles that left the AAA during the NC was 78% compared to 72% for the LC in the lateral plane and it was 81.5% for the NC and 64% for the LC in the anterior plane. For the LC, the strength of the systolic jet was not strong enough to displace particles from certain critical areas in the AAA. Furthermore, the LC is characterized by a shorter systolic duration relative to the duration of the cycle (17.5% vs. 21.2% compared to the NC). In the anterior plane (Figure 4.9 b), the LC pushed particles towards the edges of the AAA (left and right bulges). At these locations, the particles experienced very low velocities. They therefore tended to remain in these regions.

65
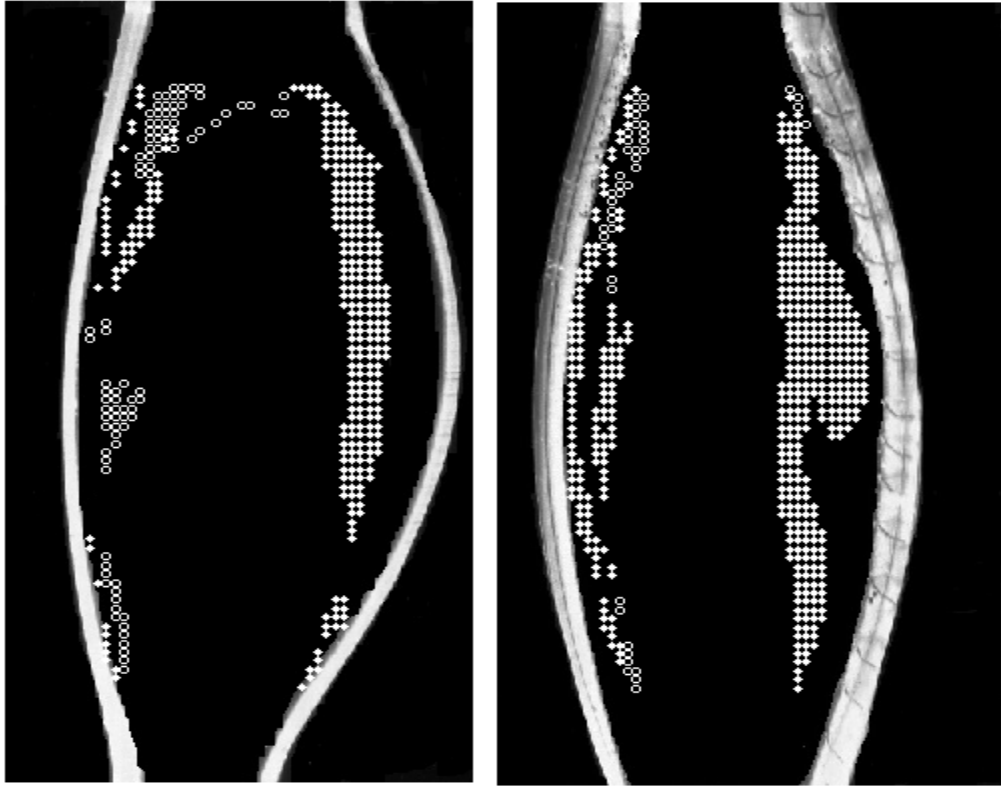
Figure 4.18: Location of particles that did not leave the aneurysm region during the LC and left during the NC (•) and location of particles that did not leave the aneurysm region during the NC and left during LC (o): (left) Lateral plane. (right) Anterior plane

4.5 Viscous Shear Stress History

When blood particles are flowing within the blood stream, they are subjected to stresses due to shearing between the blood flow layers. Platelets can be activated by both chemical and mechanical stimuli (Kleinstreuer and Li 2006). Many platelet activation models were discussed in the literature such as the cumulative power law model (Grigioni et al. 2005), the linear model (Bluestein et al. 1997), and many other models. For simplicity, a linear model has been applied to test the platelet shear accumulation and the location where particles are mostly affected by the shear. Peterson et al. (1987) stated that platelet activation is achieved when they are exposed to a

cumulative shear of 3.5 Pa.s. Although the activation of platelets may be the first step in thrombus formation, that does not mean it is an absolutely necessary step within the process.

The shear stress accumulation is estimated based on multiplying the viscous shear level exerted on a specific particle by the residence time. Yin et al. (2004) defined the platelet activation state (*PAS*) as:

$$PAS = \sum \tau_i dt \qquad (4.4)$$

where

$$\tau_i = \mu \left(\frac{du}{dy} + \frac{dv}{dx} \right) \qquad (4.5)$$

where dt is the exposure time of the applied shear. The accumulation of shear stress for each condition is evaluated based on equation (4.4). It sums up the amount of shear that each particle experiences multiplied it by its exposure time since its initial release in the flow field. Figure 4.19 illustrates a shear stress accumulation map for the NC. The most critical part in the lateral plane is near the anterior bulge. This result is consistent with PRT results since particles at this location tend to stay in this region and therefore experience more of a shearing effect. By looking at the LC in the same figure, a similar trend was found in the lateral plane with smaller amplitudes. It is worth mentioning that for both cases seven cycles were used. The anterior plane for the LC has an almost symmetrical behavior although particles in the right bulge tended to stay for longer time. In both cases, platelets do not reach their activation threshold, although in the NC, they are closer

to this level. The maximum shear level found in the NC was around 2.7 Pa.s while in the LC the maximum value of the shear level is around 2.4 Pa.s. Only seven cycles were involved in this computation. It is expected to have higher values of shear after adding more cycles where blood particles that stay experience larger shear levels.

The shear map presents what each particle experiences after the seven cycles. However, to have a better idea on how a particle behaves during the shear accumulation process, some specific particles have been selected and tracked during consecutive cycles.
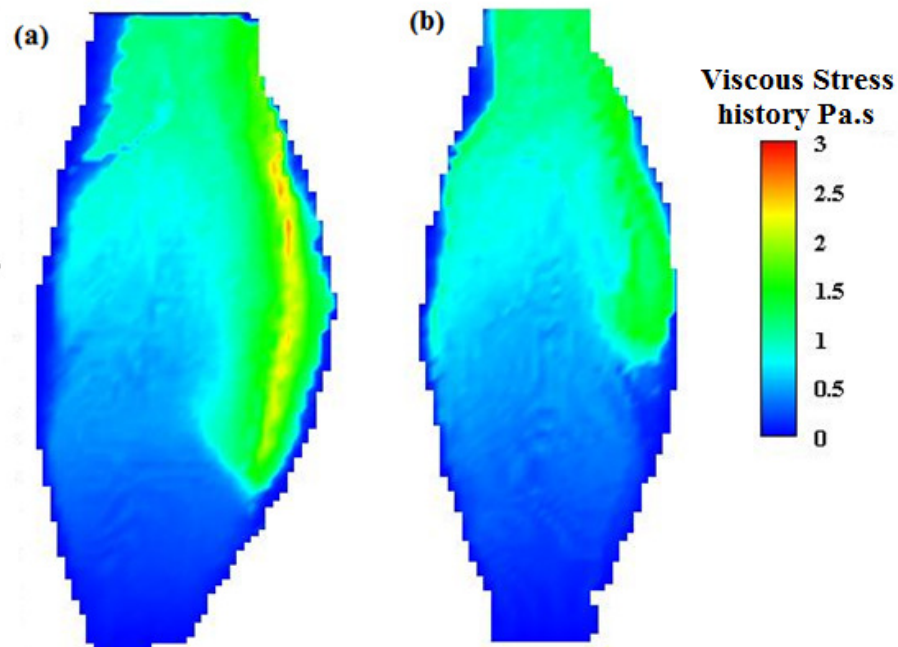
Figure 4.19: Viscous shear stress accumulation history for the NC: a) Lateral plane; b) Anterior plane
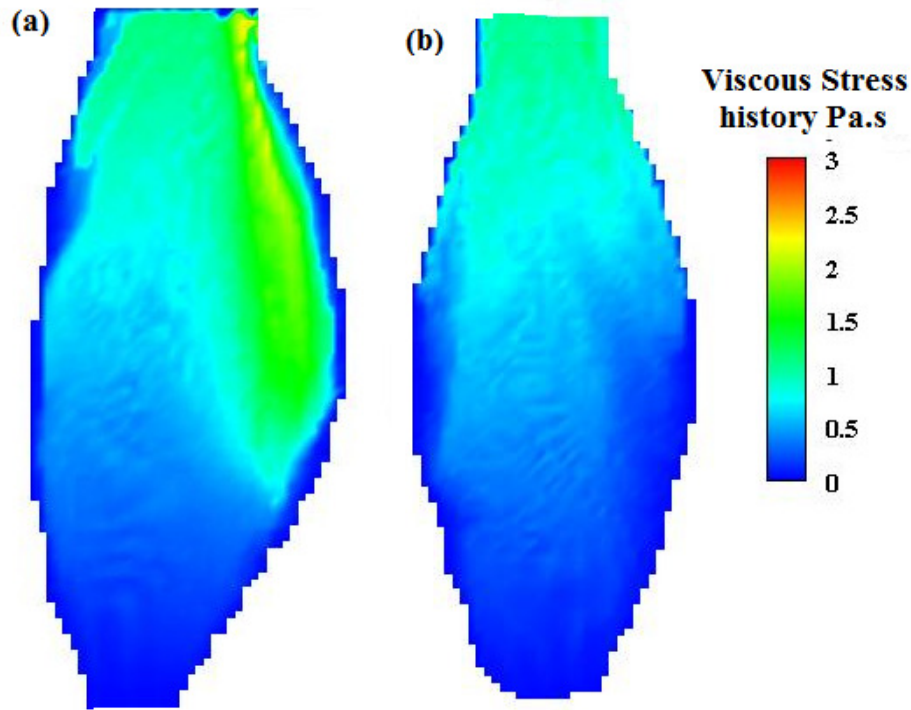
Figure 4.20: Viscous shear stress accumulation history for the LC: a) Lateral plane; b) Anterior plane

Some particles were chosen in the AAA region to evaluate the path they would take and to track their stress history. Figures 4.21 - 4.24 show instantaneous viscous shear stress applied on some selected particles for both the NC and the LC. In the lateral plane (Figures 4.21), it is clear that the most critical region was near the proximal neck, where the fluid experienced high flow separation and vortex formation. Although particles were affected by swirling, they were able to leave the aneurysm region after a number of cycles, compared to the LC where particles are almost stagnant. For the anterior plane (Figure 4.21), particles in the LC follow a straight path along the right bulge. Once they reach the entrance region, they experience low velocities forcing them to stay.

As previously mentioned, platelet activation is just the first step towards thrombus formation. Other important factors include the von Willebrand Factor (a compound contained in blood

plasma) (Shankaran, Alexandridis and Neelamegham 2003). It is activated in the region of blood stasis and helps in the adhesion of activated platelets in locations of injury. Recent studies by (Miller et al. 2010) proved that the level of the von Willebrand Factor is elevated during sleeping and is more likely to occur in men compared to women. This elevation might be one of the factors why AAA occurrence is higher in men (Isselbacher 2005).
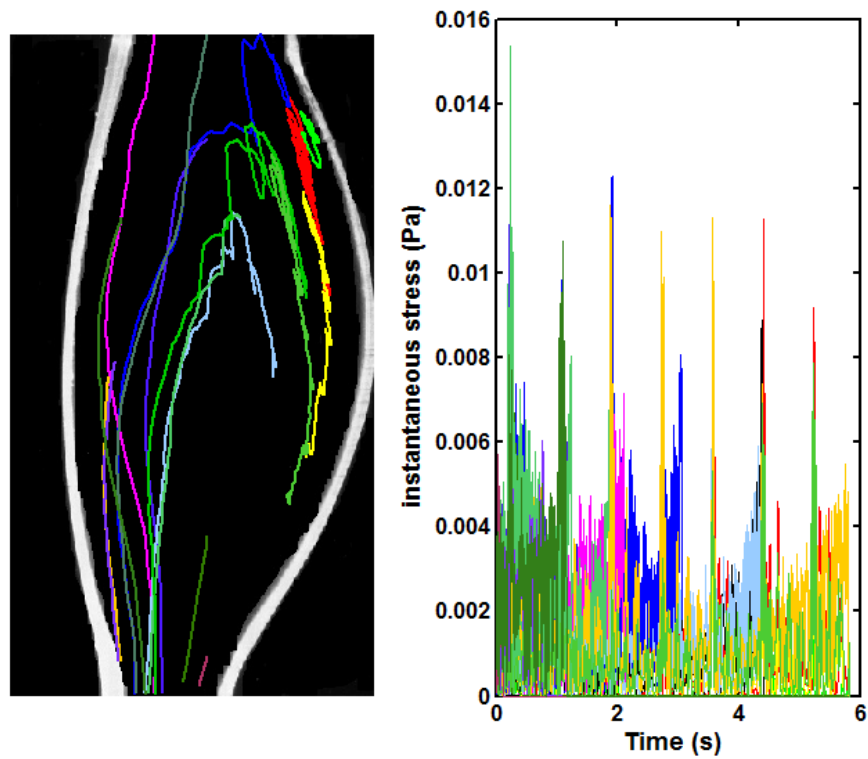
Figure 4.21: Trajectories and viscous shear stress history of some particles in the lateral plane for the NC
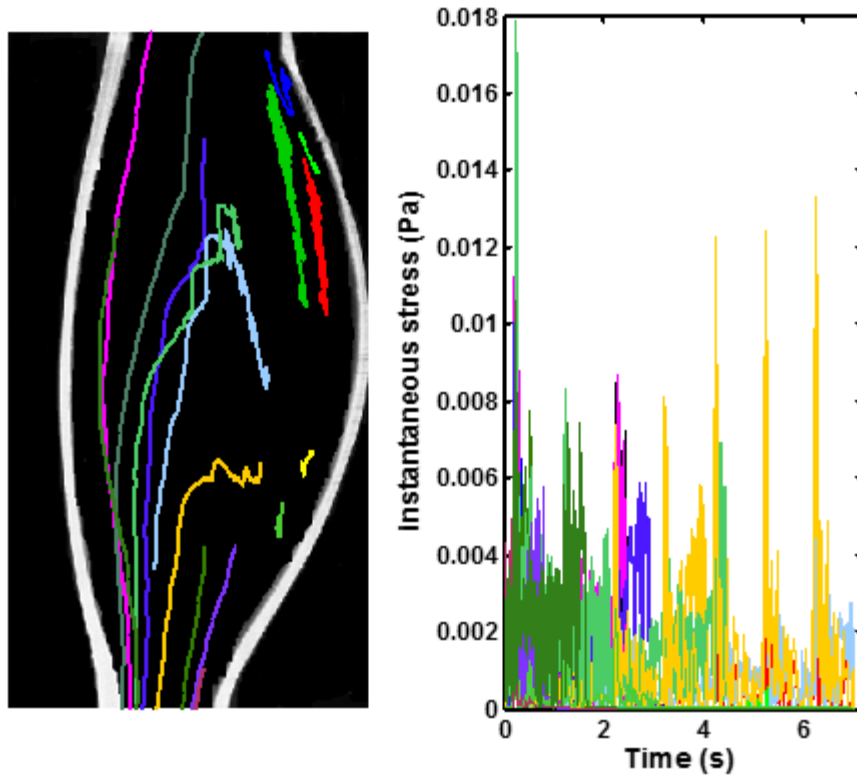
Figure 4.22: Trajectories and viscous shear stress history of some particles in lateral plane for the LC
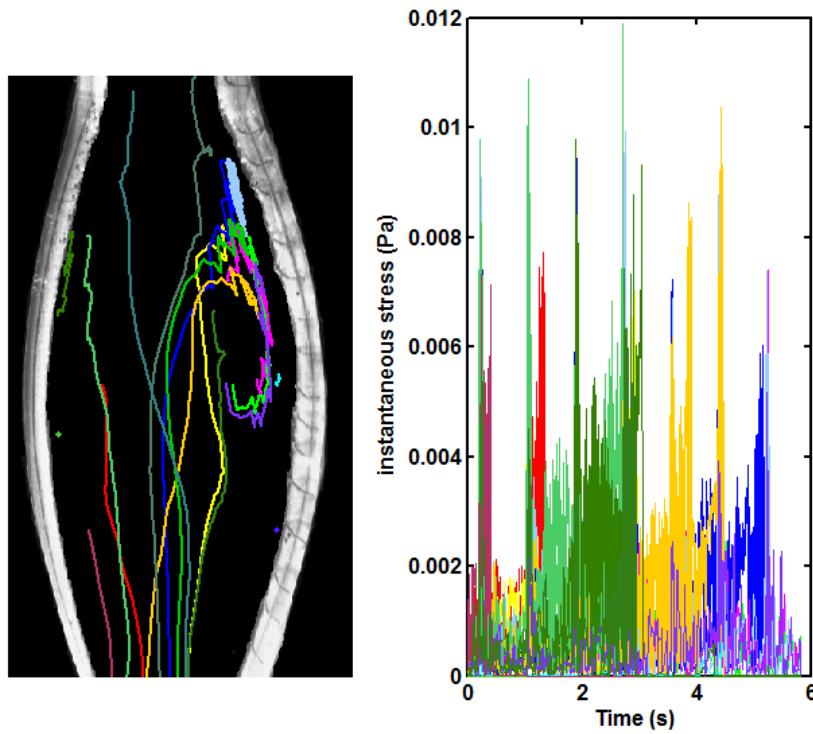
Figure 4.23: Trajectories and viscous shear stress history of some particles in anterior plane for the NC

71
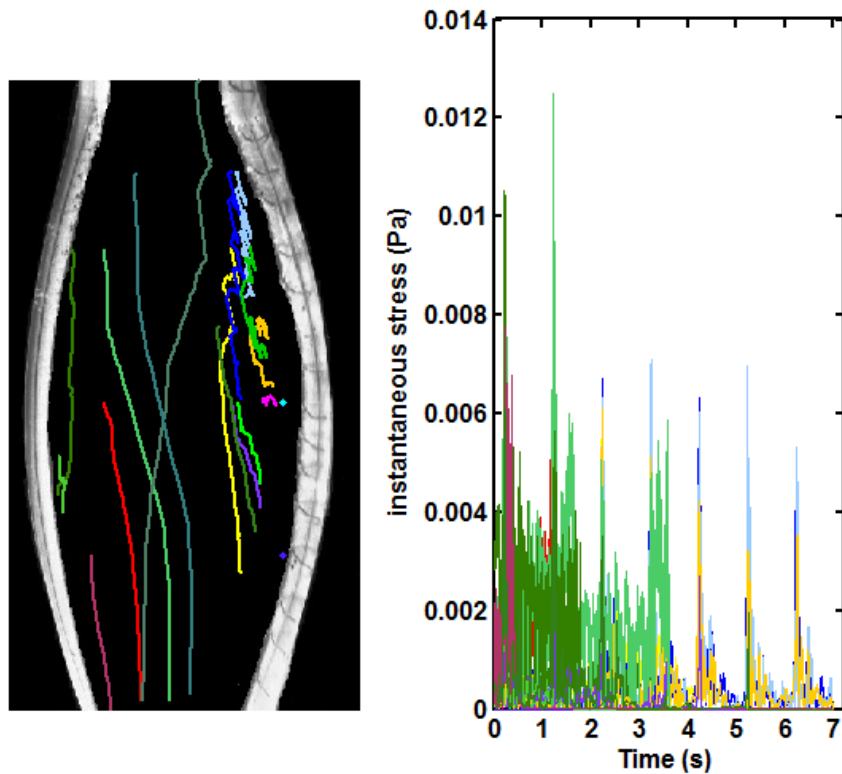
Figure 4.24: Trajectories and viscous shear stress history of some particles in anterior plane for the LC

4.6 Discussion

The purpose of this chapter was to investigate the differences in flow structures inside AAAs between NC and LC. All previous studies neglected the effect of the LC while it might be the main cause of aortic degradation as people spend 1/3 of their life under such conditions (sleeping). Note that the LC can also occur in patients suffering from spinal cord injury (Gordon et al. 1996). This disease is strongly correlated with AAA presence (Gordon et al. 1996, Nakahashi et al. 2002). The NC is usually associated with higher flow rates and more disturbed flow structures. However, this disturbance might be helpful for blood mixing. Arzani and Shadden (2012) stated that increasing flow rate results in better blood flow mixing.

One of the most critical regions in both flow cases (normal and low) is at the proximal neck (where flow experiences a sudden diametral expansion). In the LC, particles tended to stay longer and are expected to be subjected to higher cummulative shear stress effects. The systolic period in both cases is strong enough to move all the particles downstream. However, in the LC, the backflow in the anterior side of the AAA occurring during diastole redirects the particles towards the inflow region leading to a higher residence time compared to the particles in the flow stream or close to the posterior wall. These results show that the lateral plane can be divided into two distinct regions separated by the shear layer induced by the inflow jet. This shear layer acts as a "go-no go" barrier. As long as the particle has the ability to pass from the left to right side of the shear layer, it has the tendency to leave the AAA region. This shear layer changes during the cardiac cycle, and it vanishes during systole. If the shear layer moves closer to the bulges, more particles can be released from the AAA region. Some studies have shown that blood stasis (Xue et al. 2013), and low wall shear stress values (Amiral et al. 1997) lead to endothelial cell inflammation. This in turn promotes the production of platelets by the body and their aggregation. The topology of the flow shows that the LC is associated with very low velocities near the anterior side of the lateral plane. If a platelet is activated in the proximal neck and moved to the anterior side, its probability to adhere to the AAA wall is higher.

Some sleeping disorders are associated with cell inflammation. As one of the causes of cell inflammation is reduced Oxygen delivery to cells (Vorp et al. 2001). Obstructive sleep apnea reduces the oxygen concentration in blood (Sahara et al. 2012). Moore et al. (2011) tested 127 AAA patients. They found that more than 40% of AAA patients were also suffering from sleep apnea. Moreover, the annual expansion rate of their AAA was higher.

The stasis of the blood within the bulge of the AAA and the presence of very low shear stresses was found to promote thrombosis (Bluestein et al. 1996). The shear stress near the walls is one of the most common criteria for judging the effect of flow in the AAA (Salsac et al. 2006). The lack of resolution near the wall from PIV data hinders this detection.

In conclusion, this chapter highlights the importance of the LC especially during sleep and demonstrates the need to find a method which can promote accelerating blood flow during long term LC since many seniors have difficulties in performing exercise or have a sedentary lifestyle.

5. COHERENT STRUCTURES AND FLOW DECOMPOSITION

5.1 Introduction

In this chapter, we will investigate the flow structures in an AAA with more emphasis on flow topology. For this purpose, the experimental velocity field will be analyzed in terms of large and small flow structures using Proper Orthogonal Decomposition (POD) and Dynamic Mode Decomposition (DMD). The purpose here is to comprehend the hidden dynamics of blood flow in an AAA and to highlight the regions of high vortex dynamics, their energy (using POD) and their frequency and stability (using DMD). Beyond the important fundamental aspect of defining the dominant flow structures associated with the flow in an AAA, a modal decomposition of the flow field might capture the most critical flow structures leading to thrombus formation or transition to turbulence, and ultimately to AAA rupture.

5.2 Proper Orthogonal Decomposition

Proper Orthogonal Decomposition (POD) is a method used to approximate a function defined in time and space by decomposing this function into spatial and temporal parameters as described by the following equation:

$$z(x,t) \approx \sum_{k=1}^{m} a_k(t)\phi_k(x) \tag{5.1}$$

This summation becomes exact when *m* reaches infinity. If a function is bounded by time intervals, $\phi_k(x)$ can be selected as a Fourier series or a Legendre polynomial or any function that is suitable

for constructing the basis of the original function. The variables x and t represent the spatial and temporal coordinates.

In the application of fluid flow, POD reconstructs the unsteady velocity field into a number of modes. The generated modes are ranked by their importance (based on kinetic energy content). The extraction of these modes is performed by mapping the data into new basis functions extracted from the original data set and forcing them to be linear and orthogonal. The first few modes of the new constructed sets of data can be a general representation of the whole data set (Sirovich 1987). However, the main advantage of POD is that it decomposes the flow into spatial dynamics (modes) and temporal dynamics (coefficients) as shown in the following equation:

$$u(x, t_j) = \sum_{i=1}^{N} \alpha_i (t_j)\phi_i(x), \; j = 1, \ldots, N \tag{5.2}$$

where N is the number of snapshots representing the temporal coefficient which represents the number of modes. α can be represented by a temporal coefficient (amplitude) and ϕ is the basis function. POD was first introduced by Lumley (1967). It can be executed by either the classical method or the snapshot method. In the context of this thesis, the snapshot method was used since it is more computationally efficient. The main steps of the snapshot method will be outlined (but for further information, the reader is recommended to see Holmes (2012).

Performing POD on a vector field can be executed either with or without the subtraction of the average flow field. If the latter is performed, then the generated modes are related to the fluctuation part of the velocity. Each of the time steps in the PIV measurements considered to be a snapshot,

and the velocity vectors are arranged in a matrix as shown by Equation 5.3. In this thesis, the average flow field has not been subtracted from the snapshot velocities:

$$A = [u^1 u^2 \ldots \ldots \ldots u^N] = \begin{bmatrix} u_1^1 & u_1^2 & \ldots & u_1^N \\ \vdots & \vdots & \vdots & \vdots \\ u_m^1 & u_m^2 & \vdots & u_m^N \\ v_1^1 & v_1^2 & \vdots & v_1^N \\ \vdots & \vdots & \vdots & \vdots \\ v_m^1 & v_m^2 & \ldots & v_m^N \end{bmatrix} \tag{5.3}$$

Then, the covariance matrix is calculated by the following equation: $C = A^T A$. The third step is to apply a singular value decomposition (SVD) on the generated data:

$$SVD(C) = U\Sigma V^T \tag{5.4}$$

SVD decomposes the original matrix into three matrices: U and V are orthonormal matrices and Σ is a diagonal matrix. This decomposition provides general information about the original matrix C. The rows of U contains the eigenvectors of C. Σ is a diagonal matrix which ranks the eigenvalues by their magnitude. POD modes will then be evaluated by multiplying the matrix A with the eigenvector matrix U:

$$\phi_i = \frac{AU^i}{\|AU^i\|}, \quad i = 1, \ldots, N \tag{5.5}$$

Then the POD coefficients can be estimated by projecting the velocity field on the POD spatial modes:

$$a_i^n = \phi_i A \qquad\qquad (5.6)$$

Since POD modes are ranked by their energy, the first mode contains the most energetic structures in the flow. More specifically, more than 90% of the kinetic energy in the flow can be extracted from the first few modes. Therefore, the reconstruction of the flow with these modes reveals the main energetic coherent structures in the fluid flow. While PIV provides the general overview of the flow behavior of the model, POD gives a more compact representation of the structures of this flow.

Since POD provides the spatial and temporal modes, it is important to test the ability of these two functions to reconstruct the original flow field. For the NC, the PIV results contain 100 snapshots for one cycle, and the first mode represents 82.68% of the total energy while the second mode represents 14.84% of the total energy. A reconstruction of the original flow field is performed by using these two modes. Figure 5.1 (a) shows the original snapshot taken at the peak of systole for the NC. Figure 5.1 (b) shows the reconstructed data field using the first mode only. Figure 5.1 (c) shows the reconstructed snapshot after adding the second mode. Figure 5.1 (d) shows the reconstructed snapshot after the first 10 modes. Figure 5.2 illustrates the error between the original mode and the reconstructed snapshot.
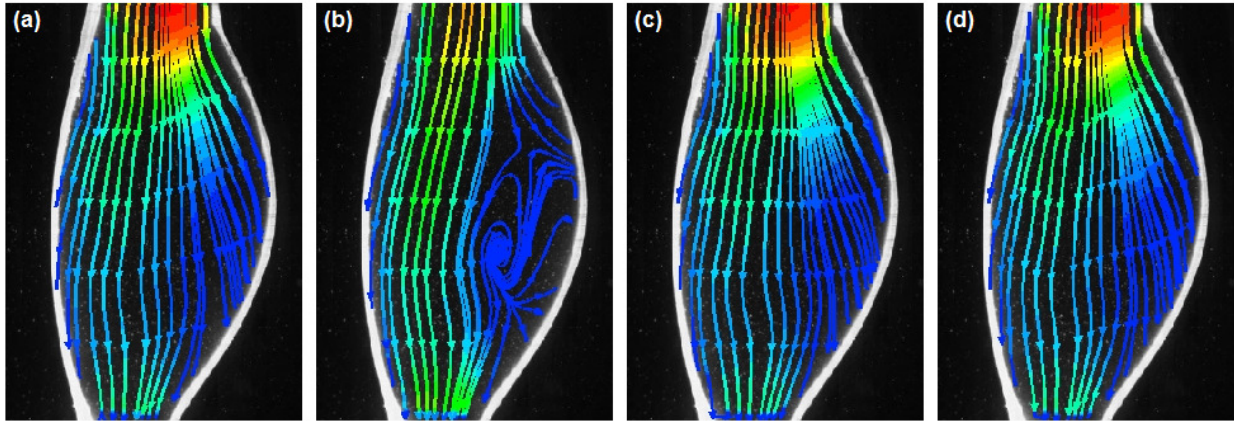
Figure 5.1: Reconstructed data field based on POD modes at the peak systole of the NC: a) Original snapshot, b) Only the first mode used, c) first and second modes are used, d) The first 10 modes are used
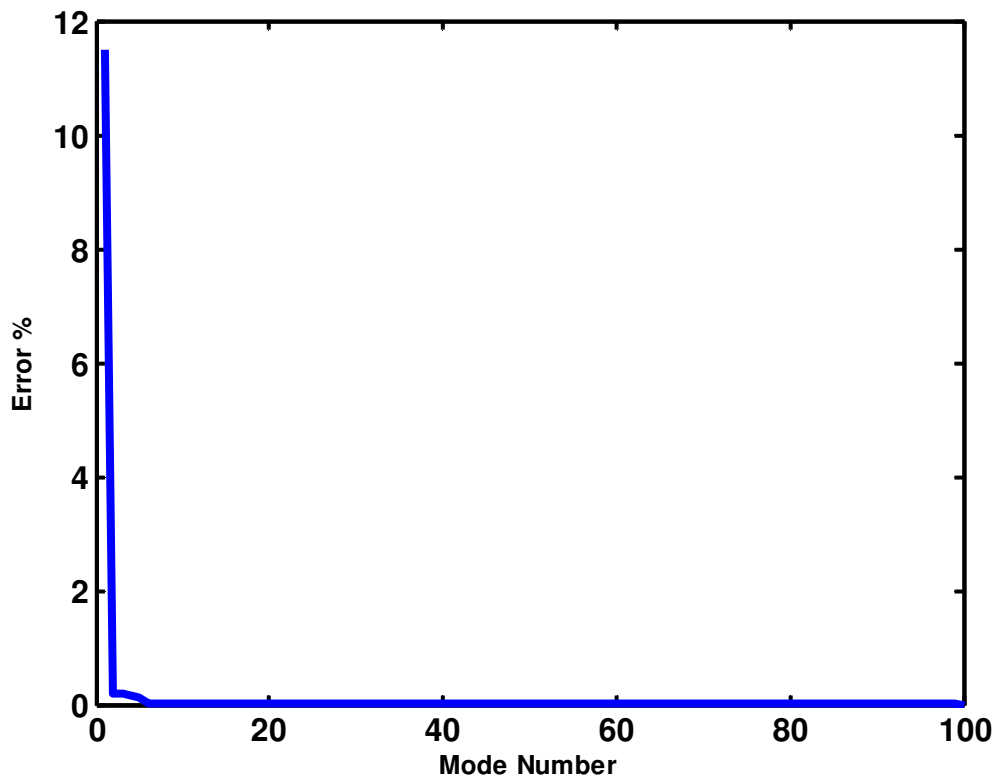
Figure 5.2: Error in the reconstruction of the snapshot in Figure 5.1 as a function of the number of modes used

The number of snapshots plays a major role in POD. To perform this analysis, 100 snapshots per cycle (0.833s), which gives a frequency of 120 Hz, were used. Kefayati and Poepping (2013)

indicated that the minimum temporal frequency required for POD application in the carotid artery is 100 Hz with around 92 snapshots, and the error associated with a decreasing number of snapshots from 462 to 92 is less than 1%.

We analyzed the effect of reducing the number of snapshots from 100 to 50 on the POD modes. Figure 5.3 shows that the error in the first (most energetic) modes is limited when the number of snapshots is reduced (from 100 to 50 snapshots). However, the least energetic modes, representing turbulence or simplimg noise, are significantly affected by the reduction in the number of snapshots. Such modes are not of interest in this thesis where only the most energetic modes, the first four modes, are investigated and discussed. The error was based on subtracting the resulting modes and the difference was divided by the original mode.
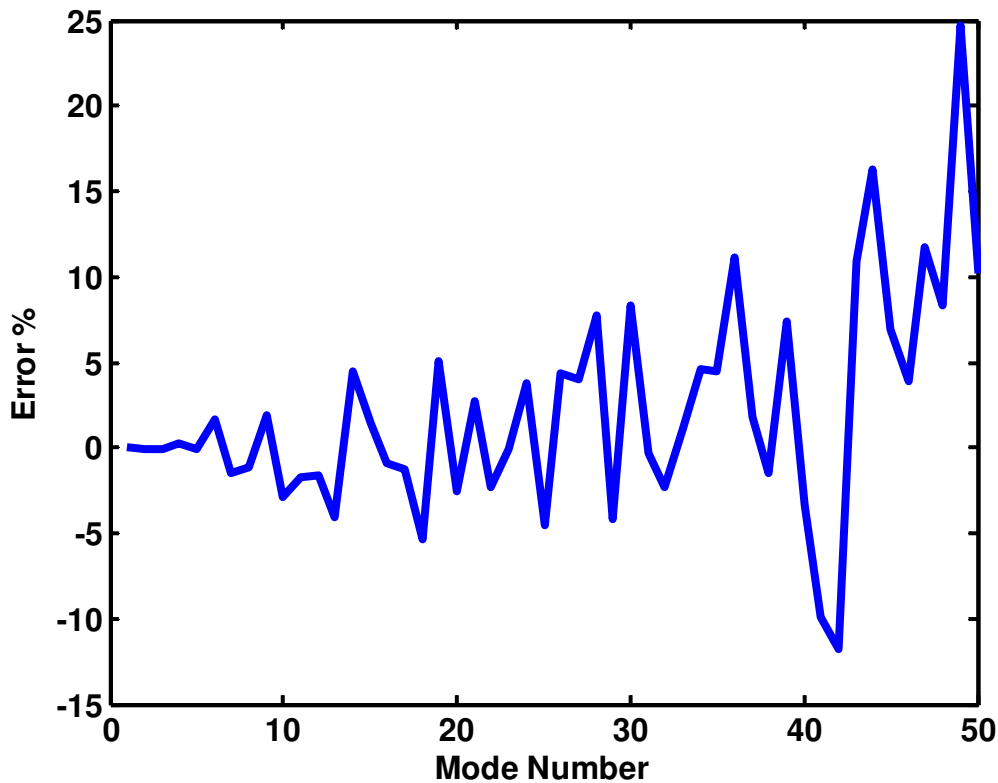
Figure 5.3: Error in POD modes if 100 or 50 snapshots used in the decomposition

Another important analysis is to see the variation of POD if one cycle or multiple cycles were used in the analysis. Also, the variations between cycle to cycle should be investigated to point out if this variation affects the mode energetic content, spatial modes, or temporal modes. Table 5.1 shows the energetic content by using two random cycles and by taking seven cycles in the analysis. The highest variation can be seen from mode 3 Figure 5.4 shows mode 3 after applying POD on these three cases. The spatial modes hold almost similar structures as illustrated. Temporal modes are also the same. However, for seven cycles they repeat themselves based on the number of cycles used.

Table 5.1: Variation of energetic mode content when using POD for one cycle and multiple cycles

	Cycle 2	Cycle 5	Seven cycles
Mode 1	82.68%	82.79%	81.56%
Mode 2	14.84%	14.43%	14.53%
Mode 3	1.17%	1.4%	1.37%
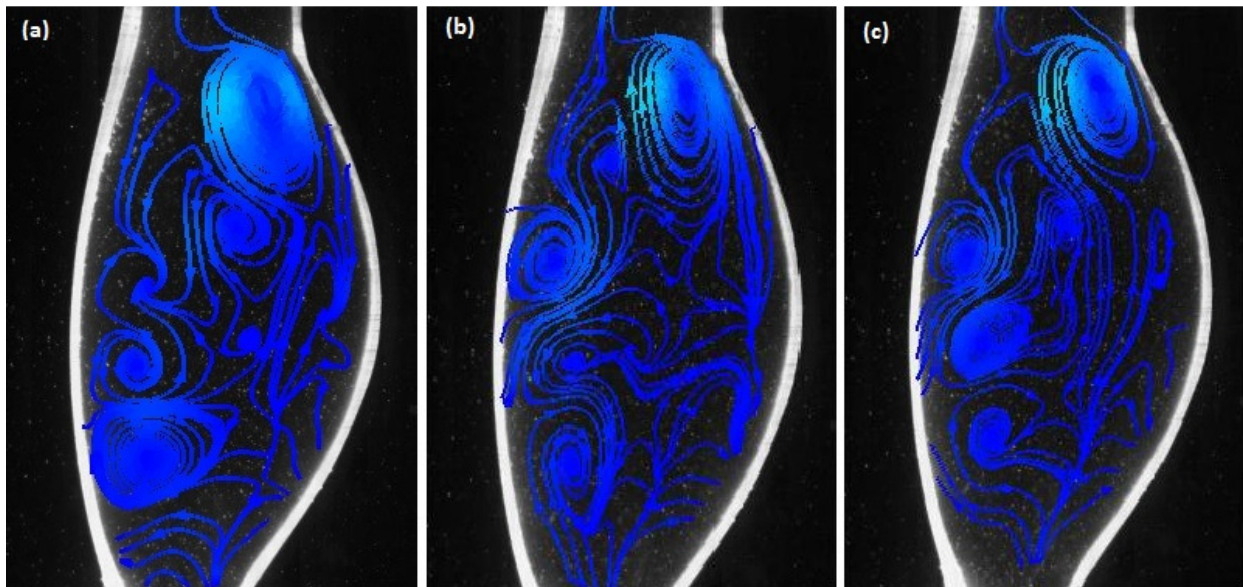
Figure 5.4: Streamlines of POD modes when using: (a) the second cycle, (b) the fifth cycle (c) seven cycles

5.3 Proper Orthogonal Decomposition Results

Lateral plane: POD modes are classified by spatial and temporal modes. Figure 5.4 illustrates a logarithmic plot of the fractional energy that each mode holds. For the NC, the first mode accounts for around 82.68% of the total energy of the fluid flow, while the second mode accounts for 14.84%. The third mode has approximately 1.17% of the total energy and all the other modes (4 to 100) represent less than 4%. For the LC, the first mode accounts for approximately 80.83% of the total energy of the fluid flow, while the second mode accounts for 16.6%. The third mode has around 1.6% of the total energy and all the other modes represent less than 2%. This shows that there is no significant difference in terms of the contribution of each mode to the total kinetic energy and that both conditions can be "compressed" in terms of energy into four fundamental modes.
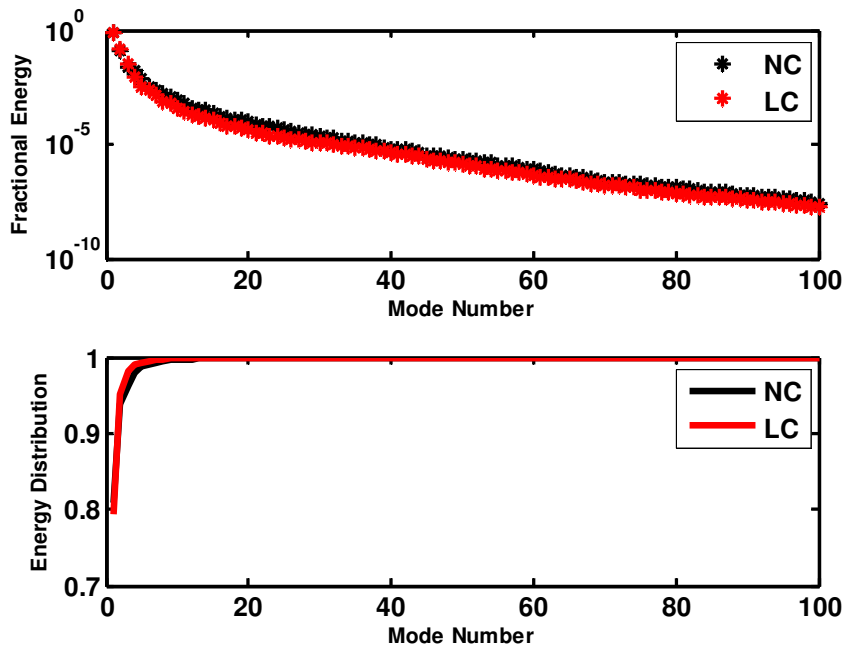
Figure 5.5: Top: logarithmic plot of the fractional energy for the NC and for the LC as obtained using POD of the velocity in the lateral plane. Bottom: cumulative energy distribution as a function of mode number

Figure 5.6 shows the first four modes presented in terms of streamlines, vorticity, and swirling strength in the second, third and fourth rows respectivly while the first row represents the temporal modes. The first temporal mode shows a waveform similar to the imposed inflow rate generated by the NC. This is expected since the first mode can be a representation of an average flow field behavior. A similar trend was found in Figure 5.7. The second temporal mode shows a similar trend as the first mode but with an opposite sign and lower amplitude. The same pattern can be visualized in the LC (Figure 5.6). As the mode number increases, the shape of the temporal modes tend to have more irregular patterns. Higher temporal modes for both the NC and the LC show a more irregular distribution.

The first spatial mode for the NC Figure 5.5 a1, b1, c1 represents the average flow field characterized by a jet entering the AAA. The jet does not occupy the whole AAA compared to the inflow jet occurring during the peak of systole as shown in (Figure 4.4 a3, b3, c3). This mode shows that the anterior part of the AAA is characterized by a vortex closer to the anterior bulge. The second mode in Figure 5.6 a2, b2, c2 has two major flow structures represented by a small vortex near the posterior entrance, and a large vortex in the middle of the region. The third mode which apears in Figure 5.6 a3, b3, c3 is characterized by a large vortex in the proximal neck with some small vortices occupying the AAA region while the fourth mode posseses a complex structure as presented in Figure 5.6 a4, b4, c4.

When comparing to the first mode of the LC (Figure 5.7 a1, b1, c1), the low velocity region near the anterior bulge has a larger size. The second mode (Figure 5.6 a1, b2, c2) shows the major

83

contribution of the reversed flow and the behavior of the large vortex structures occurring during diastole. These two modes have almost the same structure as for the NC.

The disturbances in the flow structures between the NC and the LC become more important when considering the third and fourth modes. They present small energetic disturbance structures in the AAA region including counter-rotating vortices present near the posterior side of the AAA. These types of structures are absent is the third mode of the LC. When compared to the LC, most of the lateral plane is described by a backflow. Vortical structures are more advantageous due to the fact that they promote mixing.

Figure 5.6: First four POD modes presented in terms of reconstruction coefficients first raw shows the temporal modes, and (a) velocity streamlines (b) vorticity (c) swirling strength lateral plane for the NC
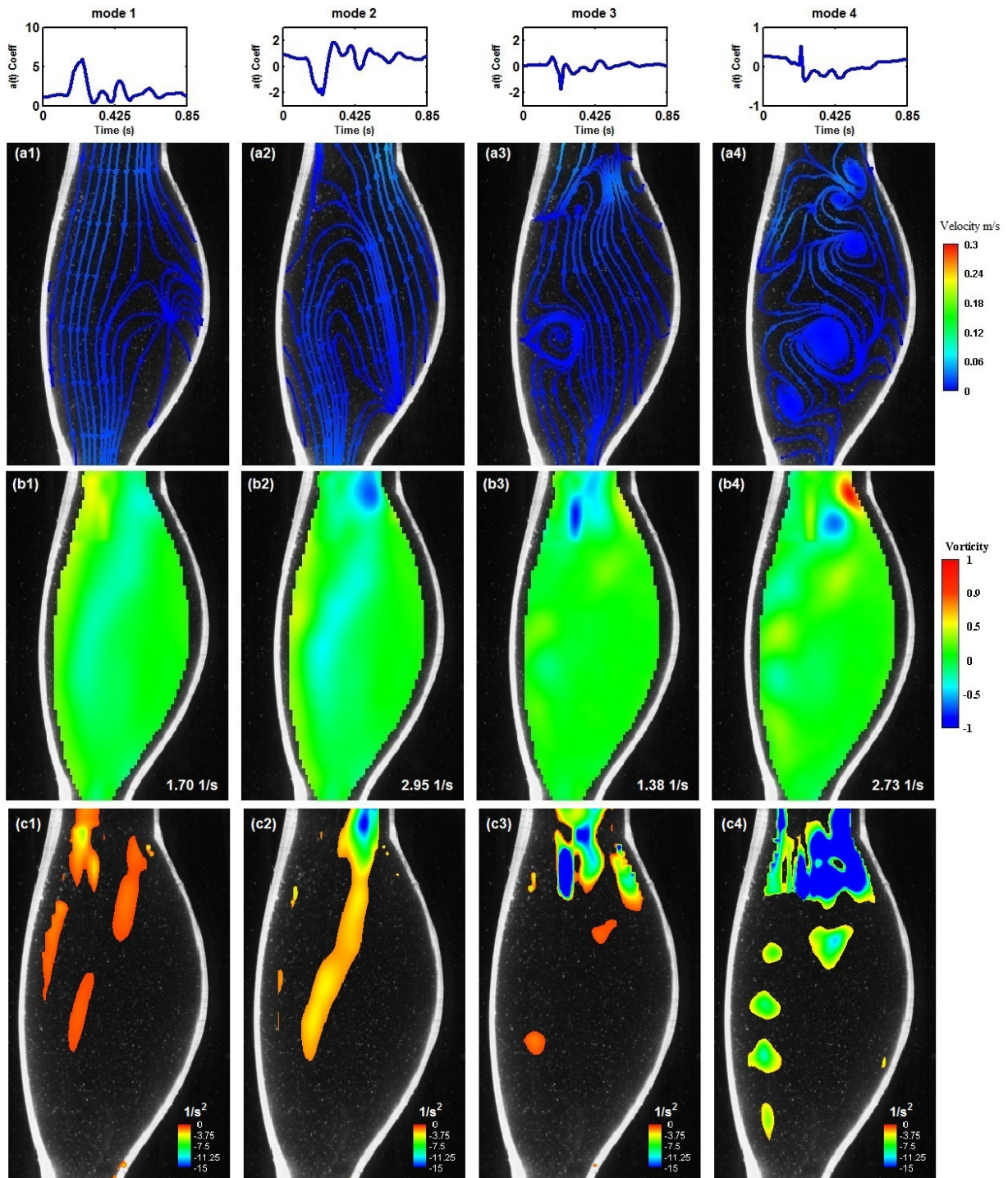
Figure 5.7: First four POD modes presented in terms of reconstruction coefficients first raw shows the temporal modes, and (a) velocity streamlines (b) vorticity (c) swirling strength lateral plane for the LC

86

Anterior plane: Figure 5.8 shows the same information as Figure 5.6. Temporal modes for the NC have almost a similar trend as for the lateral plane. The first temporal mode shows a flow directed towards the exit of the AAA domain representing 85.71% of the total energy with a small vortex structure on the side of the AAA due to the asymmetry of the inflow jet. The second mode (Figure 5.8) shows a vortex at the center of the AAA inclined towards the right bulge. This second mode represents 12.47% of the total energy. While other modes have very small energy content, their topology shows interesting flow phenomena. They are generally described by complex vortical structures occupying the AAA region.

When comparing the NC to the LC (Figure 5.9), the first mode has almost the same features except for the small vortex located in the left bulge which is not present for the LC. This mode holds approximately 88.3% of the total energy. The second mode also has similar features as in the NC holding 8.35% of the total energy. The third mode has low energetic content with less complex vortical structures for the LC compared to the NC.
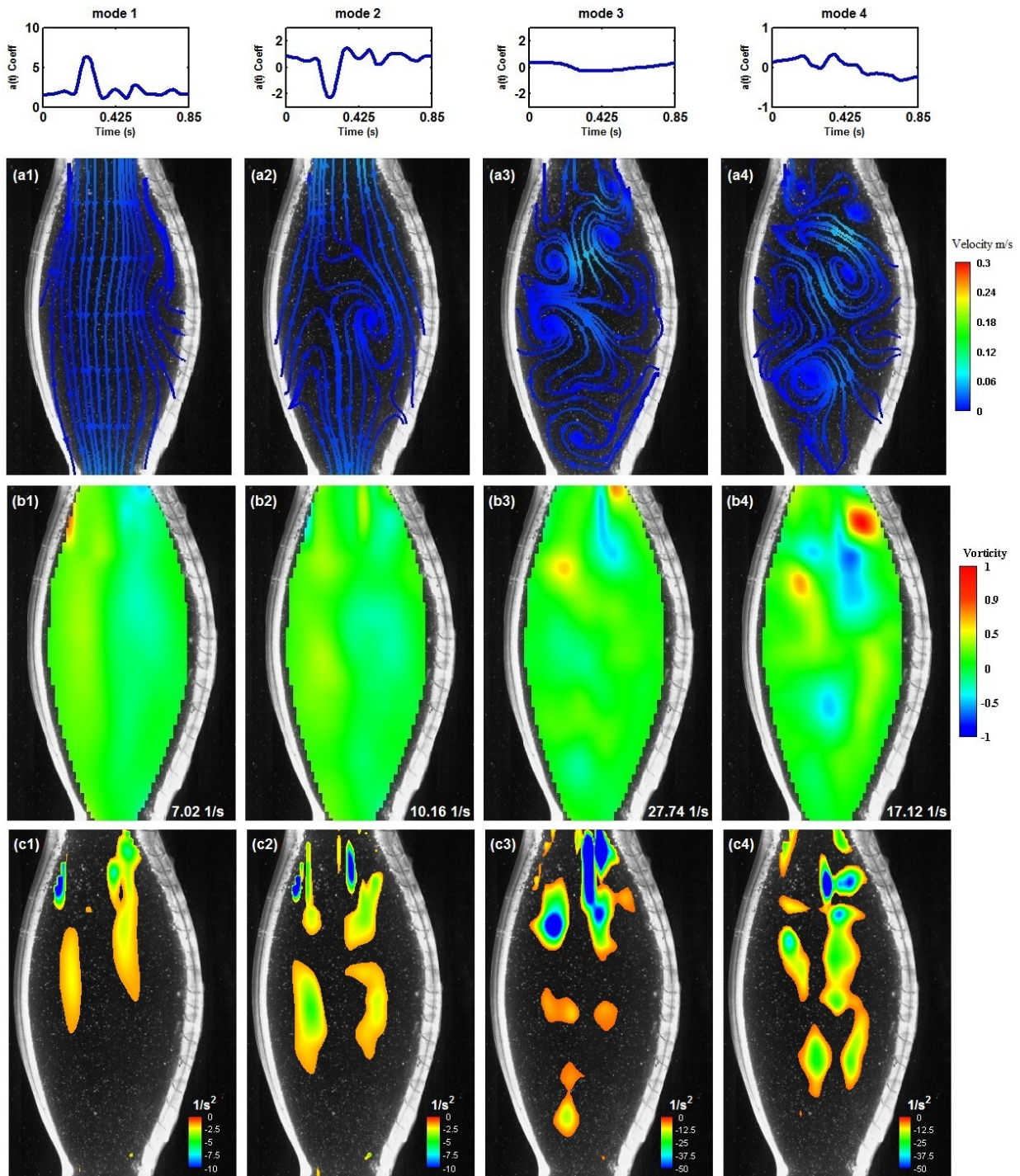
Figure 5.8: First four POD modes presented in terms of reconstruction coefficients first raw shows the temporal modes, and (a) velocity streamlines (b) vorticity (c) swirling strength anterior plane for the NC
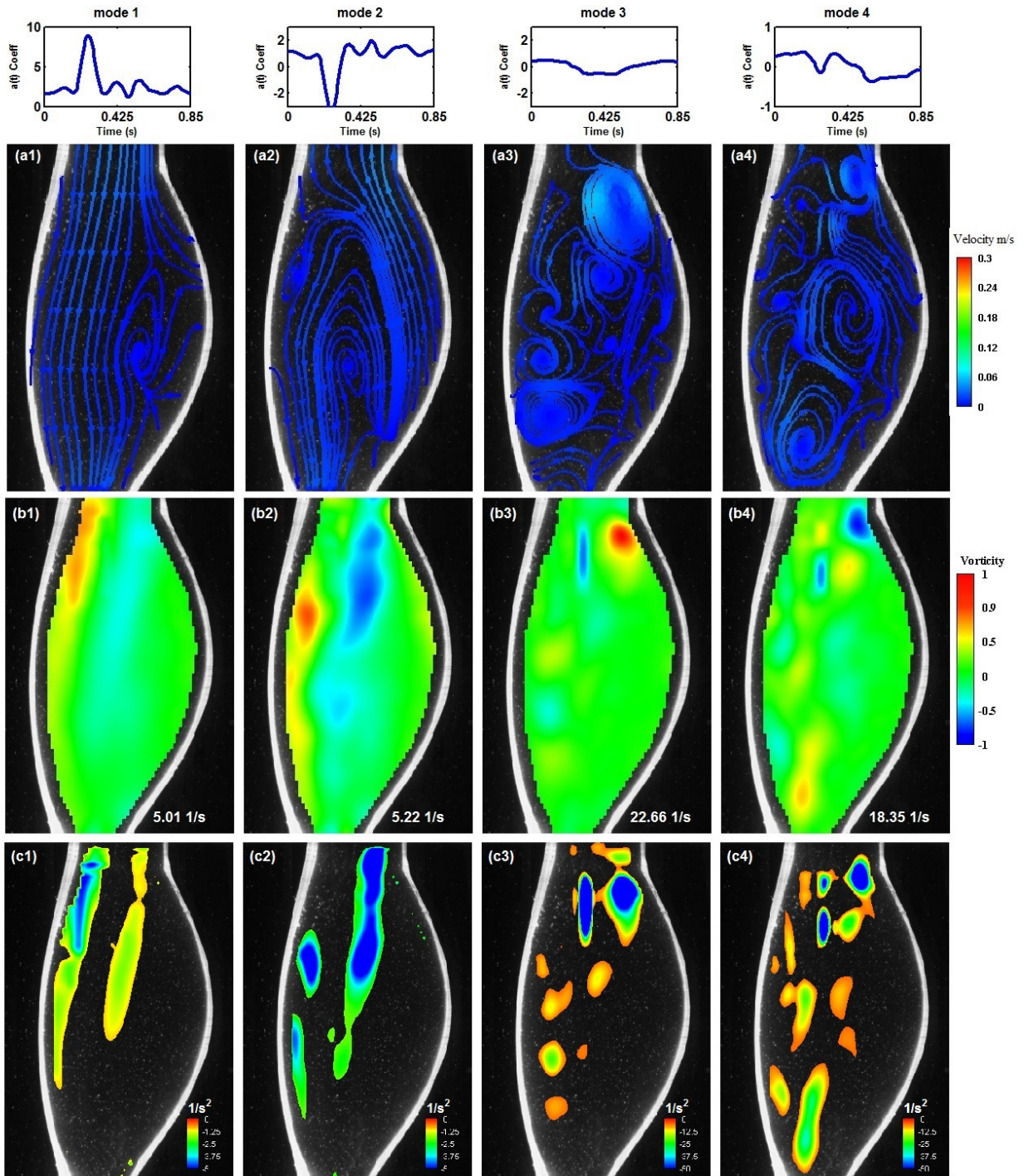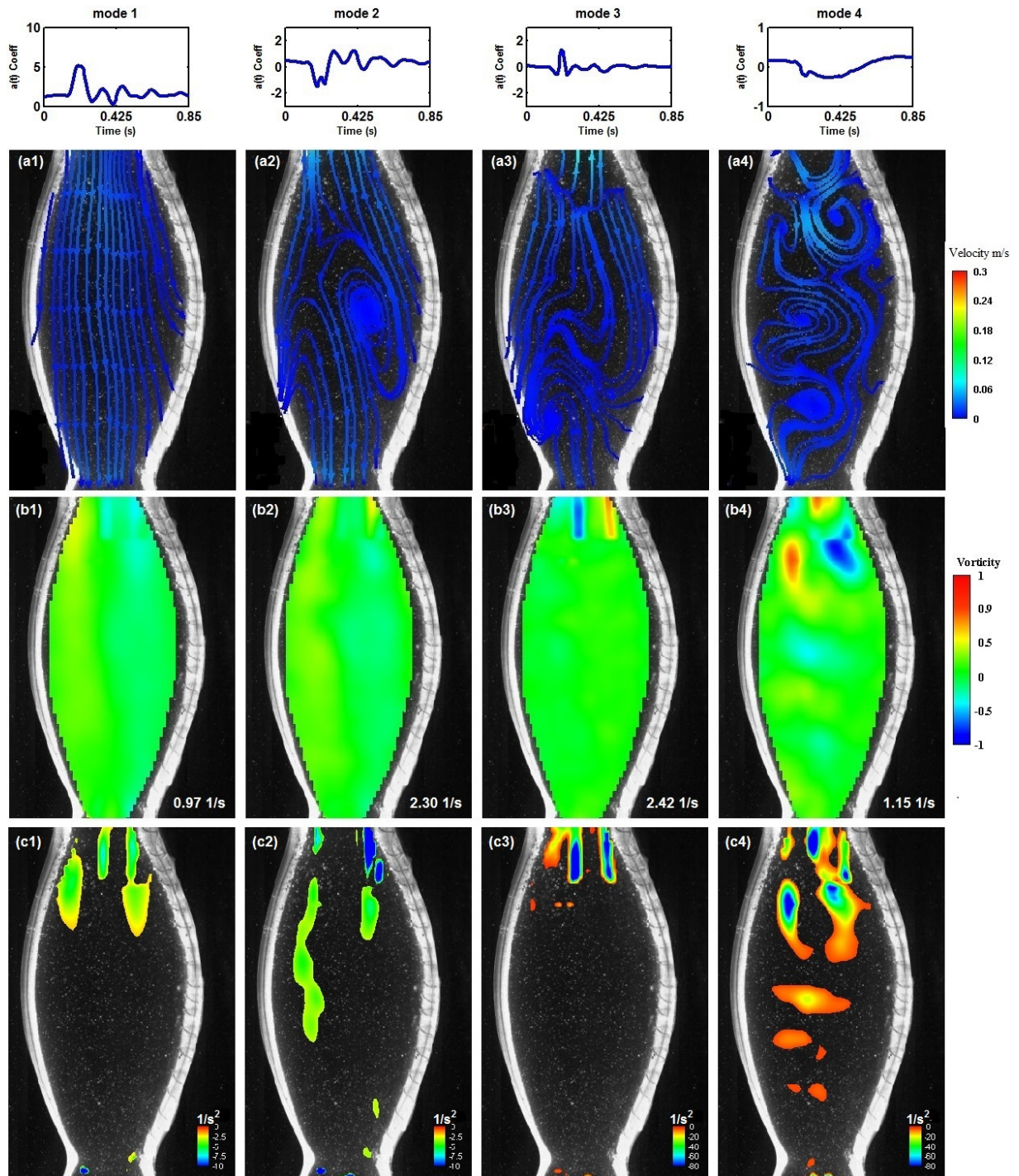
Figure 5.9: First four POD modes presented in terms of reconstruction coefficients first raw shows the temporal modes, and (a) velocity streamlines (b) vorticity (c) swirling strength anterior plane for the NC

5.4 Dynamic Mode Decomposition

DMD is a data reduction method used to note the dynamical behavior of a system. DMD decomposes the flow field into a set of modes that represent the main characteristic frequencies of the flow (Schmid 2010). DMD identifies not only the main dynamical coherent structures in the flow field but also their temporal evolution (Santosh et al. 2012). The main concept behind DMD is to identify a linear mapping from snapshots that better represent the non-linear flow process (Tu et al. 2013). Consider the time resolved velocity data set recorded in the AAA model at a time interval of Δt, the complete data set can be expressed as (Rowley et al. 2009, Schmid 2010):

$$D_1 = \{v_1, v_2, \dots \dots \dots, v_{N-1}\} \tag{5.7}$$

$$D_2 = \{v_2, v_3, \dots \dots \dots, v_N\} \tag{5.8}$$

Where, D represents the whole data set, the subscript N represents the total number of snapshots (100 in this study). D_1 and D_2 are the snapshots of the data set, separated by a constant interval Δt. We assume a linear mapping between the snapshots $v_{j+1} = A_{\Delta t} v_j$. Where $A_{\Delta t}$ is the linear mapping coefficient matrix of the data set. In general, the whole data set can be expressed under the form:

$$A_{\Delta t} D_1 = D_2 \tag{5.9}$$

By this definition, the flow is assumed to be linearly dependent although it stems from a non-linear process. The role of the matrix $A_{\Delta t}$ is to connect the velocity field recorded at instant t with $t + \Delta t$. When a large number of snapshots are used, the coefficient matrix $A_{\Delta t}$ reaches a certain limit.

At this limit, further snapshots can be expressed by the previous ones since adding more snapshots will not improve the coefficient matrix $A_{\Delta t}$. Mathematically $A_{\Delta t}$ can be expressed by an approximation matrix:

$$A_{\Delta t}D_1 = D_2 \approx D_1 S \tag{5.10}$$

The matrix S has the form of a companion matrix and can be expressed by a compact representation of the matrix $A_{\Delta t}$. The matrix S has the form:

$$S = \begin{Bmatrix} 0 & & & & a_1 \\ 1 & 0 & & & a_2 \\ & 1 & \ddots & & \vdots \\ & & \ddots & \ddots & a_{N-2} \\ & & & & a_{N-1} \end{Bmatrix} \tag{5.11}$$

Schmid (2010) proposed a linear approximation method using singular value decomposition of D_1 and substituting the results into Equation 5.10. Then, by rearranging the results, the matrix S can be estimated by:

$$S \approx U^H A U = U^H D_2 V \Sigma^{-1} \tag{5.12}$$

The eigenvalues of S approximate the eigenvalues of $A_{\Delta t}$. The eigenvectors provide the coefficients of the combination that are important to express the modal structure. Therefore, the DMD modes can be expressed as:

$$\Phi_i = U\Lambda_i \; with \; [\Lambda_i , \lambda_i] = eiv(S) \tag{5.13}$$

Where Λ_i are the eigenvectors of the matrix S. The eigenvalues of S (λ) describe the growth/decay and oscillatory characteristics of each dynamic mode (Schmid 2010, Proctor and Eckhoff 2015). The real part of each eigenvalue represents the exponential growth/decay of the corresponding mode, while the imaginary part represents the pure frequency of the mode. For this study, a Matlab code (MathWorks, Natick, MA, USA) was written in order to decompose the flow field in the AAA using DMD.

The resulting modes were normalized. Therefore, the amplitude of the modes has been computed by a projection of each mode onto the first snapshot. The norm of this projection presents the amplitude of each mode in the data structure (Muzio 2013).

There are significant differences in the outcome resulting from the decomposition of the flow field either using POD or DMD. In POD, the modes are orthogonal in space, while in DMD the modes are orthogonal in time. As a result, each POD mode contains a mixture of frequencies, while each DMD mode represents a pure frequency (Seena and Sung 2011). DMD allows then the investigation of periodic flow structures independently (Tu et al. 2013) Furthermore, POD extracts the coherent spatial structures and ranks them based on their kinetic energy content, while DMD aims at extracting the temporal coherent structures.

5.5 Dynamic Mode Decomposition Code Validation

In this section, the code that has been used for DMD will be validated using a fabricated pattern function. This function will be given an average field (q0) while other patterns that are time dependent will be added to the field. This fabricated pattern is presented by equations 5.14-5.16. The constant α is an indicator of the growth/decay rate of the mode. Similar to the study conducted by (Seena and Sung 2011), α_1 will be 1 so that the mode will not grow or decay, q2 will decay over time and q3 will grow over time. The values for α are estimated from table 5.2. Figure 5.10 shows these fabricated patterns. For this analysis, 16 points of x and 20 points of y have been chosen.

$$q = q_0 + q_1 + q_2 + q_3 \tag{5.14}$$

$$q_0(x, y, t) = \exp(-y^2/0.7) \tag{5.15}$$

$$q_n(x, y, t) = \alpha_n(t) \sum_{m=-\infty}^{m=\infty} (-1)^m \exp\left[-\left(\frac{x - \beta_n m - \gamma_n t}{d_n}\right)^2 - \frac{y^2}{d_n}\right] \tag{5.16}$$

$$n = 1,2,3$$

Table 5.2: Constants for the fabricated pattern

n	α_n	b_n	γ_n	$\alpha_n(t)$
1	0.03	0.8	0.377	1
2	0.01	0.4	0.252	$e^{-t/80} - 0.1$
3	0.005	0.3	0.126	$1 - e^{-\frac{t}{15}} + 0.2$
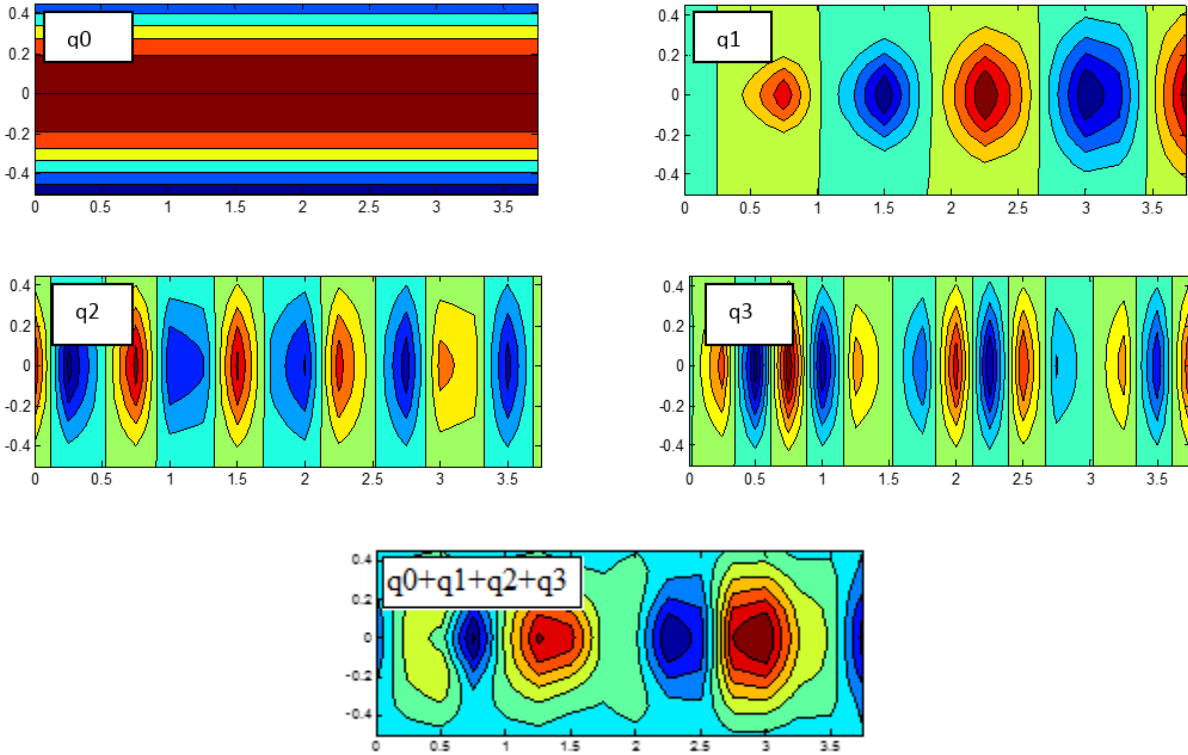
Figure 5.10: The Fabricated pattern function

After building this fabricated pattern, the second step is to perform DMD on this function. The resulting DMD modes are shown in Figure 5.11, and the mode spectrum is shown in Figure 5.12. The zeroth mode (average mode) is similar to q0. When looking to the DMD spectrum Figure 5.12, the pink point is an indicator of the zeroth mode behavior. This mode is neither growing nor decaying. The first mode, which is similar to q1, falls on the stability line and is therefore neither growing nor decaying (it is represented by the red points). The second mode (q2) decays over time. Hence, the real part of the eigenvalues is negative. The third mode (q3) is growing over time. Therefore, the real part of the eigenvalues has a positive value. The difference between the original constructed function and the resulting DMD modes are due to the linear approximation associated with applying DMD.

DMD is also capable of estimating the frequency of the modes. This frequency is found from the

imaginary part of the mode spectrum. All modes have a frequency of less than 2. However, they do not have the same magnitude. Regular snapshots do not reveal the clear frequency of the patterns. Therefore, a single point in each mode has been taken and plotted vs time as seen in Figure 5.13. q2 has the highest frequency as DMD results show, this is comparable to Figure 5.12, and the same procedure can be applied for other modes. To find if DMD is computing the right frequency. The frequency of each mode was estimated by finding the duration between the peak-to-peak in each mode. Values of the imaginary part have to be divided by 2π in order to find the real frequency. Table 5.3 shows the frequency of each mode vs the ones estimated from DMD. The values are similar and the difference can be considered negligible.
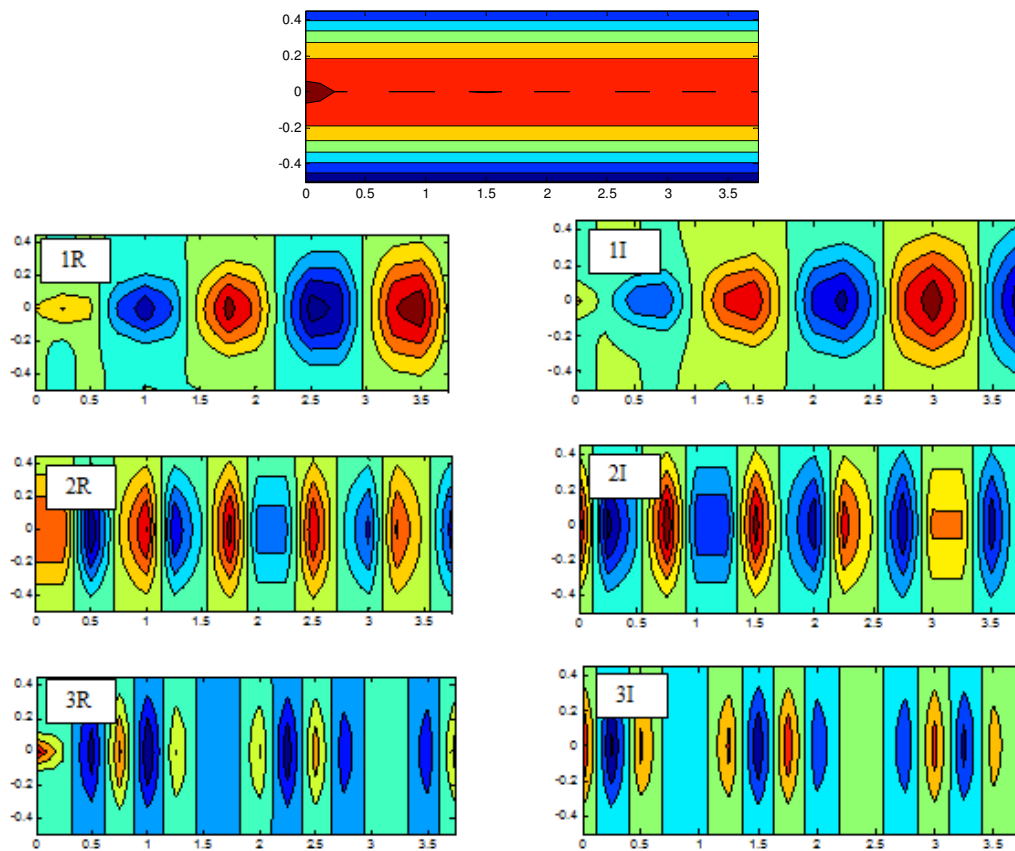
Figure 5.11: modes of DMD for the fabricated patterns

95
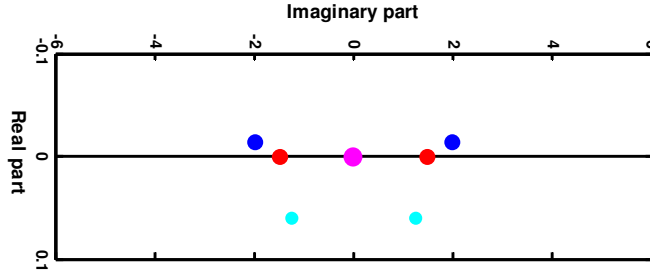
Figure 5.12: DMD mode spectrum
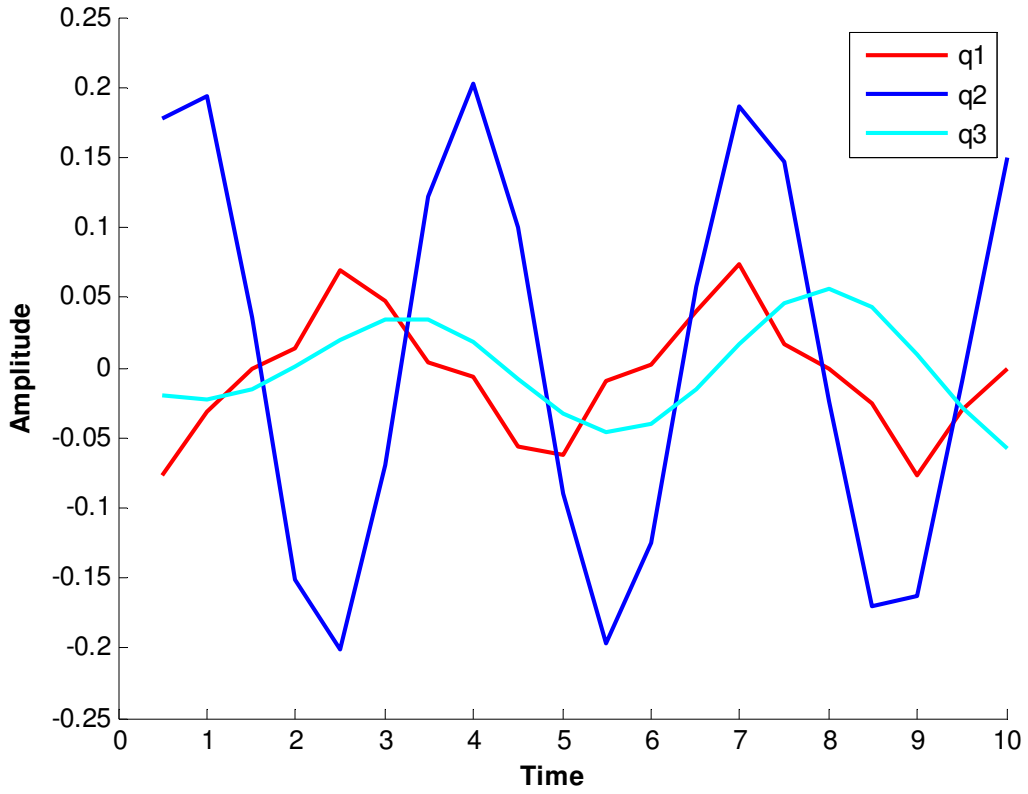
Figure 5.13: Time evolution of a single point taken from the three original patterns (q1,q2,q3)

Table 5.3: Estimated frequencies from fabricated pattern and DMD

	Frequency		Frequency
q1	0.222	mode 1	0.235
q2	0.333	mode 2	0.315
q3	0.2	mode 3	0.198

5.6 Dynamic Mode Decomposition Results

Similar to POD, DMD has to be tested for mode convergence. The resulting error difference is presented in Figure 5.14. DMD can be performed on one cycle only. Performing it on multiple cycles leads to divergence of modes by having too many growing and decaying modes.
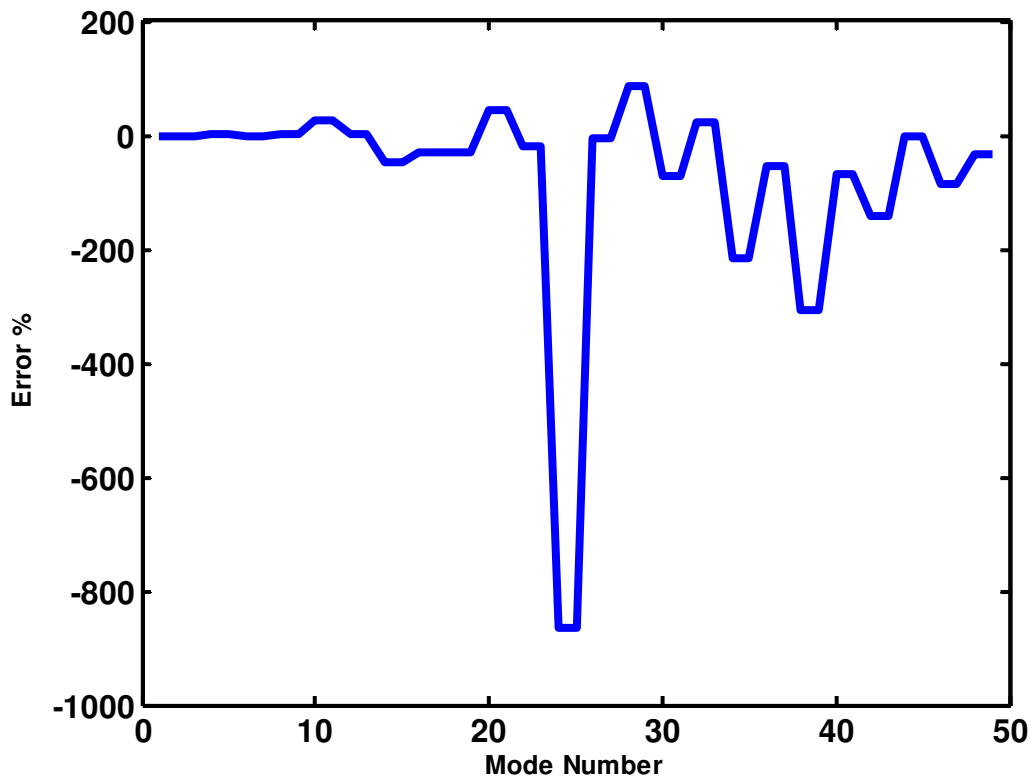
Figure 5.14: Percentage error difference of DMD modes between 50 and 100 snapshots

Lateral Plane: Figures 5.15 and 5.16 show the mode distribution of the DMD modes for both flow conditions (NC and LC) in the lateral plane. Most of the modes fall on the stability line, meaning that they are neither growing nor decaying. The zeroth (average) mode has been removed from the plot for the sake of display. The zeroth mode holds around 82.5% of the total kinetic energy with an amplitude of 5.86 for the NC and 75.6% with an amplitude of 3.5 for the LC. Since DMD

cannot capture processes with a frequency higher than the Nyquist frequency, those frequencies are not considered in the analysis (Schmid 2010). The mode distribution for the NC has a few unstable modes. However, they hold a very small amplitude. The mode spectrum shows that almost all modes are stable and fall within the stability line.

Figure 5.15: Mode spectrum (left) mode energy distribution (right) for the lateral plane in NC
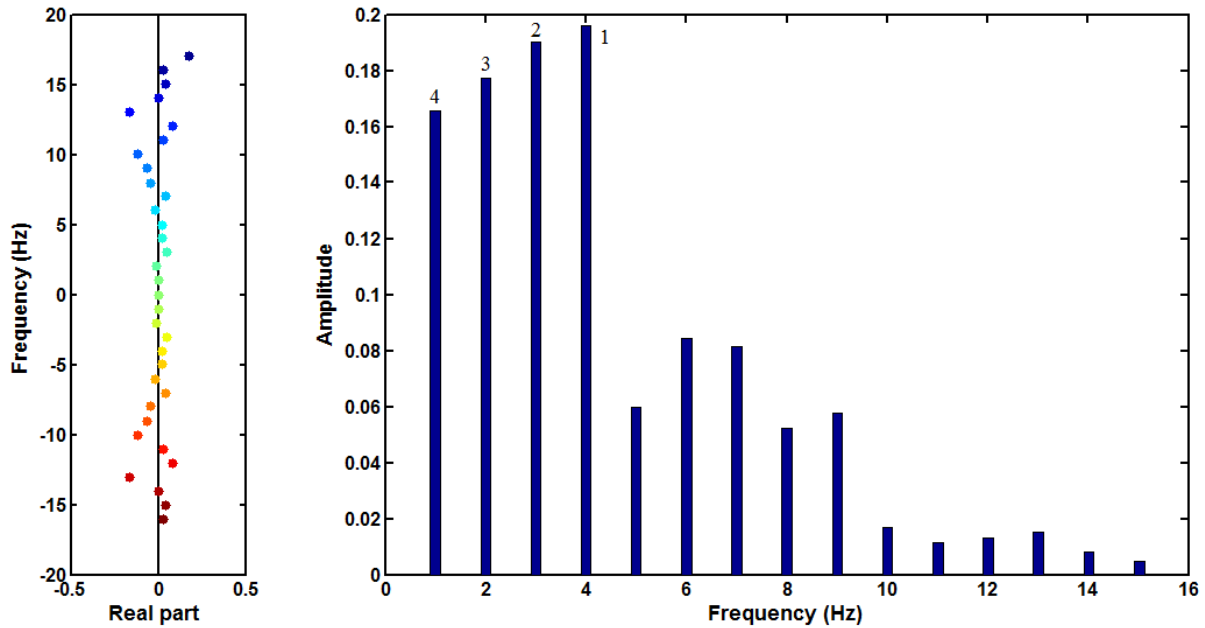
Figure 5.16: Mode spectrum (left) mode energy distribution (right) for the lateral plane in LC

DMD modes can be represented by real or imaginary parts (not shown) except for the average (zeroth) mode which is only composed of a real part. The average mode has similar characteristics as the first POD mode: a jet in the AAA directed towards the exit, the iliac arteries, with a recirculation zone in the AAA lumen.

DMD modes for both flow conditions were ranked based on their amplitude. The first mode (Figure 5.17 a1, b1, c1) for the NC shows a large vortex during the cycle with a frequency of 1.2 Hz, which reflects the frequency of the actual cardiac cycle. The second mode (Figure 5.17 a2, b2, c2) shows an interesting phenomena that cannot be captured using velocity snapshots: the presence of alternating vortices close to the posterior wall. They are an indication of the presence of a Kelvin-Helmholtz instability at a frequency of 2.4 Hz, which is twice the frequency of the cardiac cycle. The presence of this instability with high frequency means that this phenomenon occurs during both acceleration and deceleration. The third mode (Figure 5.17 a3, b3, c3) is an indication of a backflow behavior as a result of the negative flow rate occurring during the cardiac cycle. The

99

fourth mode (Figure 5.17 a4, b4, c4) shows the washing of the blood particles in the AAA lumen of the aneurysm at a frequency of 6 Hz. This frequency is close to the period corresponding to the systolic phase.

For the LC (Figure 5.18), the modes hold different energetic distributions. Both the first and the second modes for the LC display a backflow. This was not the case for the NC. The alternating vortex structures, associated with a Kelvin-Helmholtz instability, is weaker for the LC compared to the NC.
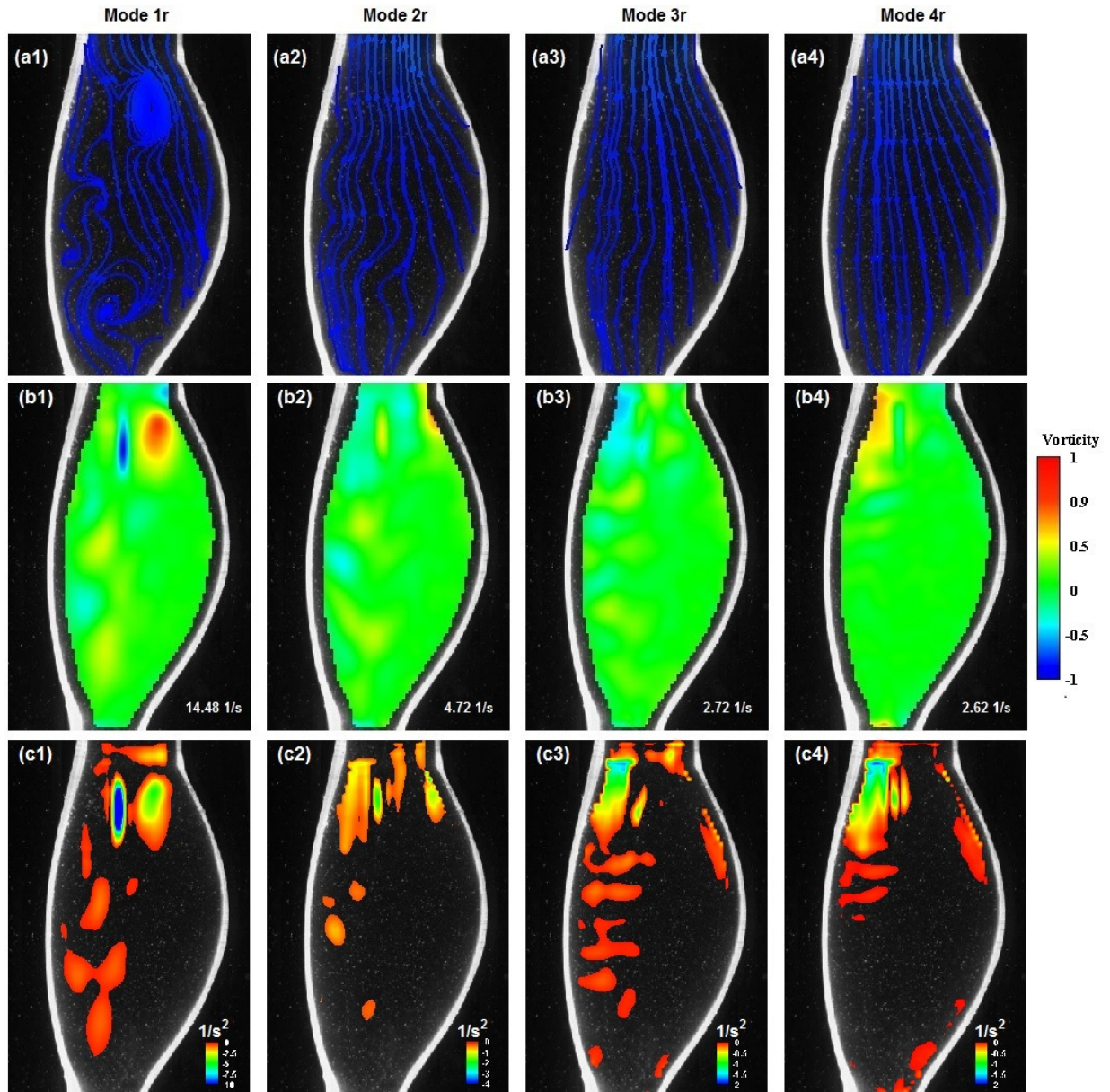
Figure 5.17: DMD real modes of for the lateral plane for the NC in terms of (a) velocity streamlines and (b) vorticity (c) swirling strength
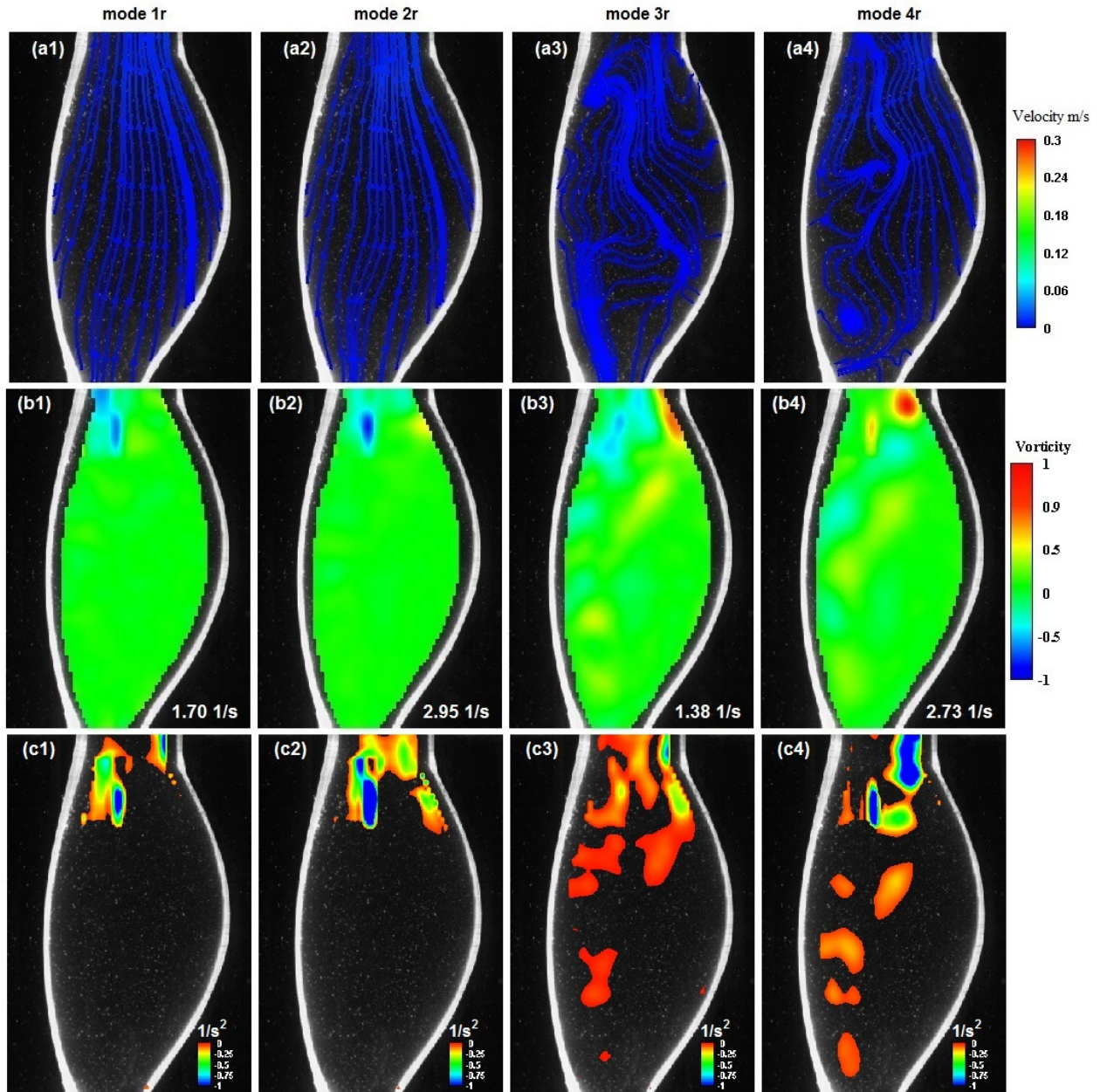
Figure 5.18: DMD real modes of for the lateral plane for the NC in terms of (a) velocity streamlines and (b) vorticity (c) swirling strength

Anterior Plane: Figures 5.19 and 5.20 display the mode spectrum of the DMD in the anterior plane

for the NC and the LC, respectively. The zeroth mode in both cases hold around 81% of the total

kinetic energy with an amplitude of 5.3 and 3.2 respectively. The first four modes for the NC have

similar frequencies as for the lateral plane, but with different amplitudes. When comparing the

102

anterior view (Figure 5.17) to the lateral view (Figure 5.21), similar phenomena can be visualized between the modes. A backflow, associated with a Kelvin-Helmholtz instability at the jet interface is present in the second mode as shown by Figure 5.21 a2, b2, c2 at a frequency of 2.4 Hz. A pure backflow characterizes mode 3 with a frequency of 3.6 Hz, and the washing of the AAA region can clearly be seen in mode 4.
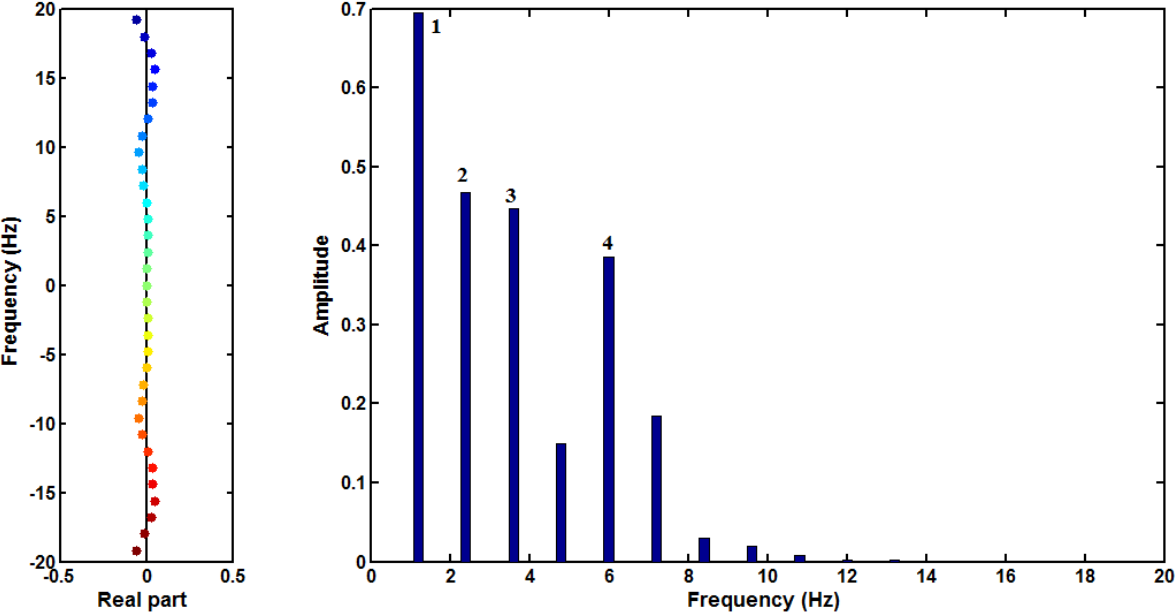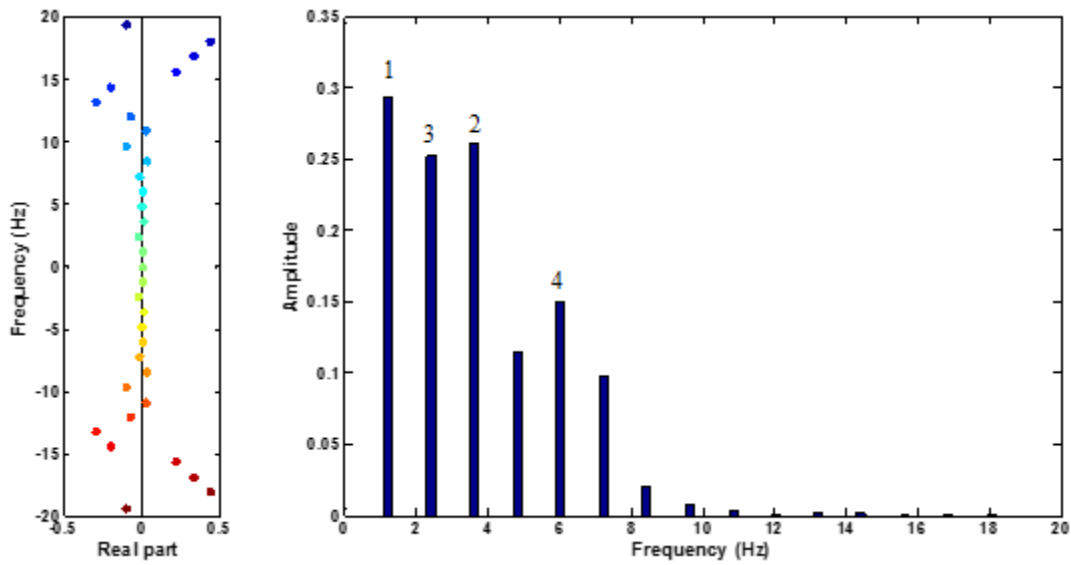

Figure 5.19: Mode spectrum (left) mode energy distribution (right) for the anterior plane in the NC
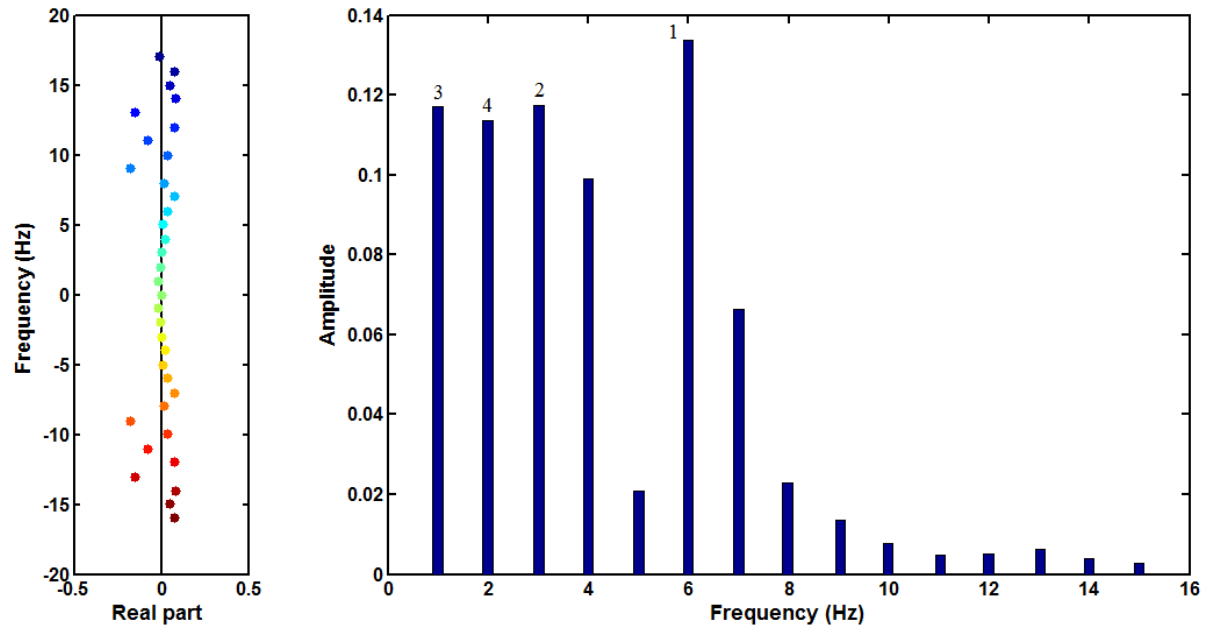
Figure 5.20: Mode spectrum (left) mode energy distribution (right) for the anterior plane in the LC
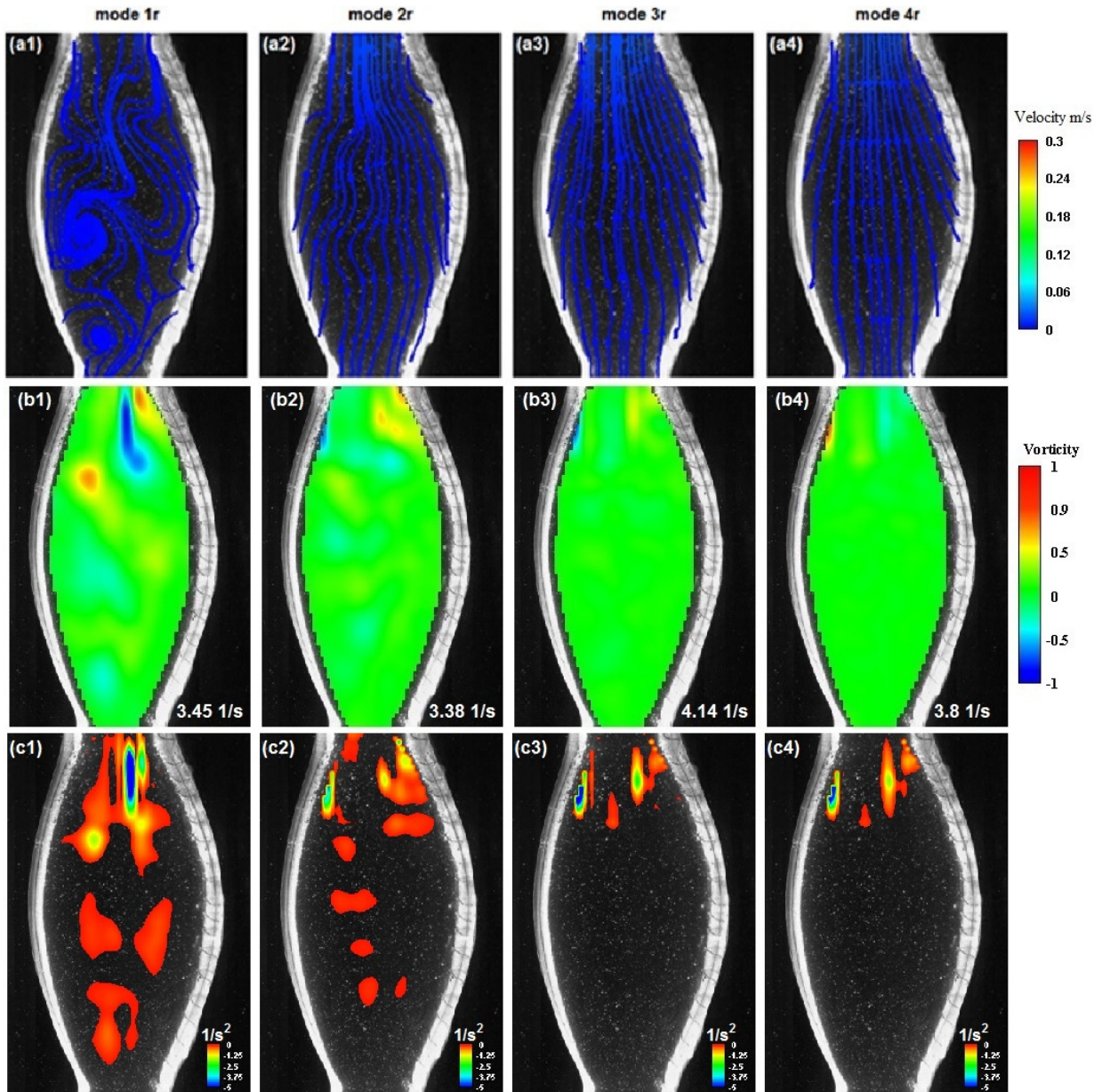
Figure 5.21: DMD real modes of for the lateral plane for the NC in terms of (a) velocity streamlines and (b) vorticity (c) swirling strength

For the LC (Figure 5.20), the spectrum between the anterior and the lateral planes have also a similar trend with backflow in the first and the second modes, and complex structures in the third and the fourth modes.
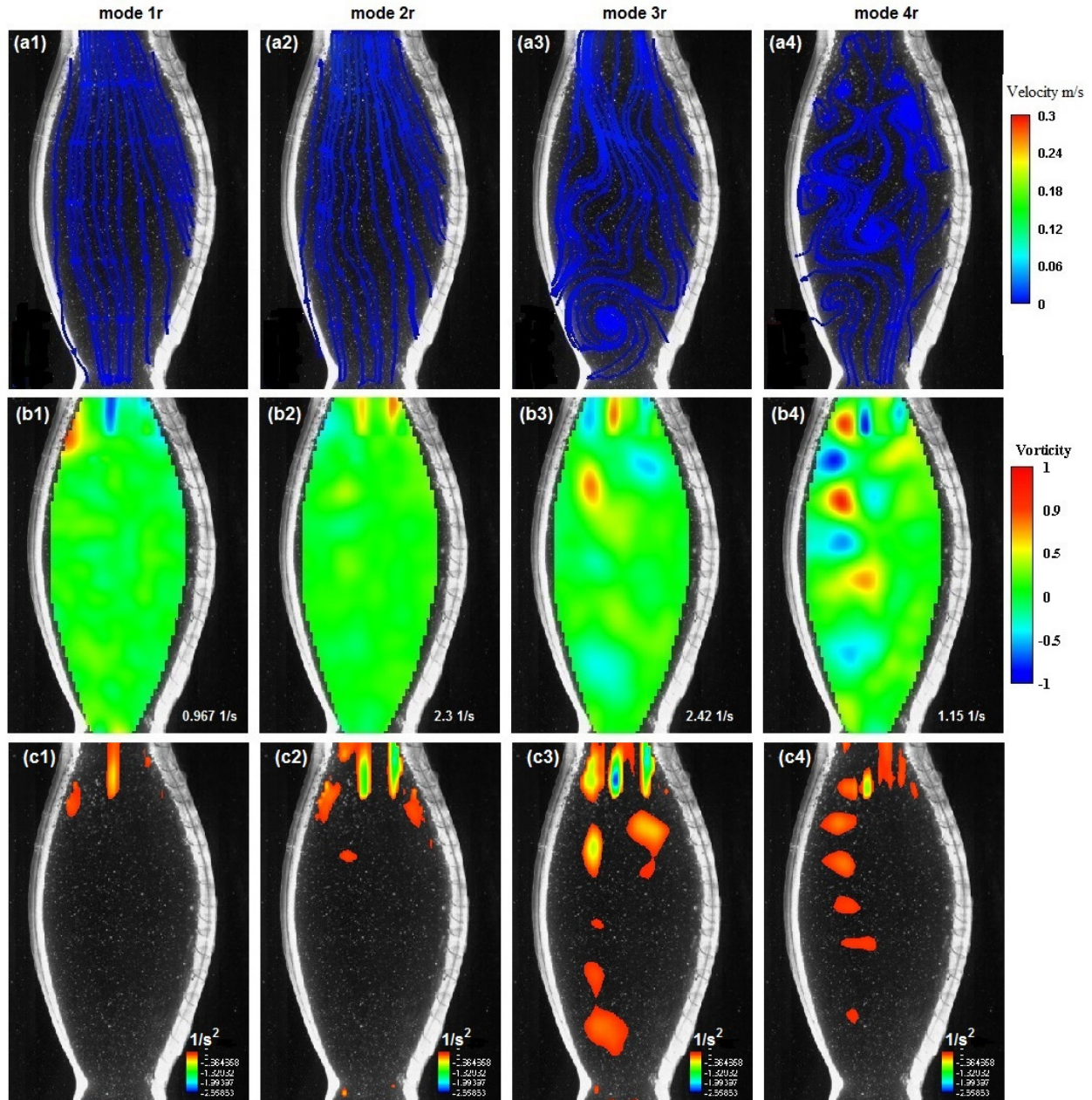
Figure 5.22: DMD real modes of for the lateral plane for the LC in terms of (a) velocity streamlines and (b) vorticity (c) swirling strength

The general outcome from the DMD applied to the NC for flow in an AAA is that it can be decomposed into four fundamental modes:

- An average mode with a zero frequency and higher energy content. This mode is characterized by a forward flow directed towards the iliac arteries with vortical structures in the AAA lumen.

106

-The first mode is characterized by a complex flow structure at a frequency of 1.2 Hz.

-The second and third modes have a frequency of 2.4 Hz and 3.6 Hz. These modes are characterized by a backflow.

- The fourth mode is characterized by washing of the blood stream having a frequency of 6 Hz.

These fundamental modes are for NC. Same scenario can be applied for the LC. However, the occurrence of the backflow and the amplitude of modes are different.

5.7 Discussion

This chapter can be considered as the first study investigating the flow in the cardiovascular system using POD and DMD. This allows for a deeper understanding of the most critical "hidden" flow structures associated with pathological conditions and hence develop clinical strategies to suppress/control them.

Particle residence time and viscous shear stress history provide a useful information regarding how blood particles, mainly platelets, are affected by the abnormal flow conditions imposed by the presence of an AAA. However, such tools fail to clearly identify the specific flow structures that are critical and that are potentially responsible for flow stasis or platelet activation. Powerful analysis tools such as POD and DMD can provide information on those critical structures, their energy, and their dynamics.

The presence of vortical structures in the anterior region of the AAA was highlighted by analyzing the recorded velocity snapshots. The strength of those structures and their contribution to the total kinetic energy was determined by POD of the velocity field. The comparison between the NC and the LC shows that reducing the flow rate limits the development of vortical structures in the AAA,

as mode 3 from POD on the LC shows mainly backflow and the sudden deceleration phenomenon holds lower energetic content compared to other ones in the LC. The presence of large vortical structures in the AAA lumen during some periods of the cardiac cycle is beneficial since such structures promote blood mixing. Biasetti et al. (2011) showed that the healthier regions of the AAA walls are associated with vortices. Intraluminal thrombus formation is usually found in the lower part of the anterior region (Tamagawa et al. 2009). In the NC, this region of the flow has a swirling behavior (Figure 5.6 b1, c1). However, reducing the flow rate in the LC shifted the shear layer and made this region behave as an island preventing blood particles from going in and out which limits blood mixing and promotes ILT (Figure 5.7 b1, c1).

DMD provides more information on the dynamics of the flow by computing their frequency and growth/decay rates. The challenge then is to identify how such structures affect the AAA in terms of progression or rupture. For example, a sudden temporal behavior could disturb the fluid flow, in a beneficial way that could force stagnant particles to leave the AAA. The two decomposition methods used in this chapter must be tested on patient data in order to clearly correlate the existence/absence of certain modes with the progression of the AAA.

6. CONCLUSIONS AND FUTURE WORKS

The present thesis includes several significant technical and scientific contributions to the current state of knowledge regarding the flow dynamics in an aneurysm of the abdominal aorta.

Contribution 1: The development of a realistic experimental facility for testing the flow in AAA models

In this thesis, the first realistic test facility capable of simulating the flow in AAA models has been designed and constructed. Our facility represents a significant improvement compared to the existing facilities in the literature. The model includes an anatomically complete aorta, the iliac arteries, and the renal arteries. Obtaining physiologically realistic flow and pressure waveforms was a great challenge, but ultimately we managed to obtained waveforms that are close to *in vivo* data recorded in patients with AAA.

Future work: Some modifications are still required in order to further improve our experimental facility. For instance, building the transparent elastic models of the AAAs has to be standardized in order to allow for testing of different AAA geometries and sizes and even patient-specific geometries. The system has to be modified in order to facilitate the replacement of the AAA models. The adjustment of the systemic resistance in the model is not optimized, using solenoid valves and a dedicated control system will facilitate simulating different flow and pressure conditions.

Contribution 2: Effect of low flow rate in an AAA model

The previous works in the literature mainly focused on the flow characteristics in AAA models under NC or under moderate exercise conditions. There were some discrepancies, however, regarding the beneficial effect of exercise in patients with AAAs. Although, it has been demonstrated using computer models that exercise reduces the particle residence time in the AAA

lumen, some studies highlighted the potential transition to turbulence under such flow regimes. In this thesis, we considered what is expected to be "the worst case scenario" in terms of the flow dynamics in an AAA, i.e. LC. The human body experiences physiological low flow conditions during night-time or sleeping or abnormal LC under pathological conditions for example in the case of spinal cord injury. From here, two important questions arise: 1) how does a LC affect the flow dynamics in the AAA lumen compared to a NC? Answering this question represents the major part of the present thesis, and 2) are there mechanisms that will allow for a "control" of the flow dynamics in an AAA lumen in patients at risk subjected to LC? Although answering this question requires extensive future work, we have already explored some potential interesting approaches.

In this thesis, we demonstrated and quantified the effect of the LC on the flow dynamics in an AAA model. LCs led to more flow stagnation in the AAA and an increase in particle residence time. As a consequence, several particles in critical regions of the AAA remained in the lumen, mainly close to the anterior wall, after several consecutive cycles, while they should have left the AAA under the NC. Such unfavorable flow conditions might promote intraluminal thrombus formation and then AAA progression and rupture.

Future works: In this thesis, we limited our study to one LC condition and one averaged geometry, future studies should include more experimental conditions and ideally patient-specific geometries. Also, our particle tracking algorithm is only based on two-dimensional velocity field recordings and neglected particle interactions. Although such an approach will be attractive in clinical settings with phase-contrast MRI recordings, future experimental studies have to include three-dimensional velocity measurements using stereoscopic PIV or Tomo-PIV and an optimized algorithm for tracking the particles in three-dimensional space.

Contribution 3: Singular value decomposition of the flow in an AAA model

The flow behavior investigated using the velocity snapshots give important information regarding the general flow structures in the AAA. However, it fails in extracting the "hidden" sub-structures that are responsible for the differences observed between the NC and the LC. More specifically, the increase in the number of particles that stayed in the AAA lumen under LC conditions. In this thesis, the "hidden" sub-structures, referred as 'modes', were extracted using advanced flow analysis tools: Proper Orthogonal Decomposition and Dynamic Mode Decomposition. To the best of our knowledge, this work is the first to apply such singular value decomposition methods to cardiovascular flows in general and to the flow dynamics in an AAA specifically.

POD and DMD highlighted the facts that LC conditions are characterized by more occurrence of a backflow and less temporal vortical structures. Vortices with a time scale close to the cardiac period are not beneficial since they contribute to an increase in particle residence time and may promote thrombus formation. However, short time scale vortices, in contrast, help "pull" blood particles from the low velocity regions to the regions where they can be released from the AAA domain.

Future work: The model used in this work was an idealized model. The flow is then more homogenous compared to the one expected in real patients. It is expected that the contribution of the first POD mode and the zeroth DMD mode become less predominant. Other modes are expected to have more contribution to the fluid flow, and it is expected to see more complex flow structures. Evaluating the flow structures for each patient using phase-contrast MRI or echo-PIV might provide essential information regarding thrombus formation and the risk of AAA rupture.

REFERENCES

Abe, T., Aoki, T., Yata, S., & Okada, M. (2011). Sleep duration is significantly associated with carotid artery atherosclerosis incidence in a Japanese population. *Atherosclerosis*, *217*(2), 509-513.

Adrian, Ronald J. "Particle-imaging techniques for experimental fluid mechanics." *Annual review of fluid mechanics* 23, no. 1 (1991): 261-304.

Adrian, R. J., & Westerweel, J. (2011). *Particle image velocimetry* (No. 30). Cambridge University Press.

Aird, W. C. (2007). Phenotypic heterogeneity of the endothelium I. Structure, function, and mechanisms. *Circulation research*, *100*(2), 158-173.

Amiral, J., Lormeau, J. C., Marfaing-Koka, A., Vissac, A. M., Wolf, M., Boyer-Neumann, C., ... & Meyer, D. (1997). Absence of cross-reactivity of SR90107A/ORG31540 pentasaccharide with antibodies to heparin-PF4 complexes developed in heparin-induced thrombocytopenia. *Blood coagulation & fibrinolysis*, *8*(2), 114-117.

Arzani, A., & Shadden, S. C. (2012). Characterization of the transport topology in patient-specific abdominal aortic aneurysm models. *Physics of Fluids (1994-present)*, *24*(8), 081901.

Asbury, C. L., Ruberti, J. W., Bluth, E. I., & Peattie, R. A. (1995). Experimental investigation of steady flow in rigid models of abdominal aortic aneurysms. *Annals of biomedical engineering*, *23*(1), 29-39.

Baxter, B. T., Terrin, M. C., & Dalman, R. L. (2008). Medical management of small abdominal aortic aneurysms. *Circulation*, *117*(14), 1883-1889.

Berger, S. A., & Jou, L. D. (2000). Flows in stenotic vessels. *Annual Review of Fluid Mechanics*, *32*(1), 347-382.

Biasetti, J., Hussain, F., & Gasser, T. C. (2011). Blood flow and coherent vortices in the normal and aneurysmatic aortas: a fluid dynamical approach to intra-luminal thrombus formation. *Journal of The Royal Society Interface*, rsif20110041.

Bluestein, D., Niu, L., Schoephoerster, R. T., & Dewanjee, M. K. (1996). Steady flow in an aneurysm model: correlation between fluid dynamics and blood platelet deposition. *Journal of biomechanical engineering*, *118*(3), 280-286.

Bluestein, D., Niu, L., Schoephoerster, R. T., & Dewanjee, M. K. (1997). Fluid mechanics of arterial stenosis: relationship to the development of mural thrombus. *Annals of biomedical engineering*, *25*(2), 344-356.

Bosch, J. L., Beinfeld, M. T., Halpern, E. F., Lester, J. S., & Gazelle, G. S. (2001). Endovascular versus Open Surgical Elective Repair of Infrarenal Abdominal Aortic Aneurysm: Predictors of Patient Discharge Destination 1. *Radiology*, *220*(3), 576-580.

Brown, L. C., Powell, J. T., Thompson, S. G., Epstein, D. M., Sculpher, M. J., & Greenhalgh, R. M. (2012). The UK EndoVascular Aneurysm Repair (EVAR) Trials: randomised trials of EVAR versus standard therapy.

Budwig, R., Elger, D., Hooper, H., & Slippy, J. (1993). Steady flow in abdominal aortic aneurysm models. *Journal of biomechanical engineering*, *115*(4A), 418-423.

Carmo, M., Colombo, L., Bruno, A., Corsi, F. R. M., Roncoroni, L., Cuttin, M. S., ... & Settembrini, P. G. (2002). Alteration of elastin, collagen and their cross-links in abdominal aortic aneurysms. *European journal of vascular and endovascular surgery*, *23*(6), 543-549.

Caro, C. G. (2012). *The mechanics of the circulation*. Cambridge University Press.

Chambers, D., Epstein, D., Walker, S., Fayter, D., Paton, F., Wright, K., ... & Woolacott, N. (2009). Endovascular stents for abdominal aortic aneurysms: a systematic review and economic model.

Chen, C. Y., Antón, R., Hung, M. Y., Menon, P., Finol, E. A., & Pekkan, K. (2014). Effects of intraluminal thrombus on patient-specific abdominal aortic aneurysm hemodynamics via stereoscopic particle image velocity and computational fluid dynamics modeling. *Journal of biomechanical engineering*, *136*(3), 031001.

Chiu, J. J., & Chien, S. (2011). Effects of disturbed flow on vascular endothelium: pathophysiological basis and clinical perspectives. *Physiological reviews*, *91*(1), 327-387.

Cosadia, I., Borée, J., & Dumont, P. (2007). Coupling time-resolved PIV flow-fields and phase-invariant proper orthogonal decomposition for the description of the parameters space in a transparent Diesel engine. *Experiments in fluids*, *43*(2-3), 357-370.

Cowan, J. A., DIMICK, J. B., Henke, P. K., Rectenwald, J., Stanley, J. C., & UPCHURCH, G. R. (2006). Epidemiology of aortic aneurysm repair in the United States from 1993 to 2003. *Annals of the New York Academy of Sciences*, *1085*(1), 1-10.

Dalman, R. L., Tedesco, M. M., Myers, J., & Taylor, C. A. (2006). AAA disease. *Annals of the New York Academy of Sciences*, *1085*(1), 92-109.

Darling, R. C. (1970). Ruptured arteriosclerotic abdominal aortic aneurysms: a pathologic and clinical study. *The American Journal of Surgery*, *119*(4), 397-401.

Das, D., & Arakeri, J. H. (1998). Transition of unsteady velocity profiles with reverse flow. *Journal of Fluid Mechanics*, *374*, 251-283.

Degaute, J. P., Van De Borne, P., Linkowski, P., & Van Cauter, E. (1991). Quantitative analysis of the 24-hour blood pressure and heart rate patterns in young men. *Hypertension*, *18*(2), 199-210.

Deplano, V., Knapp, Y., Bertrand, E., & Gaillard, E. (2007). Flow behaviour in an asymmetric compliant experimental model for abdominal aortic aneurysm. *Journal of biomechanics*, *40*(11), 2406-2413.

Deplano, V., Meyer, C., Guivier-Curien, C., & Bertrand, E. (2013). New insights into the understanding of flow dynamics in an in vitro model for abdominal aortic aneurysms. *Medical engineering & physics*, *35*(6), 800-809.

Dooley, P. N., & Quinlan, N. J. (2009). Effect of eddy length scale on mechanical loading of blood cells in turbulent flow. *Annals of biomedical engineering*, *37*(12), 2449-2458.

Duclaux, V., Gallaire, F., & Clanet, C. (2010). A fluid mechanical view on abdominal aortic aneurysms. *Journal of Fluid Mechanics*, *664*, 5-32.

Duquesne, P., Maciel, Y., & Deschênes, C. (2015). Unsteady flow separation in a turbine diffuser. *Experiments in Fluids*, *56*(8), 1-15.

Egelhoff, C. J., Budwig, R. S., Elger, D. F., Khraishi, T. A., & Johansen, K. H. (1999). Model studies of the flow in abdominal aortic aneurysms during resting and exercise conditions. *Journal of biomechanics*, *32*(12), 1319-1329.

Etebari, A., & Vlachos, P. P. (2005). Improvements on the accuracy of derivative estimation from DPIV velocity measurements. *Experiments in Fluids*, *39*(6), 1040-1050.

Faggioli, G. L., Stella, A., Gargiulo, M., Tarantini, S., D'Addato, M., & Ricotta, J. J. (1994). Morphology of small aneurysms: definition and impact on risk of rupture. *The American journal of surgery*, *168*(2), 131-135.

Fessler, J. R., & Eaton, J. K. (1999). Turbulence modification by particles in a backward-facing step flow. *Journal of Fluid Mechanics*, *394*, 97-117.

Frazin, L. J., Vonesh, M. J., Chandran, K. B., Shipkowitz, T., Yaacoub, A. S., & McPherson, D. D. (1996). Confirmation and Initial Documentation of Thoracic and Abdominal Aortic Helical Flow: An Ultrasound Study. *ASAIO journal*, *42*(6), 951-956.

Fry, D. L. (1968). Acute vascular endothelial changes associated with increased blood velocity gradients. *Circulation research*, *22*(2), 165-197.

Garcia, D. (2010). Robust smoothing of gridded data in one and higher dimensions with missing values. *Computational statistics & data analysis*, *54*(4), 1167-1178.

Giddens, D. P., Zarins, C. K., & Glagov, S. (1993). The role of fluid mechanics in the localization and detection of atherosclerosis. *Journal of biomechanical engineering*, *115*(4B), 588-594.

Glagov, S., Zarins, C., Giddens, D. P., & Ku, D. N. (1988). Hemodynamics and atherosclerosis. Insights and perspectives gained from studies of human arteries. *Archives of pathology & laboratory medicine*, *112*(10), 1018-1031.

Gopalakrishnan, S. S., Pier, B., & Biesheuvel, A. (2014). Dynamics of pulsatile flow through model abdominal aortic aneurysms. *Journal of Fluid Mechanics*, *758*, 150-179.

Gordon, I. L., Kohl, C. A., Arefi, M., Complin, R. A., & Vulpe, M. (1996). Spinal cord injury increases the risk of abdominal aortic aneurysm. *The American surgeon*, *62*(3), 249-252.

Grandner, M. A., Hale, L., Moore, M., & Patel, N. P. (2010). Mortality associated with short sleep duration: the evidence, the possible mechanisms, and the future. *Sleep medicine reviews*, *14*(3), 191-203.

Greenhalgh, R. M., Brown, L. C., Epstein, D., Kwong, G. P., Powell, J. T., & Sculpher, M. J. (2005). Endovascular aneurysm repair and outcome in patients unfit for open repair of abdominal aortic aneurysm (EVAR trial 2): randomised controlled trial. *Lancet*, *365*(9478), 2187-92.

Grigioni, M., Morbiducci, U., D'Avenio, G., Di Benedetto, G., & Del Gaudio, C. (2005). A novel formulation for blood trauma prediction by a modified power-law mathematical model. *Biomechanics and Modeling in Mechanobiology*, *4*(4), 249-260.

Grinberg, L., Yakhot, A., & Karniadakis, G. E. (2009). Analyzing transient turbulence in a stenosed carotid artery by proper orthogonal decomposition. *Annals of biomedical engineering*, *37*(11), 2200-2217.

Hans, S. S., Jareunpoon, O., Balasubramaniam, M., & Zelenock, G. B. (2005). Size and location of thrombus in intact and ruptured abdominal aortic aneurysms. *Journal of vascular surgery*, *41*(4), 584-588.

Harris, J. (2012) Investigation of relative importance of some error sources in particle Image velocimetry.

Hill, D. F., Sharp, K. V., & Adrian, R. J. (2000). Stereoscopic particle image velocimetry measurements of the flow around a Rushton turbine. *Experiments in Fluids*, *29*(5), 478-485.

Holmes, P., Lumley, J. L., & Berkooz, G. (2012). *Turbulence, coherent structures, dynamical systems and symmetry*. Cambridge university press.

Hussain, A. F. (1986). Coherent structures and turbulence. *Journal of Fluid Mechanics*, *173*, 303-356.

Isselbacher, E. M. (2005). Thoracic and abdominal aortic aneurysms. *Circulation*, *111*(6), 816-828.

Jeong, J., & Hussain, F. (1995). On the identification of a vortex. *Journal of fluid mechanics*, *285*, 69-94.

Jilkova, Z. M., Lisowska, J., Manet, S., Verdier, C., Deplano, V., Geindreau, C.& Duperray, A. (2014). CCM proteins control endothelial β1 integrin dependent response to shear stress. *Biology open*, BIO201410132.

Keane, R. D., & Adrian, R. J. (1992). Theory of cross-correlation analysis of PIV images. *Applied scientific research*, *49*(3), 191-215.

Kefayati, S., & Poepping, T. L. (2013). Transitional flow analysis in the carotid artery bifurcation by proper orthogonal decomposition and particle image velocimetry. *Medical engineering & physics*, *35*(7), 898-909.

Keshavarz-Motamed, Z., Garcia, J., Gaillard, E., Maftoon, N., Di Labbio, G., Cloutier, G., & Kadem, L. (2014). Effect of coarctation of the aorta and bicuspid aortic valve on flow dynamics and turbulence in the aorta using particle image velocimetry. *Experiments in fluids*, *55*(3), 1-16.

Khanafer, K., & Berguer, R. (2009). Fluid–structure interaction analysis of turbulent pulsatile flow within a layered aortic wall as related to aortic dissection. *Journal of biomechanics*, *42*(16), 2642-2648.

Khanafer, K. M., Bull, J. L., Upchurch, G. R., & Berguer, R. (2007). Turbulence significantly increases pressure and fluid shear stress in an aortic aneurysm model under resting and exercise flow conditions. *Annals of vascular surgery*, *21*(1), 67-74.

Khatri, I. M., & Freis, E. D. (1969). Hemodynamic changes during sleep in hypertensive patients. *Circulation*, *39*(6), 785-790.

Kilner, P. J., Yang, G. Z., Mohiaddin, R. H., Firmin, D. N., & Longmore, D. B. (1993). Helical and retrograde secondary flow patterns in the aortic arch studied by three-directional magnetic resonance velocity mapping. *Circulation*, *88*(5), 2235-2247.

King, C. R., Knutson, K. L., Rathouz, P. J., Sidney, S., Liu, K., & Lauderdale, D. S. (2008). Short sleep duration and incident coronary artery calcification. *Jama*, *300*(24), 2859-2866.

Ķīsis, K., Krieviņš, D., Naškoviča, K., Gediņš, M., Šavlovskis, J., Ezīte, N., ... & Zariņš, K. (2012). Quality of life after endovascular abdominal aortic aneurysm repair: nellix sac-anchoring endoprosthesis versus open surgery. *Medicina (Kaunas)*, *48*(6), 286-291.

Kleinstreuer, C., & Li, Z. (2006). Analysis and computer program for rupture-risk prediction of abdominal aortic aneurysms. *BioMedical Engineering OnLine*, *5*(1), 1.

Knutson, K. L. (2010). Sleep duration and cardiometabolic risk: a review of the epidemiologic evidence. *Best practice & research Clinical endocrinology & metabolism*, *24*(5), 731-743.

Ku, D. N. (1997). Blood flow in arteries. *Annual Review of Fluid Mechanics*, *29*(1), 399-434.

Länne, T., Sonesson, B., Bergqvist, D., Bengtsson, H., & Gustafsson, D. (1992). Diameter and compliance in the male human abdominal aorta: influence of age and aortic aneurysm. *European journal of vascular surgery*, *6*(2), 178-184.

Lasheras, J. C. (2007). The biomechanics of arterial aneurysms. *Annu. Rev. Fluid Mech.*, *39*, 293-319.

Lederle, F. A., & Simel, D. L. (1999). Does this patient have abdominal aortic aneurysm?. *Jama*, *281*(1), 77-82.

Les, A. S., Shadden, S. C., Figueroa, C. A., Park, J. M., Tedesco, M. M., Herfkens, R. J., ... & Taylor, C. A. (2010). Quantification of hemodynamics in abdominal aortic aneurysms during rest and exercise using magnetic resonance imaging and computational fluid dynamics. *Annals of biomedical engineering*, *38*(4), 1288-1313.

Li, Z., & Kleinstreuer, C. (2006). Analysis of biomechanical factors affecting stent-graft migration in an abdominal aortic aneurysm model. *Journal of biomechanics*, *39*(12), 2264-2273.

Lighthill, J. (1975). *Mathematical biofluiddynamics* (Vol. 17). Siam.

Lokhandwalla, M., & Sturtevant, B. (2001). Mechanical haemolysis in shock wave lithotripsy (SWL): I. Analysis of cell deformation due to SWL flow-fields. *Physics in medicine and biology*, *46*(2), 413.

London, G. M., & Guerin, A. P. (1999). Influence of arterial pulse and reflected waves on blood pressure and cardiac function. *American heart journal*, *138*(3), S220-S224.

Lumley, J. L. (1967). The structure of inhomogeneous turbulent flows. *Atmospheric turbulence and radio wave propagation*, 166-178.

Malek, A. M., Alper, S. L., & Izumo, S. (1999). Hemodynamic shear stress and its role in atherosclerosis. *Jama*, *282*(21), 2035-2042.

Mason, R. H., Ruegg, G., Perkins, J., Hardinge, M., Amann-Vesti, B., Senn, & Kohler, M. (2011). Obstructive sleep apnea in patients with abdominal aortic aneurysms: highly prevalent and associated with aneurysm expansion. *American journal of respiratory and critical care medicine*, *183*(5), 668-674.

Meyer, K. E., Pedersen, J. M., & Özcan, O. (2007). A turbulent jet in crossflow analysed with proper orthogonal decomposition. *Journal of Fluid Mechanics*, *583*, 199-227.

Miller, M. A., Kandala, N. B., Kumari, M., Marmot, M. G., & Cappuccio, F. P. (2010). Relationships between sleep duration and von Willebrand factor, factor VII, and fibrinogen Whitehall II study. *Arteriosclerosis, thrombosis, and vascular biology*, *30*(10), 2032-2038.

Moore, J. E., Ku, D. N., Zarins, C. K., & Glagov, S. (1992). Pulsatile flow visualization in the abdominal aorta under differing physiologic conditions: implications for increased susceptibility to atherosclerosis. *Journal of biomechanical engineering*, *114*(3), 391-397.

Moore, J. E., & Ku, D. N. (1994). Pulsatile velocity measurements in a model of the human abdominal aorta under resting conditions. *Journal of biomechanical engineering*, *116*(3), 337-346.

Muzio, G. (2013) Analysis of the unsteady behavior in shockwave turbulent boundary layer interaction. *PhD Thesis*.

Nakahashi, T. K., Hoshina, K., Tsao, P. S., Sho, E., Sho, M., Karwowski, J. K, & Dalman, R. L. (2002). Flow loading induces macrophage antioxidative gene expression in experimental aneurysms. *Arteriosclerosis, thrombosis, and vascular biology*, *22*(12), 2017-2022.

Nerem, R. M., Seed, W. A., & Wood, N. B. (1972). An experimental study of the velocity distribution and transition to turbulence in the aorta. *Journal of Fluid Mechanics*, *52*(01), 137-160.

Nichols, W., O'Rourke, M., & Vlachopoulos, C. (Eds.). (2011). *McDonald's blood flow in arteries: theoretical, experimental and clinical principles*. CRC Press.

Nishio, S. (2008) Uncertainty Analysis: Particle Imaging Velocimetry (PIV). *ITTC – Recommended Procedures and Guidelines*.

Okamoto, K., Nishio, S., Saga, T., & Kobayashi, T. (2000). Standard images for particle-image velocimetry. *Measurement Science and Technology*, *11*(6), 685.

Pachulski, R. T., Weinberg, A. L., & Chan, K. L. (1991). Aortic aneurysm in patients with functionally normal or minimally stenotic bicuspid aortic valve. *The American journal of cardiology*, *67*(8), 781-782.

Patel, V. (2011). *Impact of geometry on blood flow patterns in abdominal aortic aneurysms*. *Master Thesis*.

Peattie, K., & Ringer, A. (1994). Management and the environment in the UK and Germany: a comparison. *European Management Journal*, *12*(2), 216-225.

Pedley, T. J., & Luo, X. Y. (1995). Fluid mechanics of large blood vessels.add

Perrin, R., Braza, M., Cid, E., Cazin, S., Barthet, A., Sevrain, A & Thiele, F. (2007). Obtaining phase averaged turbulence properties in the near wake of a circular cylinder at high Reynolds number using POD. *Experiments in Fluids*, *43*(2-3), 341-355.

Peterson, D. M., Stathopoulos, N. A., Giorgio, T. D., Hellums, J. D., & Moake, J. L. (1987). Shear-induced platelet aggregation requires von Willebrand factor and platelet membrane glycoproteins Ib and IIb-IIIa. *Blood*, *69*(2), 625-628.

Pettersson, M., Bergbom, I., & Mattsson, E. (2012). Health related quality of life after treatment of abdominal aortic aneurysm with open and endovascular techniques—a two-year follow up. *Surgical Science*, *3*(09), 436.

Proctor, J. L., & Eckhoff, P. A. (2015). Discovering dynamic patterns from infectious disease data using dynamic mode decomposition. *International health*, *7*(2), 139-145.

Raffel, M., Willert, C. E., Wereley, S., & Kompenhans, J. (2013). *Particle image velocimetry: a practical guide*. Springer.

Raghavan, M. L., & Vorp, D. A. (2000). Toward a biomechanical tool to evaluate rupture potential of abdominal aortic aneurysm: identification of a finite strain constitutive model and evaluation of its applicability. *Journal of biomechanics*, *33*(4), 475-482.

Raval, J. S., Waters, J. H., Seltsam, A., Scharberg, E. A., Richter, E., Daly, A. R., & Yazer, M. H. (2010). The use of the mechanical fragility test in evaluating sublethal RBC injury during storage. *Vox sanguinis*, *99*(4), 325-331.

Rayz, V. L., Boussel, L., Ge, L., Leach, J. R., Martin, A. J., Lawton, M. T., ... & Saloner, D. (2010). Flow residence time and regions of intraluminal thrombus deposition in intracranial aneurysms. *Annals of biomedical engineering*, *38*(10), 3058-3069.

Reed, D., Reed, C., Stemmermann, G., & Hayashi, T. (1992). Are aortic aneurysms caused by atherosclerosis?. *Circulation*, *85*(1), 205-211.

Rowley, C. W., Mezić, I., Bagheri, S., Schlatter, P., & Henningson, D. S. (2009). Spectral analysis of nonlinear flows. *Journal of fluid mechanics*, *641*, 115-127.

Sahara, M., Sata, M., Morita, T., Hirata, Y., & Nagai, R. (2012). Nicorandil attenuates monocrotaline-induced vascular endothelial damage and pulmonary arterial hypertension. *PloS one*, *7*(3), e33367.

Sakalihasan, N., Limet, R., & Defawe, O. D. (2005). Abdominal aortic aneurysm. *The Lancet*, *365*(9470), 1577-1589.

Salsac, A. V., Sparks, S. R., Chomaz, J. M., & Lasheras, J. C. (2006). Evolution of the wall shear stresses during the progressive enlargement of symmetric abdominal aortic aneurysms. *Journal of Fluid Mechanics*, *560*, 19-51.

Satta, J., Läärä, E., & Juvonen, T. (1996). Intraluminal thrombus predicts rupture of an abdominal aortic aneurysm. *Journal of vascular surgery*, *23*(4), 737-739.

Schmid, P. J. (2010). Dynamic mode decomposition of numerical and experimental data. *Journal of Fluid Mechanics*, *656*, 5-28.

Schrader, T., Peattie, R. A., Bluth, E. I., & Comstock, C. E. (1992). A qualitative investigation of turbulence in flow through a model abdominal aortic aneurysm. *Investigative radiology*, *27*(7), 515-519.

Schurink, G Van, J., Visser, M., & Van, H., (2000). Thrombus within an aortic aneurysm does not reduce pressure on the aneurysmal wall. *Journal of Vascular Surgery*, *31*(3), 501-506.

Seed, W. A., & Wood, N. B. (1971). Velocity patterns in the aorta. *Cardiovascular research*, *5*(3), 319-330.

Seena, A., & Sung, H. J. (2011). Dynamic mode decomposition of turbulent cavity flows for self-sustained oscillations. *International Journal of Heat and Fluid Flow*, *32*(6), 1098-1110.

Semeraro, O., Bellani, G., & Lundell, F. (2012). Analysis of time-resolved PIV measurements of a confined turbulent jet using POD and Koopman modes. *Experiments in fluids*, *53*(5), 1203-1220.

Sforza, D. M., Putman, C. M., & Cebral, J. R. (2009). Hemodynamics of cerebral aneurysms. *Annual review of fluid mechanics*, *41*, 91.

Shankaran, H., Alexandridis, P., & Neelamegham, S. (2003). Aspects of hydrodynamic shear regulating shear-induced platelet activation and self-association of von Willebrand factor in suspension. *Blood*, *101*(7), 2637-2645.

Singh, K., Bønaa, K. H., Jacobsen, B. K., Bjørk, L., & Solberg, S. (2001). Prevalence of and Risk Factors for Abdominal Aortic Aneurysms in a Population-based Study The Tromsø Study. *American journal of epidemiology*, *154*(3), 236-244.

Sirovich, L. (1987). Turbulence and the dynamics of coherent structures part I: coherent structures. *Quarterly of applied mathematics*, *45*(3), 561-571.

Speelman, L., Schurink, G. W. H., Bosboom, E. M. H., Buth, J., Breeuwer, M., van de Vosse, F. N., & Jacobs, M. H. (2010). The mechanical role of thrombus on the growth rate of an abdominal aortic aneurysm. *Journal of vascular surgery*, *51*(1), 19-26.

Stamatopoulos, C., Mathioulakis, D. S., Papaharilaou, Y., & Katsamouris, A. (2011). Experimental unsteady flow study in a patient-specific abdominal aortic aneurysm model. *Experiments in fluids*, *50*(6), 1695-1709.

Suh, G. Y., Les, A. S., Tenforde, A. S., Shadden, S. C., Spilker, R. L., Yeung, J. J., & Taylor, C. A. (2011). Hemodynamic changes quantified in abdominal aortic aneurysms with increasing exercise intensity using MR exercise imaging and image-based computational fluid dynamics. *Annals of biomedical engineering*, *39*(8), 2186-2202.

Swillens, A., Lanoye, L., De Backer, J., Stergiopulos, N., Verdonck, P. R., Vermassen, F., & Segers, P. (2008). Effect of an abdominal aortic aneurysm on wave reflection in the aorta. *IEEE Transactions on Biomedical Engineering*, *55*(5), 1602-1611.

Tamagawa, M., Kaneda, H., Hiramoto, M., & Nagahama, S. (2009). Simulation of thrombus formation in shear flows using lattice Boltzmann method. *Artificial organs*, *33*(8), 604-610.

Tanné, D., Bertrand, E., Kadem, L., Pibarot, P., & Rieu, R. (2010). Assessment of left heart and pulmonary circulation flow dynamics by a new pulsed mock circulatory system. *Experiments in fluids*, *48*(5), 837-850.

Thubrikar, M. J., Robicsek, F., Labrosse, M., Chervenkoff, V., & Fowler, B. L. (2003). Effect of thrombus on abdominal aortic aneurysm wall dilation and stress. *Journal of Cardiovascular Surgery*, *44*(1), 67.

Tu, J. H., Rowley, C. W., Luchtenburg, D. M., Brunton, S. L., & Kutz, J. N. (2013). On dynamic mode decomposition: theory and applications. *arXiv preprint arXiv:1312.0041*.

USA, P. H. 2016. Abdominal Aortic Aneurysm.

Vollmar, J. F., Pauschinger, P., Paes, E., Henze, E., & Friesch, A. (1989). Aortic aneurysms as late sequelae of above-knee amputation. *The Lancet*, *334*(8667), 834-835.

Vorp, D. A., Lee, P. C., Wang, D. H., Makaroun, M. S., Nemoto, E. M., Ogawa, S., & Webster, M. W. (2001). Association of intraluminal thrombus in abdominal aortic aneurysm with local hypoxia and wall weakening. *Journal of Vascular Surgery*, *34*(2), 291-299.

Waite, L., & Fine, J. M. (2007). Applied biofluid mechanics.

Wilson, K., Bradbury, A., Whyman, M., Hoskins, P., Lee, A., Fowkes, G, & Ruckley, C. V. (1998). Relationship between abdominal aortic aneurysm wall compliance and clinical outcome: a preliminary analysis. *European journal of vascular and endovascular surgery*, *15*(6), 472-477.

Wu, W., Wang, W. Q., Yang, D. Z., & Qi, M. (2007). Stent expansion in curved vessel and their interactions: a finite element analysis. *Journal of biomechanics*, *40*(11), 2580-2585.

Xue, M., Yin, H. J., Wu, C. F., Ma, X. J., Guo, C. Y., Huang, Y, & Chen, K. J. (2013). Effect of Chinese drugs for activating blood circulation and detoxifying on indices of thrombosis, inflammatory reaction, and tissue damage in a rabbit model of toxin-heat and blood stasis syndrome. *Chinese journal of integrative medicine*, *19*, 42-47.

Yellin, E. L. (1966). Laminar-turbulent transition process in pulsatile flow. *Circulation research*, *19*(4), 791-804.

Yin, W., Alemu, Y., Affeld, K., Jesty, J., & Bluestein, D. (2004). Flow-induced platelet activation in bileaflet and monoleaflet mechanical heart valves. *Annals of biomedical engineering*, *32*(8), 1058-1066.

Yip, T. H., & Yu, S. C. M. (2001). Cyclic transition to turbulence in rigid abdominal aortic aneurysm models. *Fluid Dynamics Research*, *29*(2), 81-113.

Yu, S. C. M. (2000). Steady and pulsatile flow studies in abdominal aortic aneurysm models using particle image velocimetry. *International Journal of Heat and Fluid Flow*, *21*(1), 74-83.

Yu, S. C. M., Chan, W. K., Ng, B. T. H., & Chua, L. P. (1999). A numerical investigation on the steady and pulsatile flow characteristics in axi-symmetric abdominal aortic aneurysm models with some experimental evaluation. *Journal of medical engineering & technology*, *23*(6), 228-239.

Zankl, A. R., Schumacher, H., Krumsdorf, U., Katus, H. A., Jahn, L., & Tiefenbacher, C. P. (2007). Pathology, natural history and treatment of abdominal aortic aneurysms. *Clinical Research in Cardiology*, *96*(3), 140-151.

Zarins, C. K., Crabtree, T., Bloch, D. A., Arko, F. R., Ouriel, K., & White, R. A. (2006). Endovascular aneurysm repair at 5 years: does aneurysm diameter predict outcome?. *Journal of vascular surgery*, *44*(5), 920-930.